Titre: Title:	Passive Flow Control at Impeller Radial Bend for Stall Delay in Centrifugal Compressors with Fishtail Pipe Diffusers
Auteur: Author:	Farzad Ashrafi
Date:	2020
Type:	Mémoire ou thèse / Dissertation or Thesis
Référence: Citation:	Ashrafi, F. (2020). Passive Flow Control at Impeller Radial Bend for Stall Delay in Centrifugal Compressors with Fishtail Pipe Diffusers [Thèse de doctorat, Polytechnique Montréal]. PolyPublie. https://publications.polymtl.ca/5375/

URL de PolyPublie: PolyPublie URL:	https://publications.polymtl.ca/5375/
Directeurs de recherche: Advisors:	Huu Duc Vo
Programme: Program:	Génie mécanique

POLYTECHNIQUE MONTRÉAL

affiliée à l'Université de Montréal

Passive Flow Control at Impeller Radial Bend for Stall Delay in Centrifugal Compressors with Fishtail Pipe Diffusers

FARZAD ASHRAFI

Département de génie mécanique

Thèse présentée en vue de l'obtention du diplôme de *Philosophiæ Doctor*

Génie mécanique

Août 2020

POLYTECHNIQUE MONTRÉAL

affiliée à l'Université de Montréal

Cette thèse intitulée:

Passive Flow Control at Impeller Radial Bend for Stall Delay in Centrifugal Compressors with Fishtail Pipe Diffusers

présentée par **Farzad ASHRAFI**

en vue de l'obtention du diplôme de *Philosophiæ Doctor*

a été dûment acceptée par le jury d'examen constitué de :

Alain BATAILLY, président
Huu Duc VO, membre et directeur de recherche
Jean-Yves TRÉPANIER, membre
William D.E. ALLAN, membre externe

ACKNOWLEDGEMENTS

I would first like to expresses my deepest gratitude to Professor Huu Duc VO, my thesis advisor for accepting me as his Ph.D. candidate, defining an interesting research project, providing analytical and technical support and his availability over the past four years. I have also passed my masters' project under his supervision in the period of 2012-2014 and I have been his student for almost 9 years now. He is a great mentor, advisor and more importantly a true friend who always keeps his students motivated. I appreciate being his student and taking advantage of his immense knowledge in the field and look forward to future scientific collaborations besides our friendship.

I wish to thank the Natural Sciences and Engineering Research Council of Canada (NSERC) Discovery Grant program for funding this research for the academic year 2016-2017.

I would also like to thank Fonds du Recherche du Québec-Nature et Technologie (FRQ-NT) for recognizing me as a recipient of the Ph.D. scholarship for the academic years 2017-2019 and providing me with financial support. Special appreciation also goes to Fondation de la Polytechnique de Montréal for recognizing me as the recipient of different doctoral bursaries (Delphine-Bourgoin (2017), J-Armand-Bombardier (2018) and Pratt & Whitney Canada (2018)).

I am grateful to Canada Foundation for Innovation (CFI), Ministère de l'Économie, de l'Innovation et des Exportations du Québec (MEIE), RMGA and the Fonds de recherche du Québec-Nature et technologies (FRQ-NT) for funding the operation of the supercomputers (Cottos, Briaree, Cedar, Beluga and Graham) used for the numerical computations in this research which are managed by Calcul Québec and Compute Canada.

I am also thankful to my manager at Pratt & Whitney Canada, Dr. Sri SREEKANTH (manager of the Hot Section Durability Department) for his encouragements and support. Completing the Ph.D. research while having a full-time job in industry would be impossible without his support.

Last but not least, I would like to thank my family for their continuous presence, patience, encouragement and moral supports during the past four years.

RÉSUMÉ

Par leurs hauts rapports de pression par étage, les compresseurs centrifuges ont le potentiel d'être utilisés sur des moteurs à haut taux de dilution d'avions de ligne afin de réduire la longueur, le poids et la complexité de ces moteurs, si seulement leurs rendements isentropiques et marges de décrochage peuvent être améliorés. Cette recherche propose une nouvelle stratégie pour augmenter la marge de décrochage via le contrôle passif de l'écoulement au coude de l'impulseur plus tôt qu'à son bord d'attaque comme ce fut le cas auparavant. Comparée au bord d'attaque, la région du coude de l'impulseur présente moins de contraintes géométriques et est potentiellement plus efficace au niveau de l'effet du contrôle passif sur les structures d'écoulement à basse quantité de mouvement qui peuvent mener au décrochage. Cette recherche vise à faire une première évaluation de cette stratégie, à élucider le mécanisme par lequel elle peut efficacement retarder le décrochage et à évaluer son impact sur les pertes et le rendement isentropique au débit massique de conception.

Deux compresseurs centrifuges avec des diffuseurs à tubes de type *fishtail* (le type de diffuseur le plus commun dans la motorisation aéronautique) ont été choisis pour études: une géométrie à haute vitesse (transsonique) pour lequel le décrochage est initié dans le diffuseur et une géométrie à basse vitesse (bas subsonique) dont le décrochage commence dans la partie avale de l'impulseur. Quatre techniques de contrôle passif de l'écoulement placé sur le carter au coude de l'impulseur ont été proposées, soit une rainure circonférentielle, des fentes, un tube de recirculation dans l'impulseur et un tube de recirculation diffuseur-impulseur. Des simulations numériques de l'écoulement de type RANS CFD ont été faites pour chaque compresseur sans et avec chacune des quatre techniques de contrôle de l'écoulement pour confirmer la composante responsable du décrochage et comprendre le mécanisme de décrochage; pour élucider le mécanisme par lequel une technique efficace retarde le décrochage; et pour enquêter sur les sources de perte de rendement isentropique au débit massique de design associées au contrôle passif de l'écoulement au coude de l'impulseur.

Les résultats indiquent que pour la géométrie à haute vitesse. Le décrochage est initié par un décollement de l'écoulement sur la surface supérieure du diffuseur à tube. Le contrôle de l'écoulement est efficace lorsque qu'il peut injecter du fluide à partir du carter au coude de l'impulseur avec une pénétration radiale profonde et une basse quantité de mouvement relative dans la direction de l'écoulement principal pour réduire la vitesse relative (dans le repère rotatif)

dans une région près de l'implanture de l'aube non loin de son extrados à la sortie de l'impulseur. Cette réduction de vitesse dans le repère rotatif donne une vitesse accrue dans le repère stationnaire à la position dans le diffuseur où le décollement de l'écoulement survient pour le supprimer et ainsi retarder le décrochage. Parmi les techniques proposées, c'est la rainure circonférentielle qui implémente ce mécanisme le plus efficacement pour fournir une augmentation de 9.39% à la marge de décrochage.

Pour la géométrie à basse vitesse, le décrochage est causé par le décollement de la couche limite sur l'extrados près du bout de l'impulseur au bord de fuite. Un contrôle de l'écoulement efficace pour ce type de décrochage est caractérisé par une injection de fluide à partir du carter au coude de l'impulseur avec une faible pénétration radiale et une haute quantité de mouvement relative dans la direction de l'écoulement principal. Ce fluide va faire augmenter la vitesse de l'écoulement dans la région problématique sur l'extrados de l'impulseur afin de supprimer le décollement de la couche limite et retarder le décrochage. À ce niveau, le tube de recirculation diffuseur-impulseur performe le mieux, donnant une augmentation de la marge de décrochage de 8.16%.

La perte de rendement isentropique associée au contrôle passif de l'écoulement au coude de l'impulseur est le résultat de pertes additionnelles dans l'impulseur et le diffuseur. Dans l'impulseur, le phénomène de jet dans un écoulement transverse engendre des pertes de mélange et de cisaillement. Dans le diffuseur, les pertes de cisaillement peuvent augmenter ou diminuer dépendamment de la variation du gradient de vitesse due à la redistribution de l'écoulement en présence du contrôle de l'écoulement.

La présente recherche a fait la première évaluation du contrôle passif de l'écoulement au coude de l'impulseur en terme de l'augmentation de la marge de décrochage et de la perte de rendement isentropique des compresseurs centrifuges. Elle a aussi élucidé la physique de l'écoulement qui peut être utilisée pour raffiner les techniques de contrôle passif de l'écoulement proposées et/ou pour inventer d'autres techniques afin de maximiser la marge de décrochage tout en minimisant la perte du rendement isentropique pour les compresseurs centrifuges, particulièrement ceux avec un diffuseur à tube de type *fishtail*.

ABSTRACT

Due to their high pressure ratio per stage, centrifugal compressors have the potential to be used in mainline high bypass ratio commercial aero-engines to reduce engine length, weight and mechanical complexity if their isentropic efficiency and stall margin can be improved. This research proposes a new strategy for extending the stall margin through passive flow control placed at the radial bend of the impeller rather than at its leading edge as has been done until now. Relative to the leading edge, the radial bend location presents fewer geometrical constraints and is potentially more effective for flow control devices to affect low-momentum flow structures that can lead to stall both in the impeller and in diffuser. This research aims to provide a first assessment of this strategy, elucidate the flow mechanism by which it can effectively delay stall and to assess its impact on losses and efficiency at the design mass flow.

Two centrifugal compressors with fishtail pipe diffusers (the most common type of diffuser used in aero-engines) were chosen for study: a high-speed transonic design for which stall is initiated by the diffuser and a low-speed low-subsonic design, which stalls through the impeller exducer. Four candidate flow control techniques were proposed placed on the impeller shroud at the radial bend, namely circumferential groove, slots, impeller recirculation pipe and diffuser-impeller recirculation pipe. RANS CFD simulations were performed on each compressor withand without each of the four flow control techniques to confirm the stalling component and to assess the stall mechanism, to elucidate the mechanism by which an effective passive flow control technique delays stall, and to investigate the sources of efficiency penalty at design mass flow associated with passive flow control at the radial bend.

The results indicate that for the high-speed design, stall is initiated by flow separation on the radially outer wall of the fishtail diffuser pipe. Flow control at the radial bend is most effective if it can inject flow from the shroud at the radial bend with deep radial penetration and low relative streamwise momentum to reduce flow velocity (in the rotating frame) on the lower span region not far from the blade suction side at the impeller trailing edge. This leads to high absolute velocity at the location in the fishtail pipe diffuser where flow separation occurs to suppress this phenomenon and delay stall. Among the proposed stall control techniques, the circumferential groove most

effectively implements this stall suppression mechanism, providing a stall margin extension of over 9%.

In the low-speed design, stall is caused by suction side blade boundary layer separation in the upper span region of the impeller exit. Effective passive flow control for this type of stall is characterized by shallow spanwise flow injection with high relative streamwise momentum from the flow control device at the radial bend. This results in increased streamwise velocity in the problematic region on the impeller suction side to suppress boundary layer separation and delay stall. In this case, the diffuser-to-impeller recirculation pipe performs best with slightly more than 8% extension in stall margin.

The efficiency penalty associated with passive flow control at the radial bend is the result of additional losses incurred in the impeller and the diffuser. The additional losses in the impeller stem from the jet-in-cross-flow phenomenon associated with the flow injection, which produces mixing, and shear losses. In the diffuser, shear losses can increase or decrease depending on whether the flow redistribution due to flow control increase or decrease velocity gradients.

This research provided the first assessment of passive flow control at the impeller radial bend in terms of stall margin extension and efficiency penalty of centrifugal compressors. It also elucidated flow physics that can be used to refine the proposed passive flow control techniques and/or devise new flow control techniques to maximize stall margin extension while minimizing efficiency penalty for centrifugal compressors, particularly those with fishtail pipe diffusers.

TABLE OF CONTENTS

LIST OF TABLES

LIST OF FIGURES

LIST OF SYMBOLS AND ABBREVIATIONS

Symbols and Variables

F	Force
$F_{cori.}$	Coriolis Force
F_p	Pressure Force
Kt	Throttle constant (Valve Closing Coefficient)
$\dot{m}_c$	Corrected Mass Flow
$\dot{m}_p$	Passage Mass Flow
$\dot{m}_r$	Recirculated Mass Flow
N	Rotational Speed of Compressor
P	Pressure
PR	Pressure Ratio
P_{ref}	Reference Pressure
P_s	Static Pressure
P_T	Total Pressure
$PR_{T\text{-}T}$	Stage Total-to-Total Pressure Ratio
R	Radius
Re	Reynolds Number
SMI	Stall Margin Improvement
T	Temperature
T_{ref}	Reference Temperature
T_T	Total Temperature
U_{tip}	Rotational Speed at Blade Tip

$V_{rel.}$	Relative Frame Velocity
$V_{stn.}$	Stationary Frame Velocity
$V_{strm.}$	Streamwise Velocity
V_{θ}	Circumferential Component of Absolute Velocity
$\dot{W}$	Work per Unit Mass Flow
$y+$	Non-Dimensional First Mesh Layer Height
γ	Air Specific Heat Ratio
η	Stage Efficiency
η_i	Impeller Efficiency
ρ	Density
σ	Diffuser Loss Coefficient
σ_u	Diffuser Loss Coefficient Upstream of Tongue
σ_d	Diffuser Loss Coefficient Downstream of Tongue
Ω	Rotational Velocity

Abbreviations

CFD	Computational Fluid Dynamics
GGI	General Grid Interface
IGV	Inlet Guide Vane
LE	Leading Edge
PS	Pressure Side
RANS	Reynolds-Averaged Navier-Stokes
RP	Recirculation Pipe

RPM	Revolutions per Minute
SS	Suction Side
SST	Shear Stress Transport
TE	Trailing Edge
TKE	Turbulence Kinetic Energy

LIST OF APPENDICES

CHAPTER 1 INTRODUCTION

1.1 Background

Centrifugal compressors can allow for a step improvement in aero-engines to address the financial and environmental challenges associated with commercial air traffic growth predicted to reach 6.4 billion passengers/year by 2030 [1].

The compressor along with combustion chamber and turbine are the three main components of a gas turbine engine. However due to the high number of (commonly used) axial compressor stages needed to get the desired pressure ratio, the compressor is the longest and heaviest component of an aero-engine. With its much higher stage pressure ratio, one centrifugal compressor stage can replace up to six axial stages to reduce engine length, weight and mechanical complexity. As illustrated in Figure 1.1, the main components of a centrifugal compressor are the *impeller* and the *diffuser*. The main role of the impeller is to impart work on the flow through the increase in its circumferential velocity while providing some static pressure rise through centrifugal effects and possibly flow deceleration in the relative (rotating) frame. The function of the diffuser is to convert the increased kinetic energy of the flow from the impeller into static pressure rise while redirecting the flow toward the radial, and sometimes also axial, direction.

Figure 1.1 also shows the main components of the impeller, namely the *main blades* and *splitter blades*, the latter not required for all impellers. The upstream part of the main blade, prior to the radial bend, is called the *inducer* while the downstream part is the *exducer*. *Backsweep* in an impeller refers to the angle of the impeller blades' exit with respect to the radial direction in the direction opposite to rotational direction as shown in Figure 1.1.

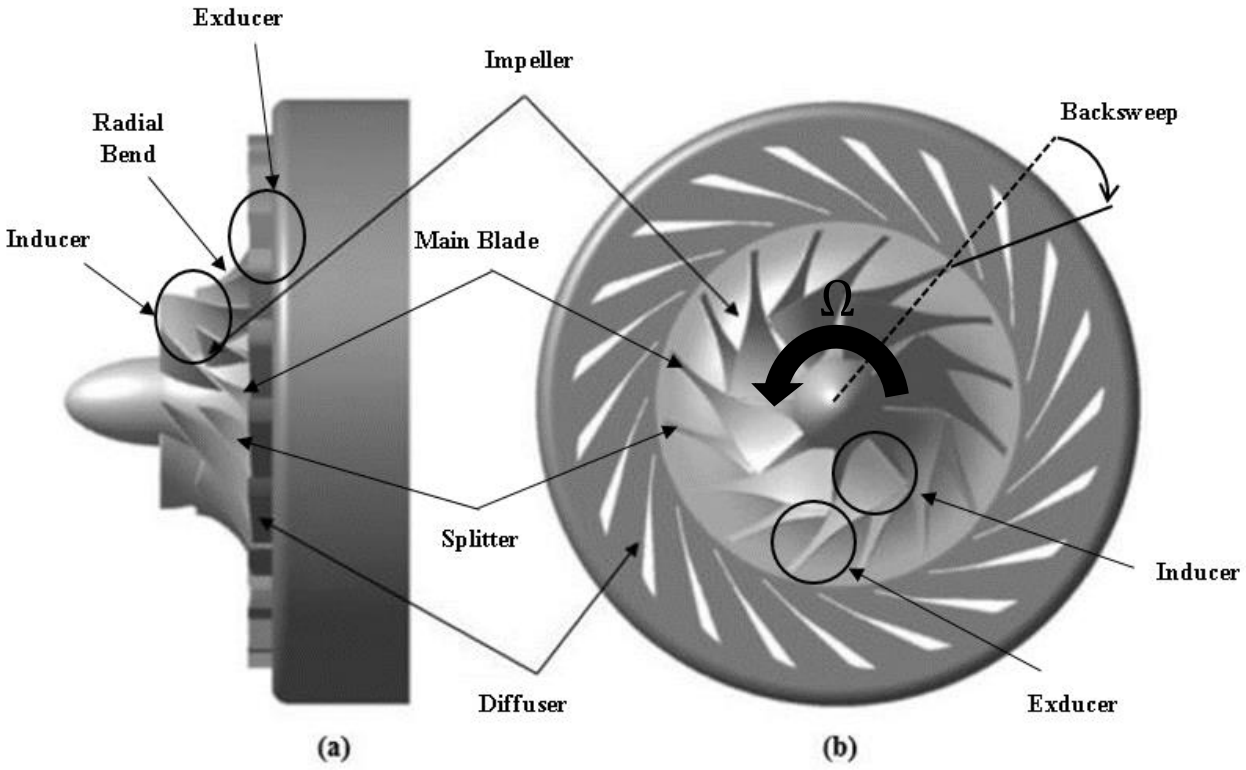

Figure 1.1: Centrifugal compressor components, (a) Side view, (b) Front View [2]

The use of centrifugal compressors in aircraft propulsion has been limited to small aero-engines for three main reasons. The first is higher stress associated with the impeller due to its larger radius compared to an axial compressor rotor with the same intake flow area. The second is its limited stage adiabatic efficiency (70-85% compared to 75-90% in axial compressors [3]) which translates to higher fuel consumption. The third, and perhaps most challenging for modern high-speed centrifugal compressors, is premature stall, where the circumferential flow symmetry in the compressor breaks down, which can lead to a drop in pressure ratio and engine power as well as violent flow oscillation across the engine that can lead to damage to its components (a phenomenon called *surge*). Premature stall is a problem with increased design rotating speed to achieve higher stage pressure ratio.

Small aero-engines, which represent a smaller market, are willing to trade some efficiency for mechanical simplicity and even then most use centrifugal compressors in combination with axial

stages to recover some efficiency loss. However, larger aero-engines do not make this trade-off and almost exclusively use axial compressors.

A big impeller brings about the issues of weight and stress. However, as the bypass ratio of modern mainline aircraft turbofan engines increases to improve propulsive efficiency, their engine cores are shrinking to levels where impellers of the same size as those already operating in private jets and regional aircrafts can be used.,. Thus, the remaining factors preventing the use of centrifugal compressors on main-line aircraft turbofan engines are their lower adiabatic efficiency and premature stall.

Resolving these obstacles will not only expand the use of centrifugal compressors in aircraft propulsion but will also be beneficial to many other industries using centrifugal compressors from appliances (vacuums, pumps) to ground transportation (turbochargers) and space technology (rocket pumps).

1.2 Centrifugal Compressor Aerodynamics

The overall performance of a compressor is usually presented in a compressor map, as shown in Figure 1.2. This map consists of several characteristic curves (*speedlines*), each plotting the pressure ratio versus corrected mass flow rate for a given rotational speed. Each speedline is delimited by choke on the right and stall on the left. Choke is the result of sonic flow at the throat of the blade passage. On the other hand, when the flow is reduced the axial velocity decreases leading to an increase in incidence up to a point where the flow in the blade passages eventually breaks down and compressor stall occurs.

On the compressor map, the line connecting the stall points of different speedlines is referred to as the *stall* (or *surge*) *line*. The *running line* is the line along which the compressor operates in an engine environment as its speed changes. In principle, it is set (by choking the turbine) to go through the point of maximum efficiency on the speedline associated with the compressor design speed. This point is referred to as the *design* (or *operating*) *point*. The distance between the running line and stall line is the *stall margin*. This safety margin is necessary because the stall line can move down when the engine inlet flow is distorted (e.g. due to non-axial engine inlet or cross-wind

flight) or when the clearance between the rotor blade tip and casing (*tip clearance*) increases (such as from wear as the engine ages). In addition, the running line can move up when the engine is subject to rapid acceleration and cross the stall line if the stall margin is too small. Moreover, as the design rotating speed is increased for high pressure ratio, the difference in mass flow between choke and stall also decreases, making the stall margin even smaller. If the stall margin is insufficient, one would have to lower the running line and not operate at the peak efficiency point as illustrated in Figure 1.2. If this happens, one either has to redesign the compressor or implement flow control strategies by delaying stall to a lower mass flow and thus increasing stall margin.

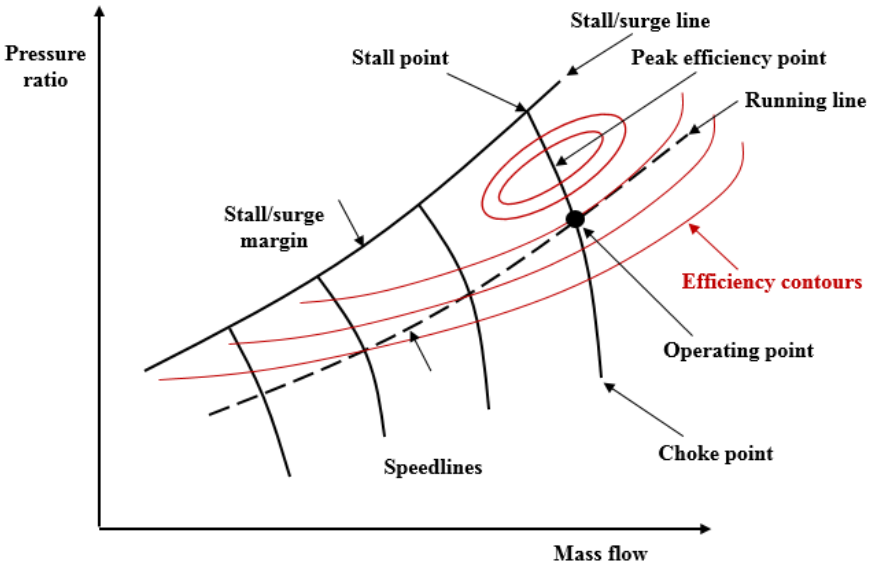

Figure 1.2: Compressor map

In order to describe the aerodynamics associated with stall in centrifugal compressors effectively, it is best to understand them for axial compressors first. Figure 1.3 shows a constant span cut of an axial compressor stage composed of a rotor and a stator. The rotor turns the flow in rotating frame and in doing so, increases the circumferential component of the absolute velocity and hence the kinetic energy and total (stagnation) pressure of the flow. The work per unit mass of air imparted by the rotor to the flow is given by the Euler pump equation (Eqn. 1.1). The stator turns the rotor exit flow toward the axial direction, slows it down (divergent flow passage) converting the kinetic energy into flow energy in the form of increased static pressure.

$$\frac{\dot{W}}{\dot{m}} = \Omega(r_2 V_{2\theta} - r_1 V_{1\theta}) \tag{1.1}$$

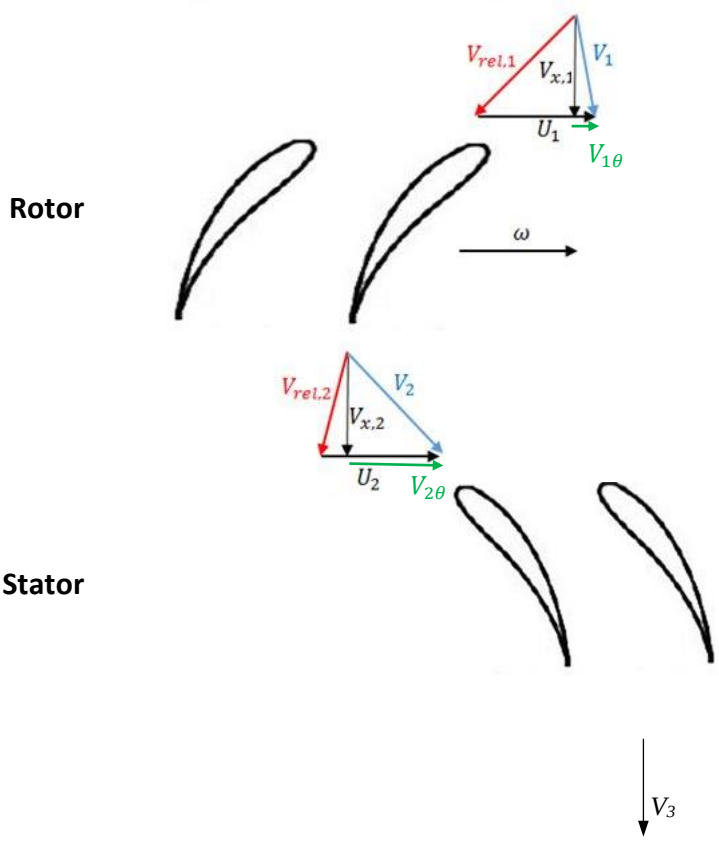

Figure 1.3: Velocity triangles in axial stage at a constant span

Figure 1.4 shows the flow structures (in relative or rotating frame) in an axial compressor rotor that affect loss and stall. These structures typically have low momentum in the (relative) streamwise direction (direction of the blade passage) and fall into three categories. The first is the blade passage boundary layers, which are the low-momentum regions on the blade and end-wall surfaces. The second is the accumulation of low-momentum boundary layer fluid at the endwall/blade junction due to secondary (cross) flow. The last is flow across the tip clearance (called *tip clearance flow* or *tip leakage flow*), which enters the passage in a direction somewhat perpendicular to that of the passage's main (core) flow resulting in region of low-streamwise momentum. Similar structures exist in a stator blade passage (in stationary frame), except the tip clearance flow, which only exists for stators with a hub clearance. The streamwise velocity deficit regions acts as an aerodynamic

blockage that decreases the effective flow area. Streamwise velocity gradient between them and the core flow generates shear and mixing losses. As can be inferred from Figure 1.3, as the mass flow decreases for a particular rotational speed (speedline), the axial velocity decreases leading to an increase in incidence on the rotor and stator blades, resulting in increased pressure rise (and thus higher positive pressure gradient) in the blade passage. The increase in pressure gradient accentuates the streamwise velocity deficit in these flow structures leading to higher blockage and mixing/viscous losses and eventually to flow reversal causing the compressor to stall. This stall takes the form of *rotating stall* which is a characterized by a region of axial velocity deficit rotating around the annulus at part of the rotor speed and usually triggers *surge*, as the compressor can no longer maintain its pressure ratio to keep the high pressure fluid in the combustor from flowing back upstream.

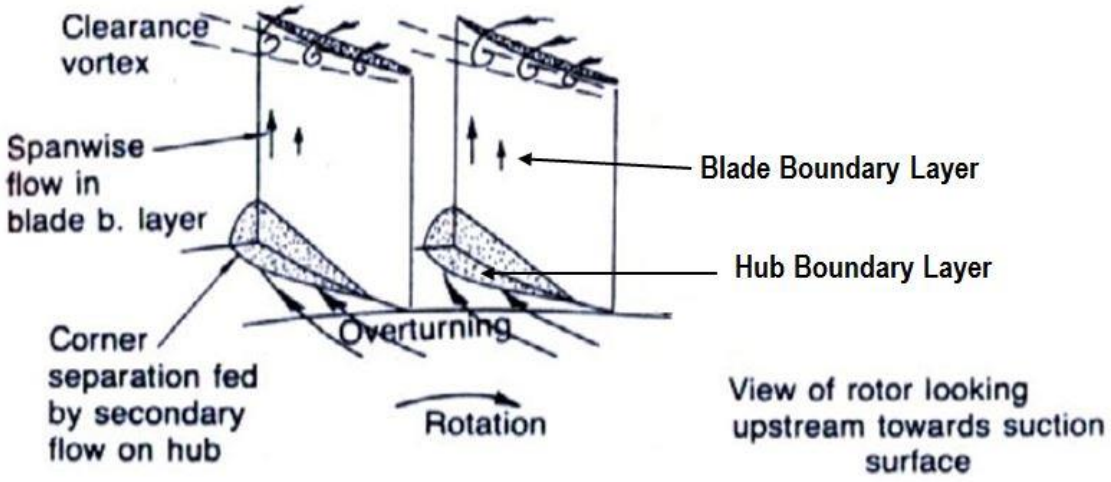

Figure 1.4: Flow structures in axial rotor passages contributing to loss (modified from [4])

All the working elements described above for an axial compressor stage are present in a centrifugal compressor but are more complex.

In terms of component functions, the impeller in a centrifugal compressor does a similar job as the axial rotor to increase the kinetic energy (and total pressure) of the flow. However, as illustrated in Figure 1.5 due to the change in radius (r) between the inlet (Station 1) and exit (Station 2) of the impeller, the change in *circumferential component of the absolute velocity* (V_θ) is much larger than that of an axial rotor in which the flow enters and exits the blade passage at about the same radius.

Thus, based on Equation 1.1, the centrifugal compressor stage provides higher work transfer to the flow and a higher total pressure rise relative to the axial stage. However, this higher circumferential velocity component at the exit of the impeller means that the diffuser needs to provide very high flow turning to bring the flow back toward the radial (and axial) direction (Station 3) relative to that in an axial stator.

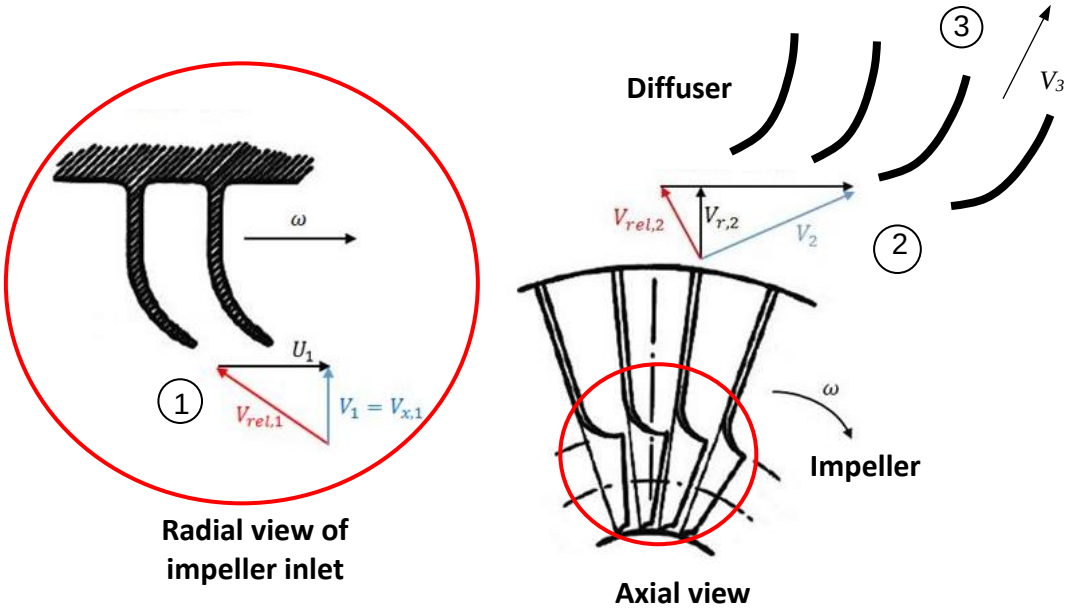

Figure 1.5: Velocity triangles for centrifugal compressor stage

In terms of flow structures, the longer blade passage and lower blade aspect ratio (blade height over chord) as well as larger pressure gradient of the impeller relative to an axial rotor results in the three low-streamwise momentum flow structures from Figure 1.4 taking up a larger volume of the blade passage. Consequently, both the core flow region and the flow uniformity at the impeller exit plane are reduced, with the latter negatively affecting the flow in the diffuser. Furthermore, due to the irrotationality of the incoming flow, the core flow velocity profile across the impeller blade passage becomes skewed as it turns into the radial direction after the impeller radial bend. Thus, the core flow itself becomes non-uniform and can induce flow separation in the exducer. Splitter blades are sometimes used to avoid this effect. These all contribute to augmented flow

complexity, aerodynamic losses and potential for flow separation in the impeller making it more susceptible to phenomenon like rotating stall relative to an axial rotor.

Moreover, relative to a stator, the very high flow turning requirement in the diffuser coupled with highly non-uniform flow coming from the impeller leads to larger boundary layers in the diffuser and a higher potential for their separation. This fact makes the diffuser a major source of loss and stall in centrifugal compressors. Thus, the diffuser is often crucial to the stability and the performance of a centrifugal compressor stage. A good diffuser design should be able to accommodate a large range of entering flow angles (i.e. stage mass flow) and also tolerate the flow non-uniformity at the impeller exit/diffuser inlet plane. Figure 1.6 illustrates the four main types of diffusers, namely vaneless diffusers, vaned diffusers, channel diffusers and pipe diffusers.

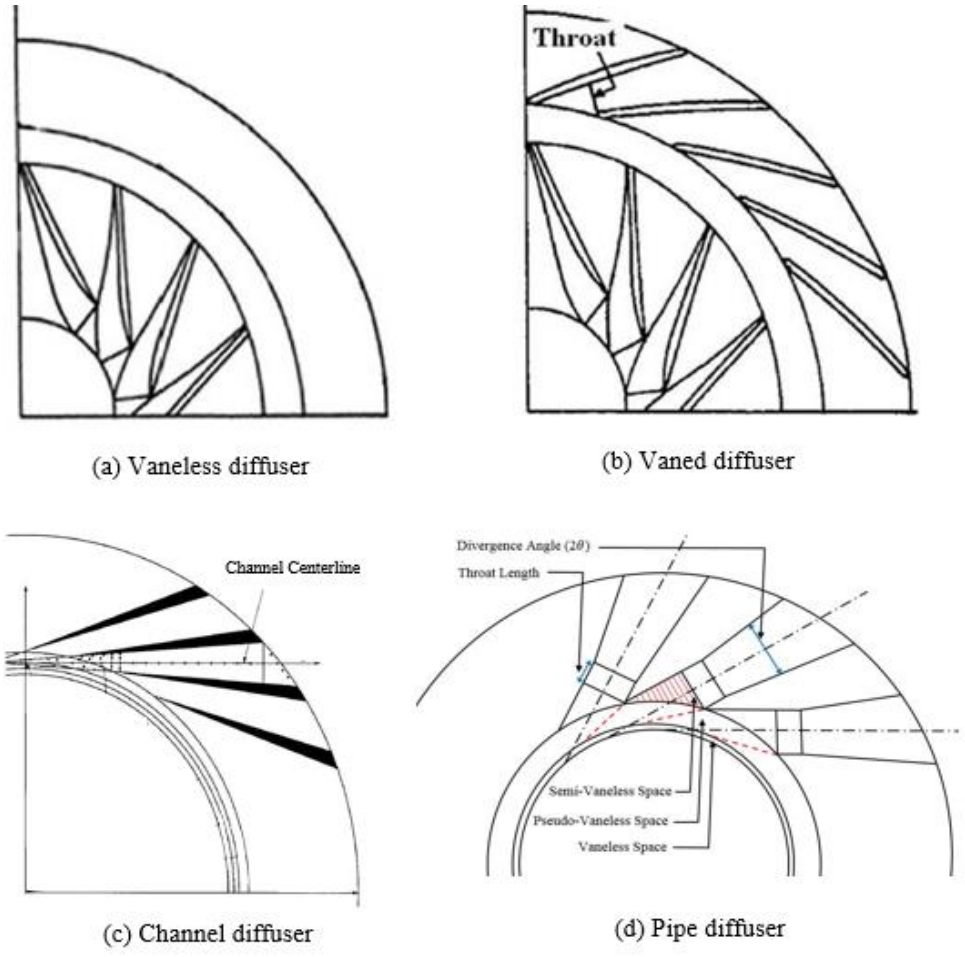

Figure 1.6: Different types of diffusers, (a) Vaneless, (b) Vaned [5], (c) Channel, modified from [6], (d) Pipe (modified from [7])

Vaneless diffusers simply consist of parallel walls without any blade elements inside. The circumferential velocity is reduced as the flow moves radially outward through conservation of angular momentum. However, this effect usually requires a large change in radius to bring the flow back close to the radial direction, which increases both viscous losses from additional wetted surface and compressor frontal area, neither of which is desirable in aircraft engine applications.

Vaned diffusers incorporating thin curved vanes or airfoils, decelerate/reorient the flow over a shorter radial distance than vaneless diffusers, resulting in a lower exit radius and lower losses (higher stage efficiency). However, they are mechanically more complex and heavier with a narrower operating range/stall margin [8].

Channel diffusers use straight wedge-shaped vanes to produce discrete diverging passages. They exhibit similar performance advantages/issues as vaned diffusers but have a larger frontal area.

Finally, pipe diffusers use divergent pipes to decelerate the flow exiting the impeller. Commonly used in modern centrifugal compressor stages, their distinguishing geometrical feature is the additional area within the pseudo-vaneless space which contains elliptical ridges formed by the intersection of two adjacent pipes, as illustrated in Figure 1.6 (d). This feature provides an additional path for diffusion as described in the work by Kenny [9] and also in one of the patents on this type of diffusers in 1986 by Bryans [10]. Centrifugal compressors with pipe diffusers are characterized by their wide operating range/stall margin and relatively high stage efficiency [7].

A subcategory of pipe diffusers often used in aircraft engines, particularly by Pratt & Whitney Canada, is the "*fishtail"* pipe diffuser. As shown in Figure 1.7, following the throat, the cross section of the pipe becomes oblong and changes the shape from circular to almost oval (two semi-circles connected by straight lines) and the pipe wraps gradually from the radial-circumferential direction to the axial direction with continuous area increase. This wrapping allows for turning the flow both radially and axially toward the direction of an axial combustor in an aircraft engine in a single diffuser stage, thus minimizing the compressor frontal area. Combined with their relatively low losses, fishtail diffusers are ideal for aero-propulsion applications.

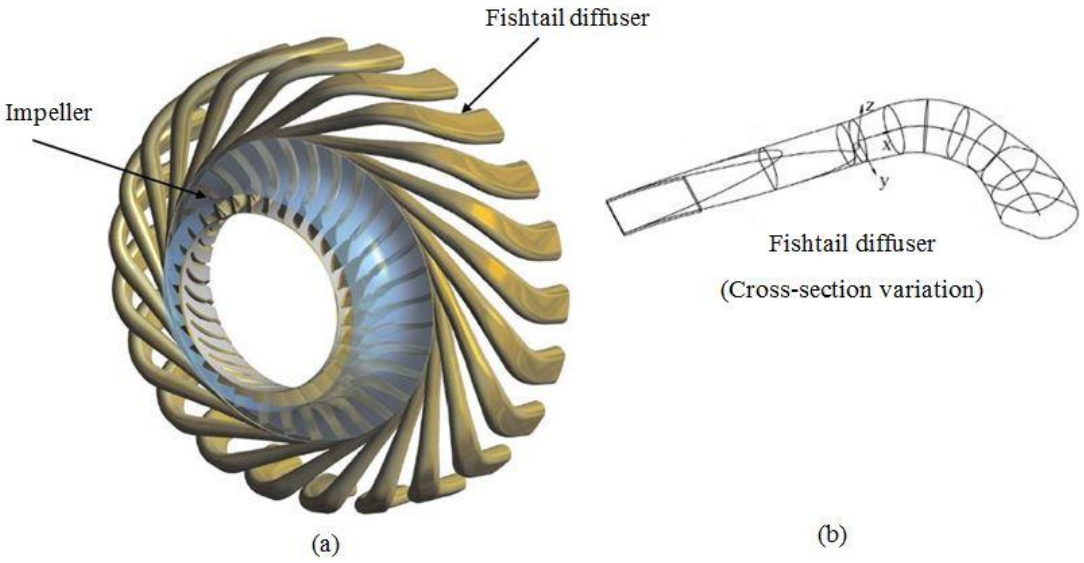

Figure 1.7: (a) Schematic of a centrifugal compressor stage with *fishtail* pipe diffusers [11], (b) fishtail cross-Section variation (modified from [12])

1.3 Problematic

Different passive flow control techniques (i.e. not requiring energy input) have been applied to delay stall in centrifugal compressors. They mostly involve placing flow control devices, such as slots [13], ported shrouds [14] and recirculation pipes [15, 16] in the leading edge of the impeller, as illustrated in Figure 1.8, perhaps because it is the simplest place to put them in terms of fabrication constraints and mechanical integration. It must also be noted that none of these past studies involve compressors with fishtail pipe diffusers.

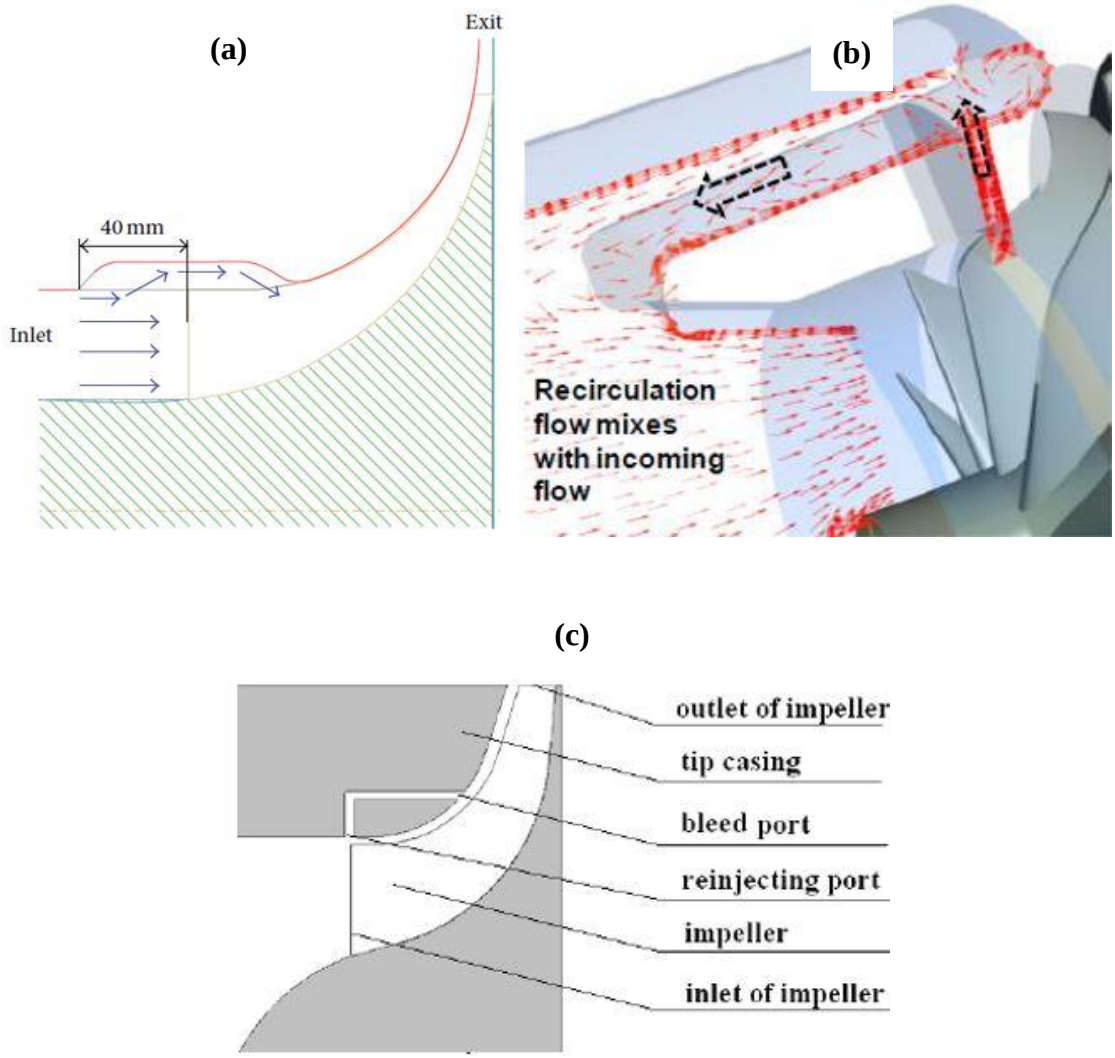

Figure 1.8: Schematic of flow control at impeller leading edge region using (a) slots [13], (b) ported shroud [14] and (c) Recirculation pipe [15]

Although these studies have shown some success in delaying stall, this flow control location may not be practical nor optimal. In an engine environment where the centrifugal compressor may be preceded by many axial stages, the spacing between the impeller and the upstream blade row might be very small. As such, the flow control device might infringe upon or be hindered by the stator immediately upstream of the impeller. Moreover, a study by Eckardt [17] indicated that the flow non-uniformity in the tip region of the impeller, which would be most affected by a flow control device placed on the shroud, really starts to increase in size after the radial bend, as shown in Figure

1.9. Moreover, the flow physics described in Section 1.2 point to the exducer and diffuser as more likely locations for the initiation of stall. As such, a flow control placed on the shroud at or near the radial bend, as illustrated in Figure 1.10, may be more effective in affecting flow features at the exducer and in the diffuser that lead to stall. Indeed, applying the control at the radial bend, can not only improve the flow uniformity inside the impeller exducer, but also will improve the flow uniformity at the impeller exit/diffuser inlet plane and hence inside the fishtail diffuser, both having a direct positive impact on delaying stall.

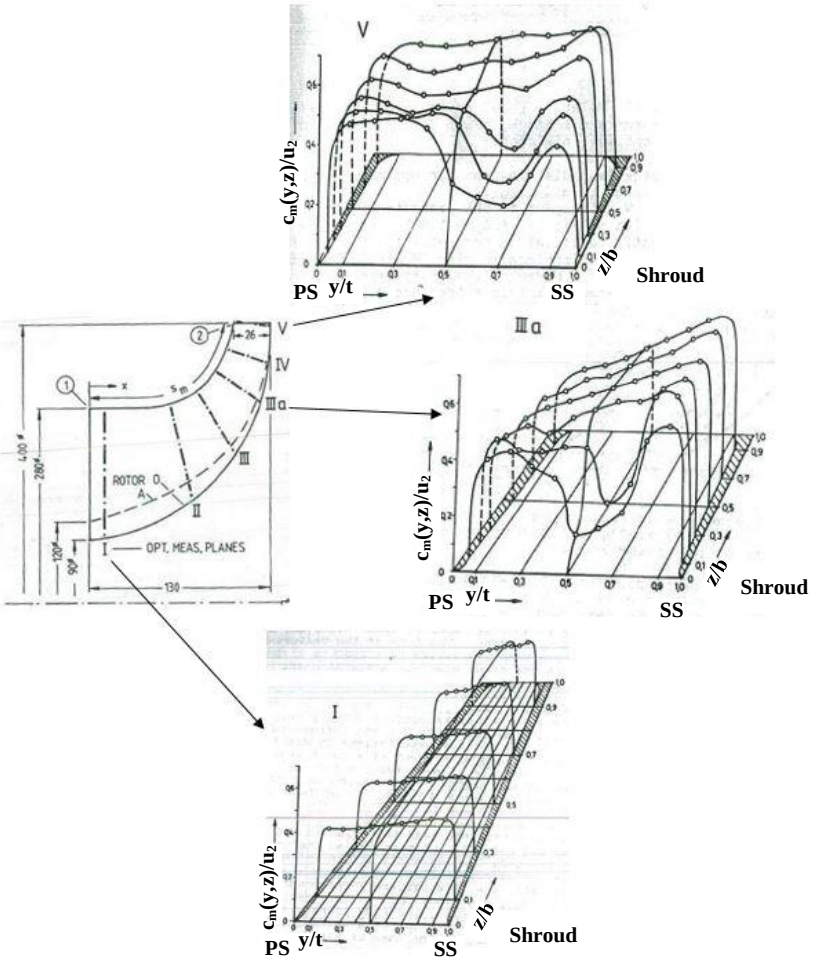

Figure 1.9: Flow evolution in impeller passage [17]

Moreover, as shown in Figure 1.10, the radial bend region of the shroud provides a more convenient physical access to incorporate the flow control devices than does the impeller leading edge region. Finally, while traditional manufacturing constraints may have rendered placing slots and grooves

at the impeller radial bend more difficult and costly, the advent of additive manufacturing not only negates these constraints but also allows for the possibility of implementing even more complex flow control devices such as flow return channels from the diffuser to the impeller integrated into the casing.

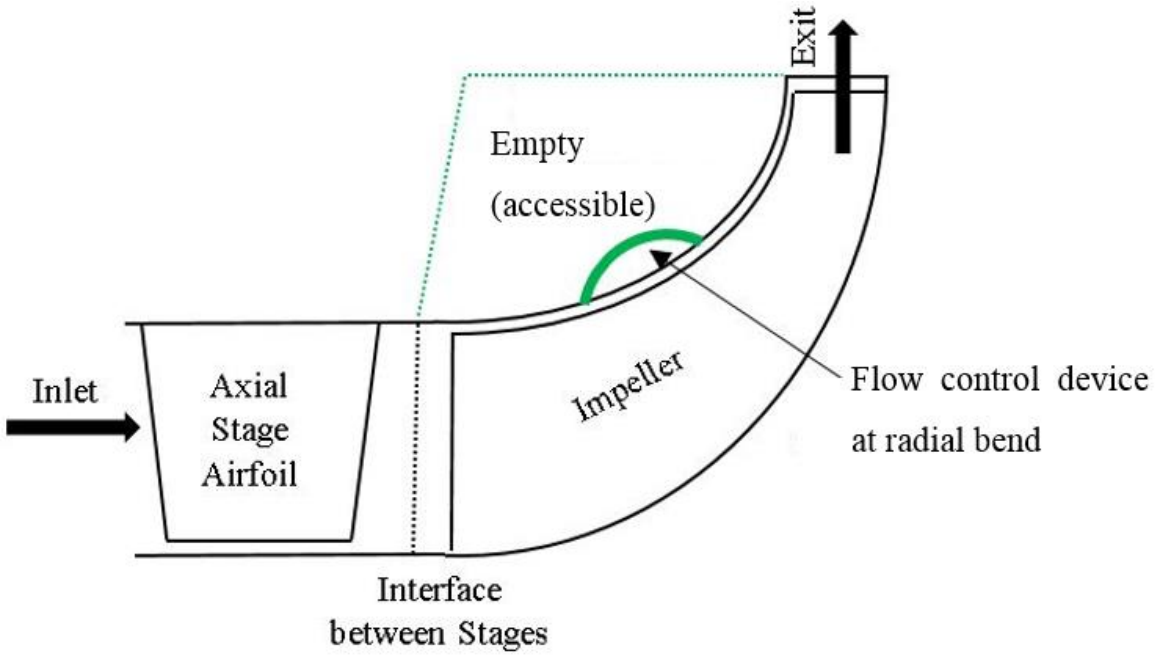

Figure 1.10: Schematic of the available empty space at radial bend for effective use of flow control

The research questions are:

1) Is passive flow control implemented on the shroud of the impeller at the radial bend effective in improving stall margin for centrifugal compressors with fishtail pipe diffusers?

2) In the affirmative, what characterizes effective passive flow control techniques at the radial bend?

3) What is the effect of these flow control techniques on the stage efficiency at the design point?

1.4 Objectives

Thus, the general objective for this research is to assess the effectiveness of passive flow control devices placed at the impeller radial bend in terms of stall margin improvement and efficiency penalty for centrifugal compressors with fishtail diffusers.

The specific objectives can be stated as follows:

1) Assess the effectiveness of passive flow control on the shroud at the impeller radial bend for stall margin improvement in centrifugal compressors with fishtail diffusers through evaluation of different flow control devices at this location
2) Elucidate the flow mechanism by which effective passive flow control at the impeller radial bend delays stall
3) Assess the impact of these flow control devices on losses and compressor isentropic efficiency at the design mass flow

1.5 Thesis Outline

This thesis consists of six Chapters. Following this introduction, Chapter 2 summarizes the pertinent literature on the design and characteristics of centrifugal compressors with fishtail pipe diffusers and the effective flow control techniques applied to improve centrifugal compressors' stall margin and performance. The methodology chosen to reach the research objectives is presented in Chapter 3. Chapters 4 and 5 show the results for two centrifugal compressors with different stall mechanisms. Finally, Chapter 6 summarizes the conclusions and lists the suggestions for the future work.

CHAPTER 2 LITERATURE REVIEW

In order to design effective flow control strategies which can improve the operating envelope of centrifugal aero-compressors, one must investigate and understand the flow physics within a centrifugal compressor stage that are responsible for limiting the stall margin. Moreover, given very few publicly available references on compressors with fishtail pipe diffusers, this literature review will cover centrifugal compressors in general and include material on other compressors that may be relevant to the present research.

This chapter starts with a review of the flow physics, loss mechanisms and aerodynamic performance associated with centrifugal compressors. Thereafter, an overview of the flow control strategies is presented, describing their potential to improve the stall margin and performance of centrifugal and other types of compressors.

2.1 Stall Mechanisms in Compressors

2.1.1 Centrifugal Compressors

While many studies have been carried out on rotating stall for axial compressors, very few such studies have been done on centrifugal compressors. This section summarizes these studies while stall studies for axial compressors will be reviewed in Section 2.1.2.

In one of the first extensive references, Japikse [18] summarized the works done prior to 1998 on rotating stall in centrifugal compressors. This summary identified three types of rotating stall associated with impellers: mild impeller rotating stall, abrupt impeller rotating stall and progressive impeller rotating stall as well as vaneless diffuser rotating stall. While no clear explanation is given for mild impeller rotating stall, abrupt impeller rotating stall is identified by large velocity and pressure amplitude perturbations upstream and downstream of the impeller prior to stall. However, the author noted that mild impeller rotating stall can initiate vaneless diffuser rotating stall. Moreover, progressive impeller rotating stall is not well-known except that it is characterized by progressive growth of the amplitude of the oscillations. According to this summary, impeller

rotating stall is dependent on the impeller outlet blade angle, tip incidence and leading edge to throat velocity ratio, while no criteria was established to predict the stall onset. Inside the diffuser, rotating stall occurs in vanless diffusers or the vaneless part of vaned diffusers, and is affected by diffuser length, vaneless extent, inlet-to-throat area ratio, number of vanes and vane design for vaned diffuser.

Eckardt [17] was the first to perform a detailed measurement of the 3-D flow within an impeller passage. As highlighted in Section 1.3 and illustrated in Figure 1.9, his study revealed a region of low-momentum flow near the casing just downstream of the radial bend and on the blade suction side, this region, which persists to the impeller exit region, affects the flow uniformity entering the diffuser where a large portion of the loss due to the interaction between the two components is generated. Eckardt also states that rapid growth of boundary layers is a frequent occurrence in the exducer which can lead to suction side flow separation and unsteady flow in the diffuser. One can thus infer that the low-momentum flow structure identified by Eckardt can lead to both impeller stall and/or diffuser stall.

Ibaraki *et al.* [19] studied the effect of tip clearance flow within a transonic impeller of a turbocharger compressor with vaned diffuser. Their results showed that the design of the inducer is critical, as it is responsible for shock waves, which is another source of total pressure loss. Their experimental measurements with Laser Doppler Velocimetry at different locations and corresponding results from CFD simulations, as presented in Figure 2.1, showed that the interaction of the leakage vortex with shock wave creates a region of low-momentum flow (blue region) near the shroud. Their analysis of the CFD simulations further showed that this interaction can enhance total pressure loss of the tip vortex core downstream of the inducer. Their results also indicated that there is a low-velocity region formed by tip leakage flow and local regions of reversed flow at the impeller exit which can affect the flow uniformity inside the diffuser and the incidence on diffuser vanes and can trigger stall if not controlled.

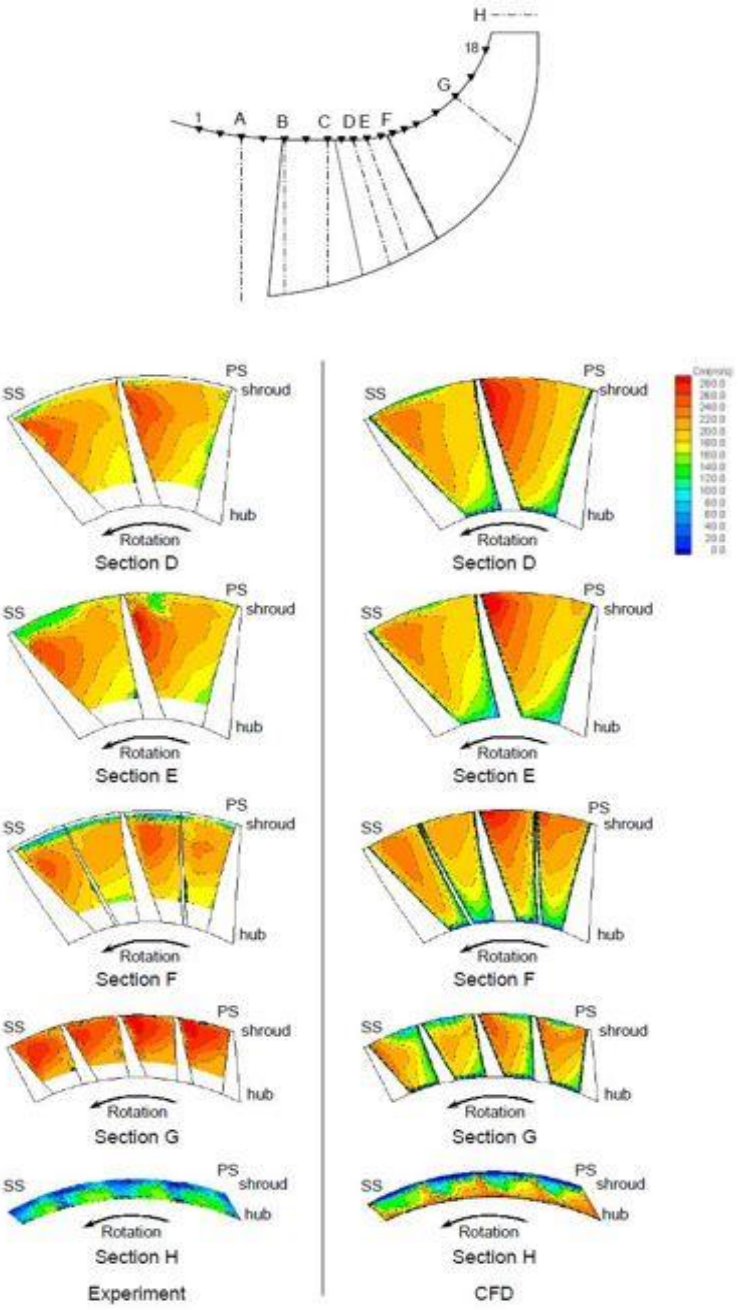

Figure 2.1: LDV measurement stations and meridional velocity distribution at five sections [19]

In another numerical study using a commercial CFD code, Kaneko and Tsujita [20] considered the effect of tip leakage flow in a transonic centrifugal compressor impeller. Their results revealed that the loss generation and stall onset in the transonic centrifugal compressor impeller with tip clearance is influenced by three factors: (1) impeller blade suction side boundary layer separation

downstream of the shock wave; (2) interaction of shock wave with the tip vortex at the main blade leading edge region; and (3) tip vortex attenuation from the splitter blade leading edge due to high loading and large positive incidence angle on the splitter blade leading edge. Through comparison with a shrouded impeller (no tip clearance), the authors showed that despite the losses incurred from tip leakage flow the presence of the tip clearance is overall beneficial because the resulting tip blockage reduces the incoming flow velocity in the tip region. As such, the strength of the shockwave and its associated losses as well as the probability of stall are reduced.

In a numerical study validated by experimental measurements in 2014, Ashrafi *et al.* [21] simulated a centrifugal compressor with vaneless diffuser which was part of a two-stage low-speed axial-centrifugal compressor. In an attempt to delay stall in the centrifugal compressor stage, it was revealed that the stall in this centrifugal compressor stage was associated with the tip clearance flow spillage ahead and below of the impeller tip at leading edge. This happens once the interface between the incoming and tip clearance flow aligns with the impeller leading edge plane. As such, the impeller inducer in this study exhibited a similar stall inception behaviour as that of tip critical axial rotors, which are described in more detail in Section 2.1.2.

Diffuser performance is dependent upon impeller exit flow conditions, whereas the diffuser back pressure also has an effect on the impeller exit flow. Anish *et al*. [5] performed a numerical study on the impeller diffuser interaction in a low-speed centrifugal compressor using two different vaned diffusers with different solidities. It was understood from their results that the main parameter influencing the unsteady behaviour of the flow within the diffuser is the circumferential variation of flow angle at the diffuser vane leading edge which is linked to the circumferential flow variation in the impeller exit flow. They found that the steady-state and unsteady performance of the diffuser are influenced by the spanwise variation and circumferential variation, respectively, of the flow angle at the diffuser inlet. The circumferential variation of the flow inlet angle leads to fluctuations in the diffuser vane loading which, in turn, triggers unsteady vortex shedding (and associated energy and pressure losses) that causes variations in diffuser pressure recovery and may lead to diffuser stall. The interaction effects were found to be stronger in the vaned diffuser with higher solidity and at off-design conditions, where the diffuser blade loading would be higher.

The studies mentioned in the previous Section were mostly on vaneless and vaned diffusers, only a few studies have focused on the concept of pipe diffusers.

Kenny [9] performed pioneering research on the concept of pipe diffuser which first appeared in the patent by Vrana in the 1960s [22]. This concept is essentially the first version of the fishtail diffuser concept. Kenny [9] compared this pipe diffuser concept with cambered-vane and flat-plate diffusers, all shown in Figure 2.2. The pipe diffuser consisted of a set of discrete drillings arranged in a symmetrical array within a radial plane followed by a "*diffusing trumpet*" (similar to the aft part of the current fishtail diffuser), as shown in Figure 2.2 (c) and (d). This pipe diffuser exhibited an efficiency improvement over conventional vanned diffusers on the order of 8 percent at 6:1 pressure ratio.

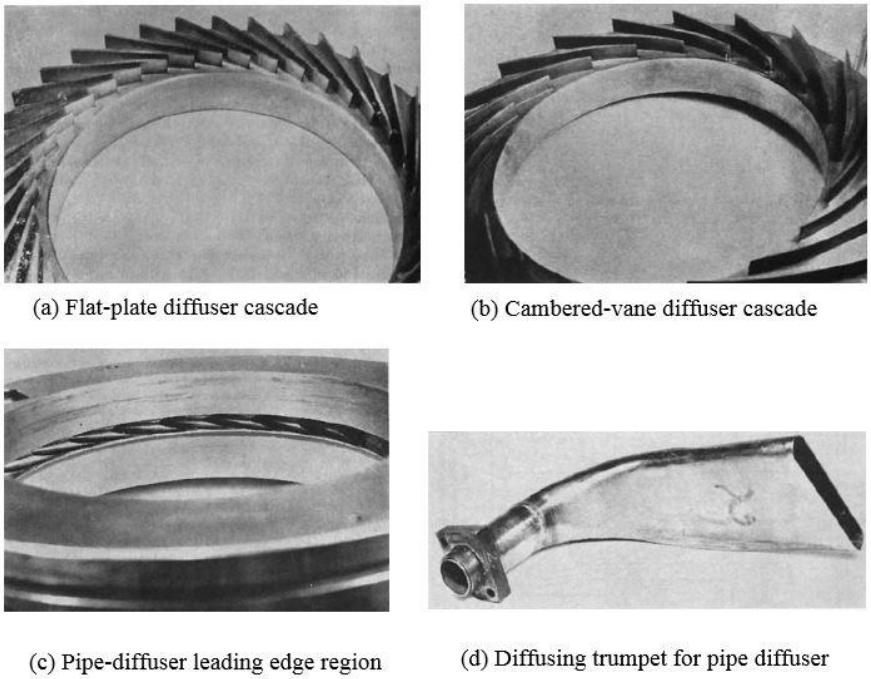

Figure 2.2: Different types of diffuser studied in the work by Kenny [9]

According to Kenny [9], the pseudo-vaneless space (unique to pipe diffusers) formed by the intersection of two adjacent pipes, containing elliptical ridges/scalloped leading edge, provides an additional area for diffusion. This inherent leading edge provides the pipe diffuser with a better tolerance of the misalignment between the inlet flow angle and vane angle and an ability to adapt better to high subsonic Mach number inlet flow, resulting in a wider operating range and higher stall margin. Due to the small gap between the impeller exit and diffuser inlet and the specific

geometry of the pipe-diffuser (pseudo-vaneless area and ridges), there is an intense impeller-diffuser interaction with very highly non-uniform flow leaving the impeller and entering the diffuser. In a transonic environment with supersonic inlet Mach number, this can lead to strong gradients, strong secondary flows, vortical structures and stall.

Grates *et al.* [23] did a numerical investigation validated by experimental measurements on the unsteady flow inside a centrifugal stage with pipe diffusers. They showed that the geometry specific to a pipe diffuser leading edge creates a pair of counter-rotating vortices shown in Figure 2.3. The first vortex on the front wall/shroud oscillates in time and is generated by the temporal incidence variation on the leading edge as the impeller passes by, similar to other bladed radial diffusers. However, the second vortex on the back wall/hub, which is constant in time, is generated by the ridge, which operates as a vortex generator. These vortices tend to direct the high-momentum flow toward the pressure side of the diffuser and move the low-momentum fluid from the pressure side wall into the middle of the pipe. The continuous sequence of jet and wake flow passing over the diffuser leading edge will result in a reduced aerodynamic blockage in the throat. The effect of unsteady flow within the impeller and diffuser was also investigated separately. The unsteady flow inside the impeller favours mixing between the low-momentum tip clearance flow and the high-momentum core flow, thus reducing the associated blockage. In addition, pipe diffusers have a fairly strong upstream effect and can alter the local pressure field at the impeller exit by $\pm 5\%$. It was also found that the diffuser has to cope with strong variations of about ten degrees in its inlet flow angle due to the circumferential variation of the impeller exit flow. The resulting flow unsteadiness in the diffuser also improves mixing between low and high-momentum fluid, thus diminishing the blockage in the diffuser throat. As such, one can infer from this work that flow unsteadiness may be beneficial to stall margin. The authors also invoke the fact that it is the diffuser characteristic that determine the surge (stall) and choke points and thus operating range of the stage.

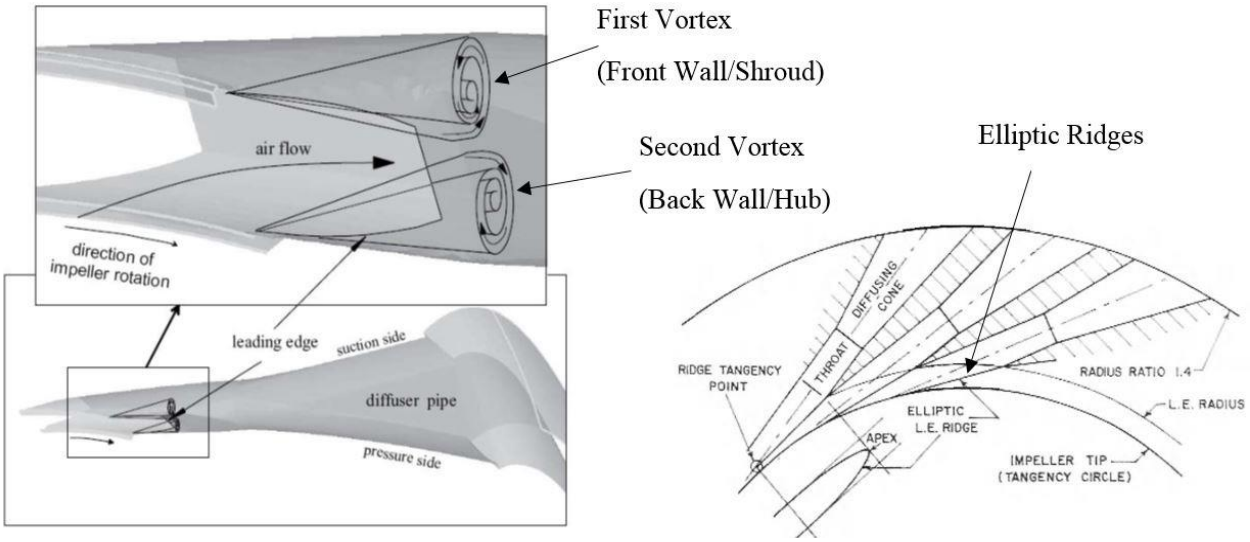

Figure 2.3: Vortex generation inside the pipe [24]

Zachau *et al.* [24] carried out an experimental study on the effect of these vortical structures in the pipe diffuser of a centrifugal compressor stage, but they could not conclude whether these vortices had a positive or negative impact on the losses in the diffuser. Their work considered the effect of impeller tip clearance size, different bleeds from the impeller and the axial misalignment between the impeller exit and diffuser inlet. They found that the boundary layer separates on the pressure side for the first half of the diffuser for all stable operating points. In addition, it was found that for all configurations studied the flow hardly decelerates for the last 30% of the diffuser.

The studies on the flow physics mentioned above were considering straight pipe diffusers (purely radial-circumferential) rather than the more complex fishtail design.

2.1.2 Other Types of Compressors

The study by Moore [25] in 1980s and later on by Moore and Greitzer [26] on a multi-stage compressor modeled as an actuator disk with flow inertia was one of the first studies to elucidate the stall mechanism for axial compressors. This study revealed that when the total-to-static pressure rise versus mass flow rate curve or the speedline of the compressor reaches a positive slope, the naturally occurring perturbations in the flow would grow to fully-developed rotating stall cells due

to negative damping. This type of stall inception which was experimentally verified is called long length-scale (or modal) stall inception.

Another type of rotating stall onset is referred to as short length-scale (or spike) stall inception was first discovered experimentally in the 1990s by Day [27]. This type of stall inception is characterized by the sudden appearance, localized nature and rapid evolution of a short-length scale perturbations at the rotor tip into a rotating stall cell is more common in modern axial compressors. Moreover, due to its characteristics, it is hard to predict its onset. Later on, Camp and Day [28] noticed that spike stall inception occurs once the flow near the blade tip reaches a critical incidence. However, the generic value of this critical incidence as well as its associated span location were not quantitatively specified.

Vo *et al.* [29, 30] proposed the first quantitative criteria to capture spike stall inception in axial compressors that were later confirmed with experimental observations by other researchers. The proposed criteria was based on the tip clearance flow, which is the high-entropy flow in the small gap between the rotor tip and the casing. This flow is driven by pressure difference between the pressure and suction sides of the rotor and contributes to the loss in pressure rise and efficiency. This flow exiting the tip gap meets the low-entropy incoming flow and forms an interface and a region of high entropy gradient. Moving to lower mass flow rates on the compressor speedline, the axial velocity decreases and hence the incidence on blade row increases. This will increase the pressure difference and results in increased tip clearance flow momentum and decreased incoming flow momentum. The momentum imbalance drives the incoming/tip clearance flow interface upstream toward the leading edge.

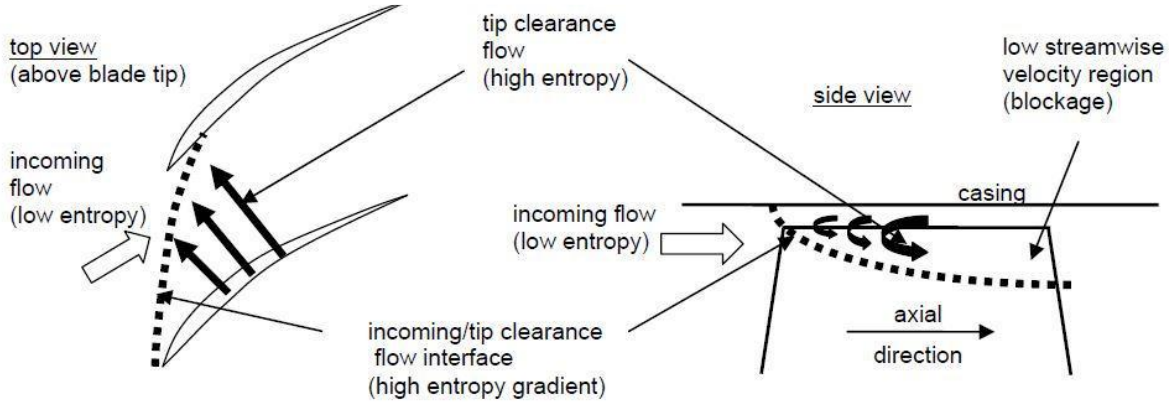

Figure 2.4: Interface between incoming flow and tip clearance flow [29, 30]

Two criteria are proposed for spike stall inception in [29, 30], as shown in Figure 2.5. The first is the incoming/tip clearance flow interface reaching the leading edge, marking the onset of tip clearance flow spillage below and ahead of the blade tip leading edge into adjacent blade passage, as illustrated in Figure 2.5. The second criterion is tip clearance fluid backflow at the trailing edge below the tip, impinging on the adjacent blade's pressure side, as illustrated in Figure 2.5 (b). Both criteria were said to be required for spike stall inception. Spillage of tip clearance flow (criterion 1) provides the path of lower resistance for tip clearance fluid, more so than downstream convection or entering the adjacent blade tip clearance (double leakage). Hence, the impinged tip clearance backflow at the trailing edge can move upstream across the entire passage and form a spike perturbation and then stall. Vo *et al.* [29, 30] showed that delaying one of the two criteria, would delay stall to a lower mass flow until both criteria are satisfied. The authors suggested that if the two criteria occur before the zero-peak of the compressor speedline, the compressor would exhibit spike stall inception. Otherwise, it would exhibit modal stall inception. The authors also concluded that tip clearance flow losses could make the speedline turn over to its peak or zero-slope and generate modal stall inception before the spike criteria are satisfied.

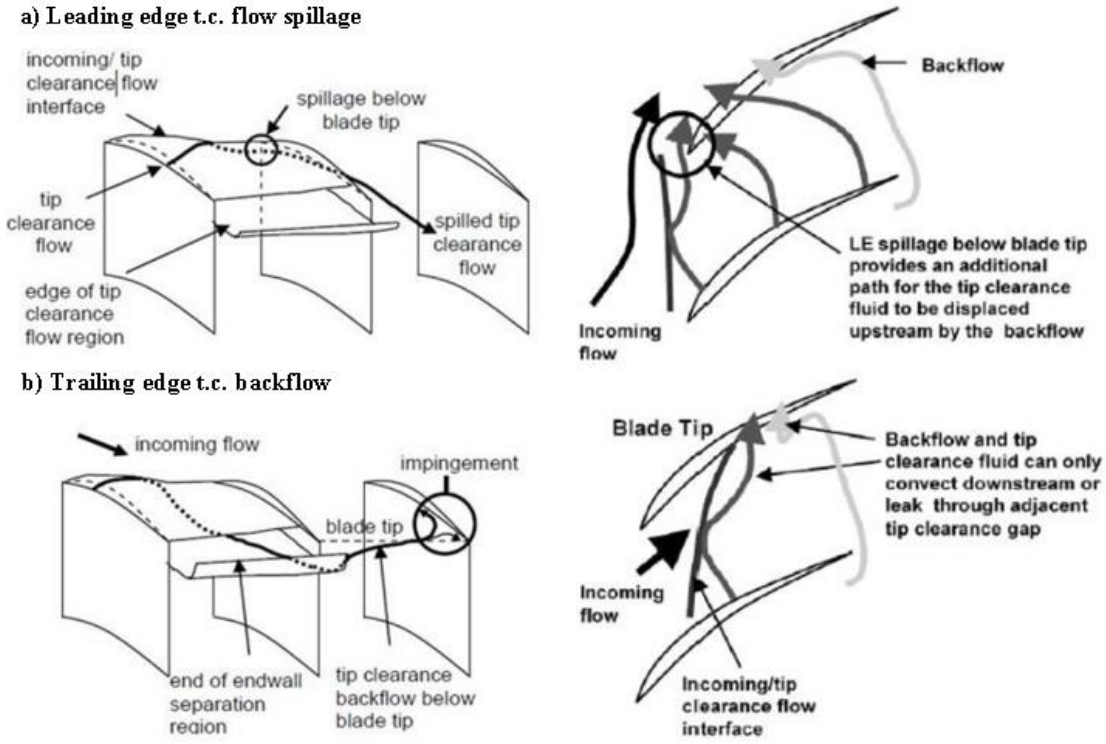

Figure 2.5: Proposed criteria and mechanism for spike stall inception, modified from [29, 30]

Different studies have tried to validate the criteria proposed by Vo. The experimental study by Deppe *et al.* [31] on three low-speed axial compressor stages and the numerical study by Hah *et al.* [32] on a high-speed axial compressor corroborated both criteria. However, most other studies such as the experimental work by Cameron and Morris [33] on a high-speed axial compressor stage and the numerical work by Djeghri *et al.* [34] on a mixed-flow compressor rotor only focused on and corroborated the leading edge tip clearance spillage criterion.

2.2 Strategies for Improving Compressor Stall Margin

The following section reviews strategies found in the published literature for delaying rotating stall, starting with centrifugal compressors in Section 2.2.1, followed with the studies for other compressors that could also be beneficial for the research. The focus is on passive flow control which does not require power input and is of interest in the current research. The stall margin extension for this work and all the other cited works in this review are calculated as the difference

between the stall point corrected mass flow of the configuration with the flow control and that of the baseline (no flow control) divided by the corrected mass flow of the baseline stall point.

2.2.1 Centrifugal Compressors

As explained in the previous sections, the flow uniformity in centrifugal compressors within the impeller and diffuser as well as the impeller and diffuser interaction play a key role in stage performance and stall margin. Therefore, to extend stall margin, most techniques investigated so far focus on reducing aerodynamic blockage regions within the impeller and increasing impeller exit flow uniformity to improve flow within the diffuser. These techniques fall under two categories: retroactive strategies that do not involve redesign of the impeller, and impeller blade design optimization.

Retroactive Flow Control Strategies

Sitaram and Swamy [35] performed an experimental investigation on the effect of turbulence generators and partial shroud on the efficiency and performance of a low-speed centrifugal compressor. The turbulence generator is a flow tripping device attached to the shroud at different distances upstream of the rotor to generate a turbulent endwall boundary layer, while the partial shroud was placed at different positions along the chord, as illustrated in Figure 2.6. The compressor used a vaneless diffuser and the impeller was tested at three different tip clearance values: 2.2%, 5.1% and 7.9% of impeller exit blade height. Results show that configurations with turbulence generator increased the compressor operating range more substantially. However, configurations with partial shroud have higher specific work and efficiency compared to the other configurations.

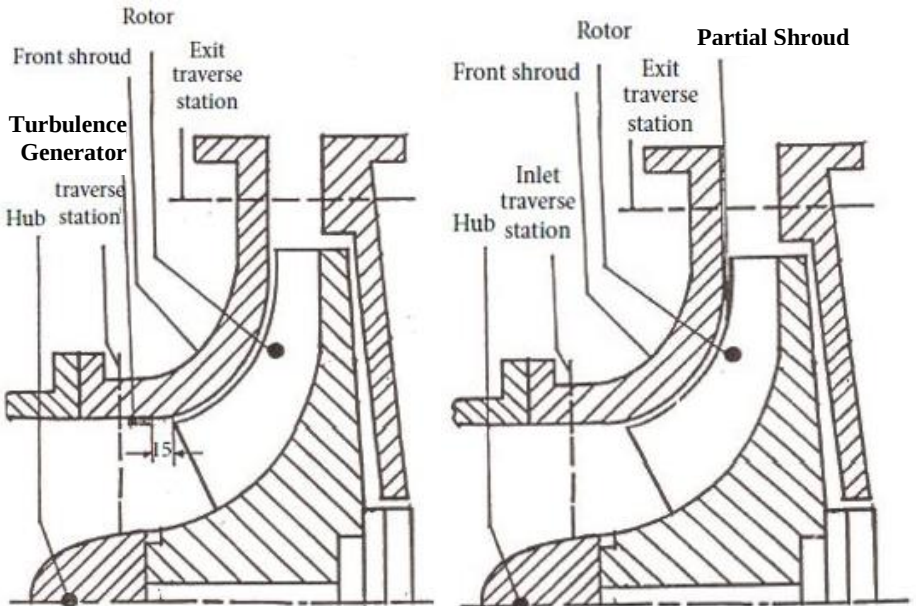

Figure 2.6: Details of tested configurations for turbulence generators and partial shroud, modified from [35]

In another study, Zheng *et al.* [16] applied a non-axisymmetric self-recirculation casing treatment to improve the surge margin of a high-pressure ratio turbocharger centrifugal compressor with inlet distortion. The self-recirculation casing treatment consists of almost discrete (lightly connected) Sections of circumferential recirculating grooves (as shown in Figure 2.7) placed at different axial locations in a sinusoidal pattern around the circumference. The injection side is always upstream of the impeller leading edge and the suction side downstream of it. By reducing the inlet flow distortion, they could obtain a 10% lower surge flow rate compared to the axisymmetric self-recirculation casing treatments. The largest surge margin improvement is obtained when the largest distance between main blade leading edge and rear groove has a coincident phase with the minimum static pressure near the splitter blade leading edge.

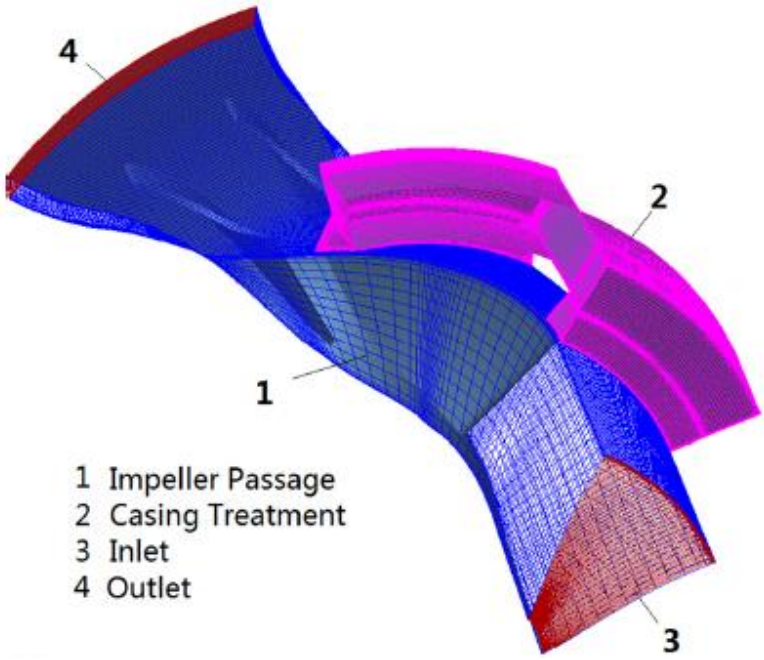

Figure 2.7: Schematic of a self-recirculation casing treatment in a turbocharger centrifugal compressor [16]

In a numerical investigation of the effect of inducer slots casing treatments on the stall margin and performance of a high speed centrifugal compressor with vaneless radial diffuser and a pressure ratio of 4, Koyyalamudi *et al.* [13] assessed three configurations of casing treatments differing in their inlet shapes as shown in Figure 2.8. Each configuration features four slots per blade passage. All the three configurations improved the choke margin by 9.5% because of increased inlet flow area. However, the configuration in Figure 2.8 (a) could improve the stall margin by 18% through energizing and pushing the weakened low-momentum fluid near the shroud downstream, while reducing the peak efficiency by 0.8%. The other two configurations were not as successful in terms of stall margin improvement while also reducing the peak efficiency by 1%.

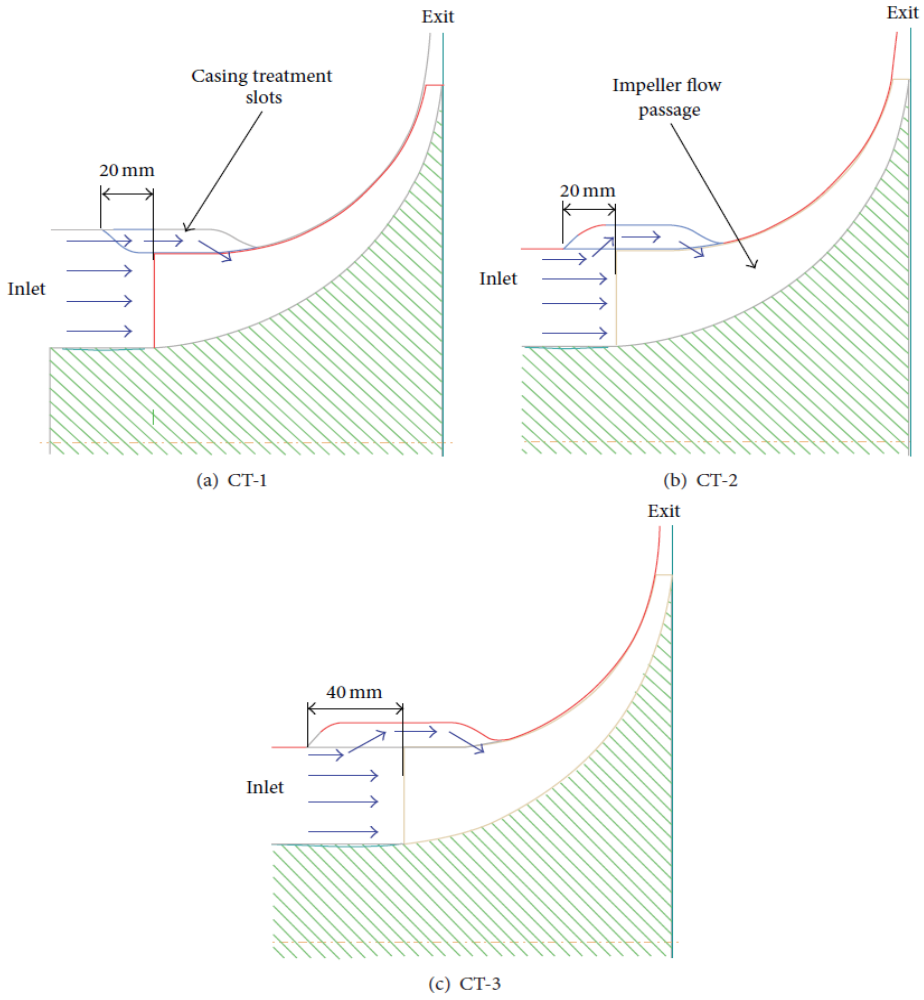

Figure 2.8: Inducer casing treatment configurations in meridional plane [13]

Wang *et al.* [15] numerically simulated and experimentally tested a self-adaptive casing treatment for a turbocharger centrifugal compressor stage with vaneless diffusers, as shown in Figure 2.9. This type of casing treatment includes a set of discrete round holes within the stationary shroud. It bleeds air at operating points near stall due to the larger pressure gradient and much less so away from stall to decrease losses and improve design point efficiency. The results show that unsteady reinjected flow re-directs the low-momentum fluid near the casing and in the tip region in the streamwise direction to reduce positive incidence angle and suppresses flow separation at the tip of the impeller leading edge. This enhances the stable range. With this mechanism a stall margin extension of up to 20% is achievable with 0.2% to 1.5% efficiency improvement over the entire operating range.

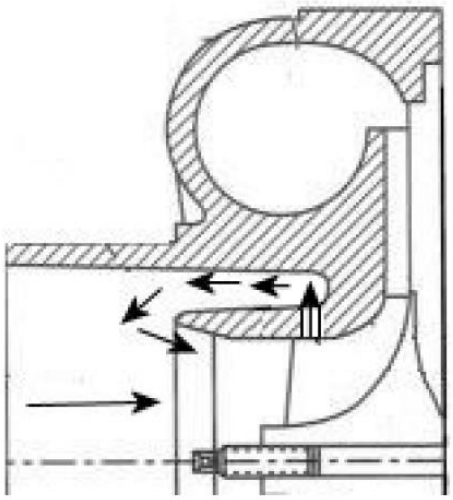

Figure 2.9: Self-adaptive bleeding recirculation casing treatment for turbocharger centrifugal compressor [15]

In an experimental investigation, Skoch *et al.* [36] tested two different methodologies to extend the surge margin of a high-speed 4:1 pressure ratio centrifugal compressor with a vaned diffuser, as illustrated in Figure 2.10. These two techniques: flow injection into the shroud of the diffuser vaneless space (Figure 2.10 (a)) and flow obstruction using control tubes (Figure 2.10 (b)). These techniques aim to reduce the span-averaged swirl angle inside the diffuser vaneless space which in turn reduces incidence on the diffuser vane leading edge and eliminates unsteady flow separation on the vanes of the diffuser responsible for stall. The flow injection technique was tested in two different configurations. The first is forward-tangent injection with recirculated air from the diffuser discharge which resulted in a modest 3.7% surge margin improvement and a slight diffuser pressure loss. The second configuration is reverse-tangent injection using external air to provide required pressure margin for injection which resulted in a 10.2% stall margin improvement at low injected flow rate and a large diffuser pressure loss. The control tubes technique with capped outer port flow obstruction only, could provide 13.4% in stall margin extension with moderate diffuser loss. The stall margin extensions are inferred from the speedlines.

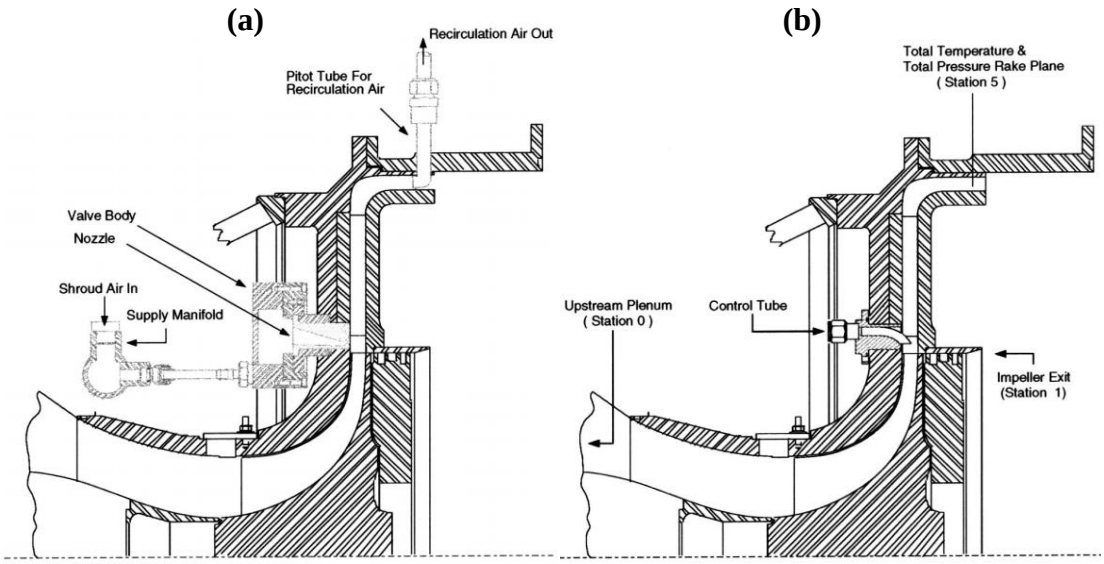

Figure 2.10: Cross section of test compressor with (a) air injector and (b) control tube ([36]

Chen *et al.* [14] reviewed the impact of ported shrouds for centrifugal compressors, a technology mainly used in turbochargers for more than twenty years. Figure 2.11 shows the mechanism of ported shroud near surge. The authors explain that as the mass flow reduces and back pressure increases, backflow occurs along the shroud tip clearance region that causes stall if it reaches the impeller leading edge. A ported shroud extends stall margin by removing the low-momentum fluid near the shroud and reinjecting it at the inlet.

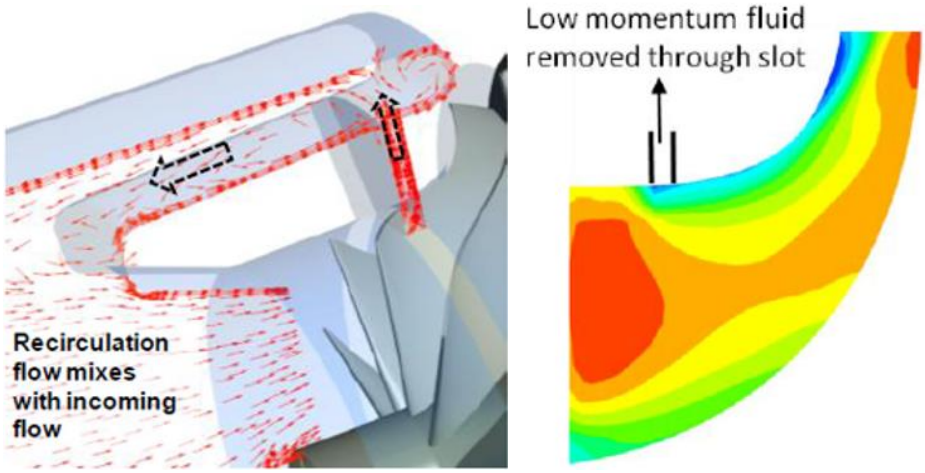

Figure 2.11: Effect of ported shroud on flow near surge [14]

Impeller Blade Design Optimization

In a study to improve impeller exit flow uniformity, Hiradate *et al.* [37] explored impeller blade lean for fully shrouded impellers (no tip clearance) with a vaneless diffuser. They provided design guidelines and validated numerically and experimentally a new impeller with curvilinear blade elements in which the blade 2D sections are stacked along a curvilinear spanwise stacking line rather than a straight stacking line. Their results showed that leaning the blade in the direction opposite to its rotation, in other words applying a negative tangential lean, along the entire chord reduces the blockage associated with the suction surface boundary layer and tip clearance flow. On the other hand, negative tangential lean promotes accumulation of low-momentum fluid at the suction surface-hub corner. Moreover, it also accentuate flow deceleration near the upstream part of suction surface resulting in a reduced stall margin. However, these drawbacks can be eliminated with a curvilinear blade (concave on the suction side, see Figure 2.12 (b)) and reduction in inducer flow turning. Indeed, Figure 2.12 (b) shows the resulting negative tangential lean blade design with the concave suction surface and associated reduced accumulation of low-momentum fluid (dark blue regions in Figure 2.12 (a)) and improved uniformity of the impeller exit flow. The stage stall margin was extended by 5% and the efficiency was increased by 2.4% over the baseline impeller design.

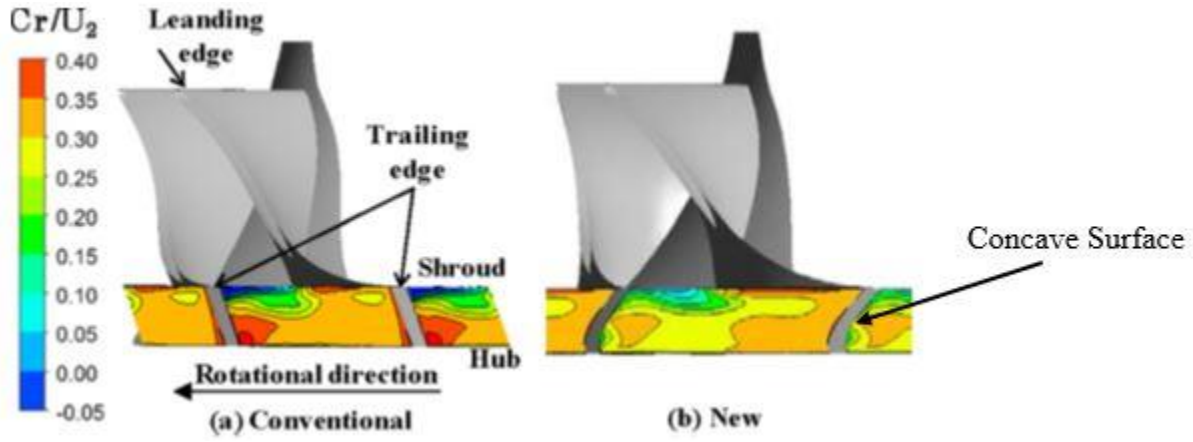

Figure 2.12: Radial velocity distribution at impeller outlet (at design point) before and after impeller blade lean [37]

Shibata *et al.* [38] investigated numerically and experimentally the effect of backsweep angle, diffusion factor (relative velocity reduction) and blade loading for five different unshrouded impellers at high specific speed range with vaneless, vaned and low-solidity vaned diffusers. They increased the backsweep angle to reduce losses in the diffuser and simultaneously increased the inlet-to-exit relative velocity diffusion ratio by increasing impeller exit blade height in order to avoid pressure ratio reduction. In their study, the impeller stall margin was shown correlated with the inlet-to-exit relative velocity diffusion ratio and was increased by lowering the impeller front loading. It was concluded that proper blade loading distribution is essential for a wide operating range as well as high efficiency.

It is desirable to design compressors with reduced size and weight while maintaining high stall margin and adiabatic efficiency. However, higher stage pressure ratio requires increased loading and greater inlet Mach numbers leading to transonic inlet flow conditions, both of which tend to decrease operating range and efficiency significantly. Hah and Krain [32] performed numerical and experimental analyses on an impeller with splitter blades at different operating conditions. They pointed out that high inlet flow incidence and large flow separation near the hub cause a large volume of low-momentum fluid to travel toward the inducer tip, which increases the loss through increased shock/boundary layer interaction. At higher flow rates, a second shock at the splitter leading edge exacerbates the situation. With the help of numerical simulations, they assessed the effect of modifying the blade camber near the main blade leading edge and reduced the main blade thickness by 50%. These mitigated the flow separation and improved the mass flow split between the two impeller channels, resulting in better flow distribution at the impeller exit. The combined effect was a 5% improvement in stall margin as inferred from speedlines, 8% in choke margin, 5% in impeller efficiency and an increased pressure ratio from 6.1:1 to 7.1:1.

Ganesh et al. [39] explored numerically the impact of impeller inducer forward and backward lean on stall margin and performance of a 4:1 pressure ratio centrifugal compressor with a vaneless radial diffuser. Forward lean is defined as a tangential lean opposite to the impeller rotation and backward lean is in the direction of impeller rotation in this work, as shown in Figure 2.13. It was found that forward lean tends to decrease the efficiency. However, the maximum stall margin improvement of approximately 6% was achieved for the forward lean of 20°. The mechanism with which the inducer lean improves the performance parameters is through changing the effective

passage flow area and redistributing the flow within the impeller blade passage. This yields shock-free regions inside the passage, smaller low-momentum flow regions and improved flow uniformity at the impeller exit plane, all beneficial for improved performance and stall margin.

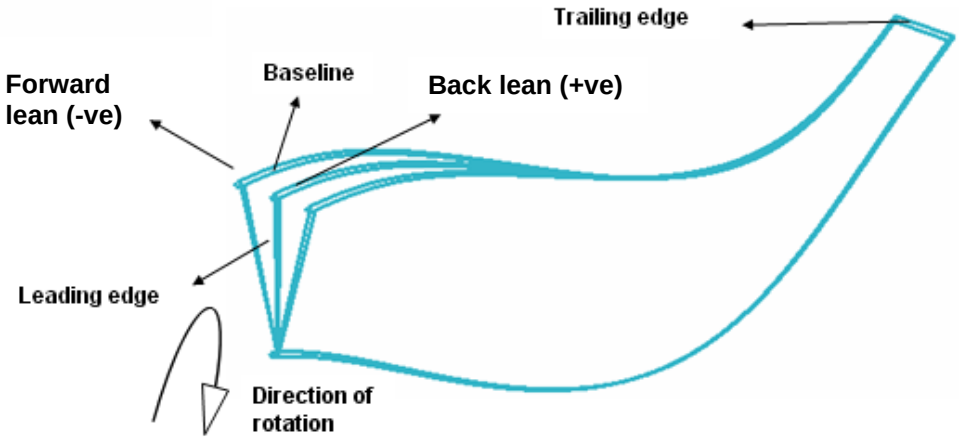

Figure 2.13: Impeller blades with zero, forward and backward lean at impeller leading edge, modified from [39]

2.2.2 Other Types of Compressors

While there are different active and passive flow control strategies to improve performance and operating envelope of axial and mixed flow compressors, this section mainly focus on passive flow controls over the stationary element. These techniques have the potential of being applied to centrifugal compressors, mainly to the empty space available on the impeller casing radial bend.

In an experimental and numerical investigation, Müller *et al.* [40] examined the effect of circumferential grooves over the rotor on the operating range of a single-stage transonic axial compressor. Four different shallow and deep groove configurations with variable coverage of the rotor projected axial chord were tested. Figure 2.14 shows one configuration with six grooves covering 82.4% of the rotor axial chord. Results indicated that all applied grooved casings reduced stalling mass flow at design speed and at three off-design speeds significantly, while deep grooves were more effective in increasing operating range with a stall margin extension of 9.9% as inferred from speedlines and total pressure ratio. Independently from the groove depth, a higher coverage of the rotor projected axial chord can better delay stall inception. It was also found that shallow

grooves can increase stage peak efficiency more than one percent at design speed while deep grooves roughly maintain efficiency levels compared to the smooth casing. Comparison of 3D RANS CFD simulations of the smooth casing configuration against that with six deep grooves also revealed that at the nominal stalling mass flow rate, the grooves reduce the tip blockage area inside the blade passage tip and deflects the tip leakage flow in the streamwise direction.

Figure 2.14: Axial Rotor with 6 Circumferential Grooves [40]

Guinet *et al.* [41] performed a time-accurate numerical investigation on the recirculating tip blowing casing treatment shown in Figure 2.15 for a rotor of a one-and-a-half stage (IGV-rotor-stator) axial research compressor. In order to provide the maximum pressure difference and hence the maximum injected momentum, the inlet of the recirculating duct is placed at 90% tip chord downstream of rotor leading edge and its outlet is 15% tip chord upstream of rotor leading edge. CFD simulations with and without tip blowing casing treatment were carried out at three different rotor tip gaps of 0.5%, 1% and 1.5% of span with an average relative recirculated mass flow of around 0.27%-0.38% of the main mass flow.

Results showed that the tip blowing casing treatment reduces the tip gap leakage flow and re-energizes the endwall low-momentum flow, resulting in a reduction in tip blockage and an increase in the stall margin for 1% and 1.5% tip gaps by 4.75% and 3.4%, respectively as inferred from speedlines. The efficiency was unchanged at design point but was increased near stall for 1.5% tip

gap through an improvement in tip region flow uniformity. The stall delay mechanism for 1% and 1.5% tip gap was related to the delay in tip vortex breakdown. However, the tip blowing casing treatment is ineffective for the 0.5% tip gap configuration where stall was caused by blade boundary layer separation.

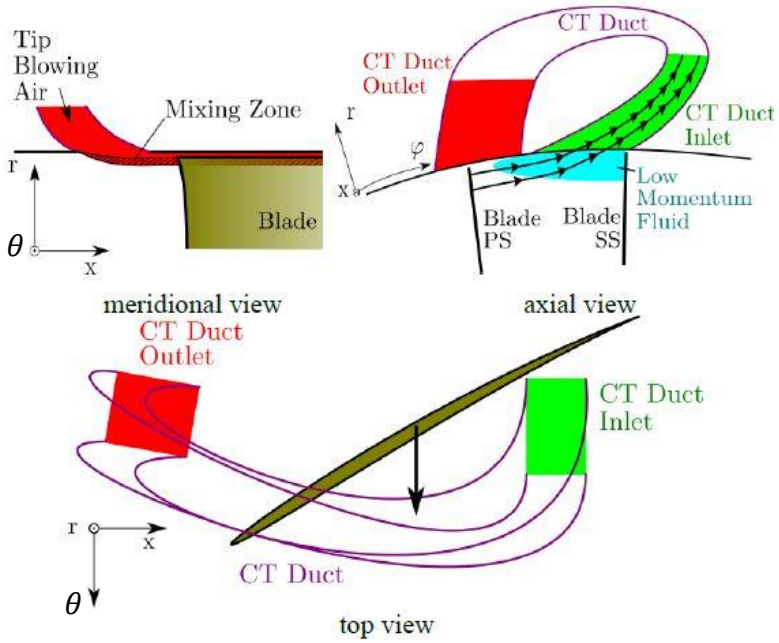

Figure 2.15: Schematic illustration of tip blowing casing treatment, modified from [41]

Wilke *et al.* [42] performed a time-accurate three-dimensional numerical study of the impact of the axial slots over the first stage rotor of high-pressure transonic axial compressor. The two configurations shown in Figure 2.16 were considered. Configuration 1 (Figure 2.16 (a)) in which slots cover the blade tip from leading edge to trailing edge. Configuration 2 (Figure 2.16 (b)) in which slots are moved upstream and only 25% of the axial chord is under the slots. Both configurations extend stall margin by approximately 20% by affecting the tip leakage flow. However, configuration 1 results in a 4% penalty in efficiency while configuration 2 reduces the efficiency only by 0.2%. Hence, manipulating the tip leakage flow only in the upstream portion or close to the leading edge provides the same benefit in stall margin extension with much less efficiency penalty.

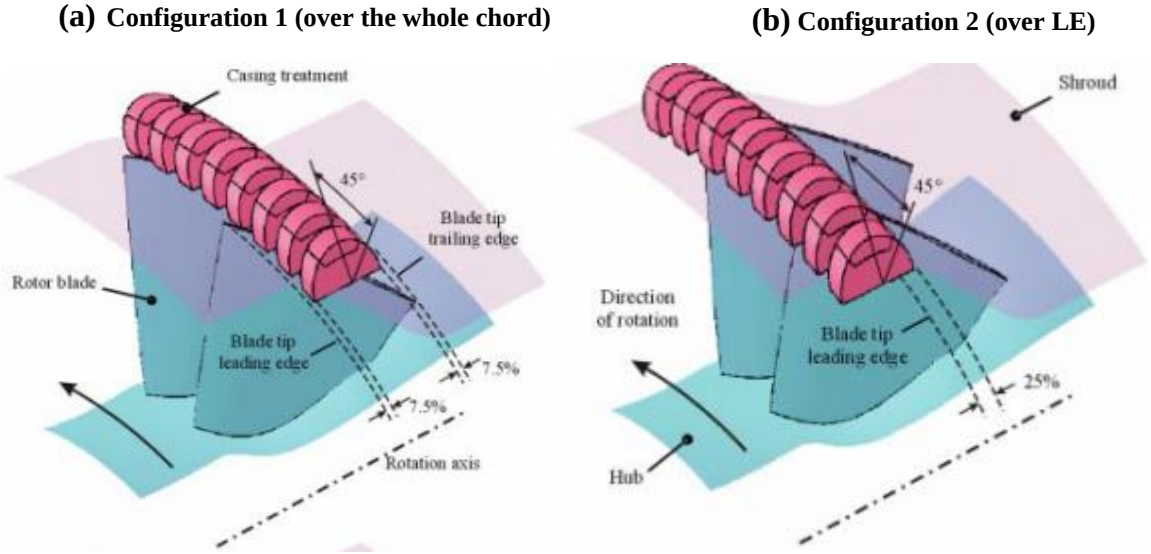

Figure 2.16: Axial slot casing treatment for an axial compressor rotor [42]

While casing treatments have mostly been studied in axial compressors, there is one study for non-axial compressors. Djeghri *et al.* [34] looked into slots casing treatment for a mixed flow compressor rotor at subsonic speed, as shown in Figure 2.17. A mixed flow compressor is somewhat similar to an axial compressor but with a large change in mean radius across the rotor, with the flow exiting the rotor axially (rather than radially). Using CFD simulations, the authors carried out the most extensive parametric study of slot casing treatments to-date on any compressor to find preliminary design rules to maximize stall delay without loss in peak efficiency. They considered nine different design parameters for slots casing treatment over a mixed-flow rotor, namely slot axial position; open area ratio; slot skew angle; number of slots per blade passage; slot stagger angle; slot radial shape; slot lateral shape; slot axial length; and slot depth. The authors claimed that slot axial position, open area ratio, slot skew angle and slot axial length are the most important parameters in increasing stall margin and minimize the negative impact on peak efficiency. Their best configuration is characterized by 3 semi-circular, axial slots per blade passage with 60 degree skew angle and 60% open area ratio with half the slot axial length located upstream of the blade leading edge. This configuration improved the operating range up to 25% as inferred from speedline and provided even a small gain in peak-efficiency over the baseline rotor without casing treatment.

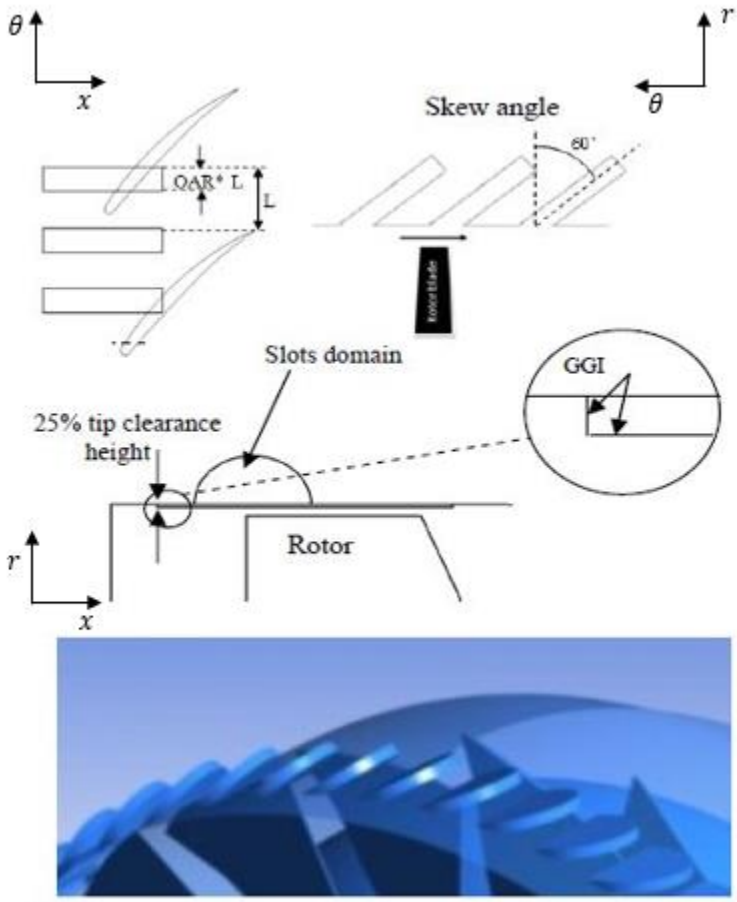

Figure 2.17: Axial skewed slot casing treatment for a mixed-flow rotor, modified from [34]

2.3 Summary

The following conclusions can be drawn from the literature review.

First, most stall delay studies have focused on reducing the blockage in the impeller tip region and improving the flow uniformity within the impeller. Knowing the importance of the interaction between the impeller and diffuser, this blockage reduction will also be important for the uniformity of the flow within diffuser, diffuser loss and by extension centrifugal stage performance. This should be the focus of flow control concepts to improve stage stall margin and performance.

Second, while there are many studies to improve the operating range and performance of centrifugal compressors used in turbochargers, there are few studies for centrifugal compressors used in aero-engines, especially for those with the more complex fishtail pipe diffusers. Moreover,

the retroactive flow control studies on centrifugal compressors with vaneless diffusers seem to produce higher stall margin improvement (*SMI*).

Third, the studies which apply passive flow control like casing treatments (slots, pipes and grooves) focus mainly on the impeller leading edge and inducer region. No such studies have been dedicated to other regions such as the impeller radial bend. However, some of the successful techniques applied to axial, mixed-flow and centrifugal compressors using other types of diffusers such as grooves, slots and recirculation ducts can be tried at the radial bend for centrifugal compressors with fishtail diffusers.

CHAPTER 3 METHODOLOGY

3.1 General Methodology

A computational approach based on RANS CFD simulations is chosen for the current study. This approach allows for a relatively low-cost and rapid evaluation of different flow control techniques and it provides access to the entire flow field for detailed analysis.

This project starts with the design of two centrifugal compressor stages with fishtail pipe diffusers, one high-speed (transonic) and another low-speed (subsonic), both based on existing or past compressor geometries. Although validation is required, one compressor stage is intended to exhibit diffuser stall while the other should exhibit impeller stall, in order to assess passive flow control at the radial bend for both. Thereafter, different passive flow control techniques are proposed for the radial bend of the centrifugal compressor stages based on the literature review of flow control in axial compressors and in centrifugal compressors at the impeller leading edge.

The assessment of flow control at the radial bend for each of the two compressor stages is carried out in three phases. First, the stalling component (impeller or fishtail diffuser) is identified through simulating the impeller alone and the compressor stage up to their stall points (convergence limits). If the stage stalls at a higher mass flow than the impeller, then the diffuser is responsible for stall. Otherwise, the impeller is the stalling component. The flow field within the stalling component is then examined to find the stall mechanism. It consists of detecting the growth of low-momentum flow structures, such as boundary layer separation, near and past the convergence limit during the stall transient. In Phase 2, the simulations of the stage with the different passive flow control devices at the radial bend are performed from the nominal design mass flow up until their convergence limits passing through the baseline (no flow control or smooth casing) stalling mass flow. An integral comparison of the stall margin extension and effect of stage performance is first presented for each flow control technique versus the baseline case. This is followed by a comparison of the flow field associated with selected flow control techniques against that of the baseline case to assess their effect on the flow structure responsible for stall and to elucidate the

mechanism by which this flow structure is suppressed to delay stall. Finally, in Phase 3, the impact of the studied flow control techniques on loss at the design mass flow is investigated on a preliminary basis to identify the sources of the efficiency penalty.

It must be noted that the identification of the most effective flow control techniques at the radial bend for stall margin extension is not really the mandate of the current research. The reason is that a fair comparison between different flow control techniques would require the optimization of each of them, which is beyond the scope of this first study of flow control at the radial bend. Instead, the simulations of different flow control techniques aim to identify the flow mechanism(s) by which stall can be delayed by passive flow control at the radial bend such that flow control techniques can later be refined for maximum stall margin extension and minimum performance penalty.

3.2 Compressor Geometries

3.2.1 High-Speed Compressor

The first compressor geometry chosen for study is a high-speed centrifugal compressor stage with fishtail pipe diffusers. This stage geometry is based on a rear compressor stage of a production aero-engine. However, contrary to the original design, the new stage has the same number of impeller blades and diffuser pipes. This allows for unsteady simulations of the stage to be carried out using a single passage domain with periodic lateral boundary conditions. The original design with mismatched impeller blade and diffuser pipe numbers would have required a full-wheel unsteady simulation, which would have been too expensive in both resource and time to be feasible. The new impeller was designed using ANSYS BladeGen. As for the diffuser design, Appendix A provides an overview of the published literature on important parameters for fishtail diffuser design with Han *et al.* [12] being the most complete published source. The current diffuser mimics the original design which was verified to be consistent with the guidelines by Han *et al.* [12], in terms of the best values for the main geometric parameters: cross-sectional area change, cone length and centerline shape. Figure 3.1 shows the new high-speed compressor stage while Table 3.1 summarizes the design parameters of this stage. Based on practice, this type of high-speed

centrifugal compressor geometry usually stalls due to the diffuser, although this has to be verified for the current geometry.

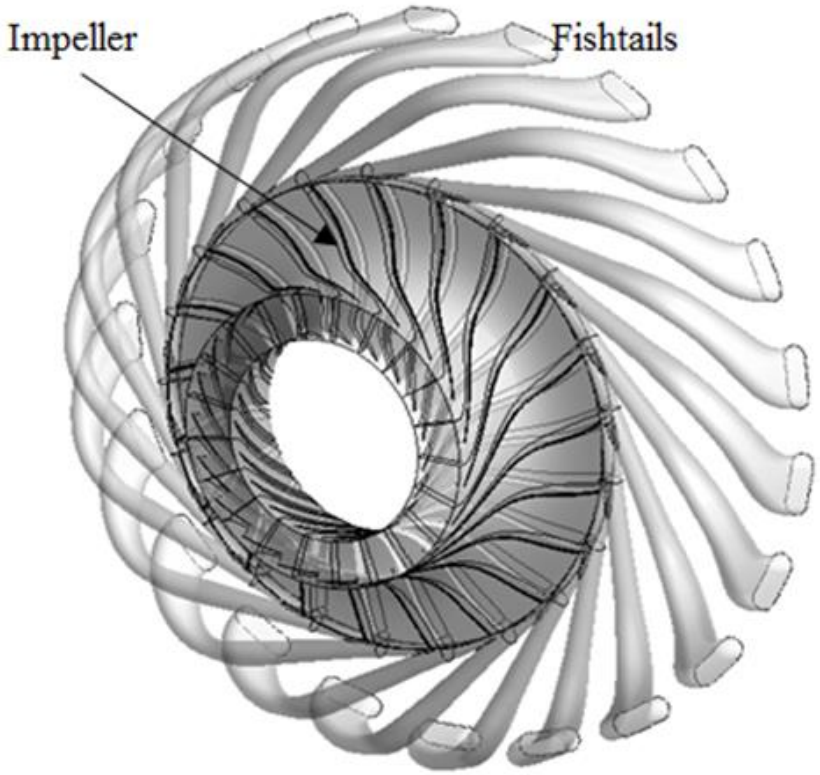

Figure 3.1: High-speed centrifugal compressor design with fishtail pipe diffusers

3.2.2 Low-Speed Compressor

This low-speed design uses the impeller geometry from a previous low-speed two-stage axial centrifugal compressor test rig shown in Figure 3.2 that was designed and built in an undergraduate capstone project in 2012-2013 at École Polytechnique de Montréal [43]. The original centrifugal stage featured a vaneless diffuser. This rig was later used for research into stall delay with plasma actuation [21], which pointed to the impeller as the source of stall.

Table 3.1: Design parameters of the high-speed centrifugal compressor stage

Parameter	Value
Design corrected speed (rpm)	40942
Design corrected mass flow rate (kg/s)	1.461
Design total-to-total pressure ratio	5.22
Design impeller efficiency (%)	91.42
Design stage efficiency (%)	84.01
Fishtail total pressure loss coefficient	0.1674
Impeller inlet circumferential tip speed (m/s)	323.32
Impeller tip radius inlet/exit (mm)	74.60/118.36
Impeller inlet hub radius/exit blade height (mm)	51.42/8.26
Number of impeller blades/fishtail pipes	21/21
Impeller tip clearance (mm)	0.2537
Fishtail diffuser inlet radius (mm)	118.74
Fishtail diffuser exit shroud radius (mm)	189.75
Fishtail exit to throat area ratio	4.47
Fishtail inlet incidence angle for maximum efficiency (degree)	-3.47

A fishtail pipe diffuser was designed for this impeller, again with the constraint that the number of diffuser pipes equals the number of impeller blades to allow for affordable single blade passage unsteady simulations. While the number of diffuser pipes/passages is not the same as the number of impeller passages in practice, the results obtained using this assumption should still be valid for real compressors since the analysis is based on a time-averaged flow field. The fishtail pipe diffuser for this low-speed design follows the guidelines of Han *et al.* [12]. This low-speed compressor

design is shown in Figure 3.3 and Table 3.2 summarizes its design parameters. While yet to be verified, it is expected that this stage will exhibit impeller stall.

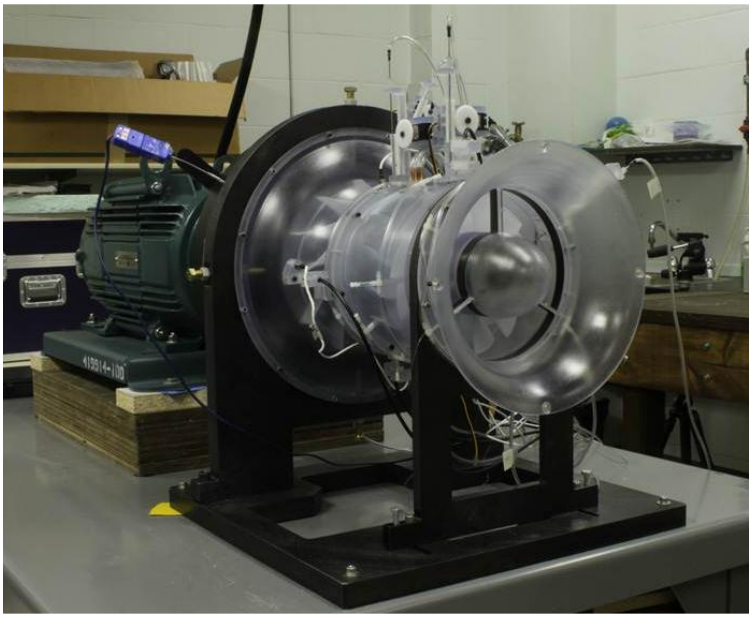

Figure 3.2: Two-stage axial-centrifugal test rig designed and built in 2012-2013 [43]

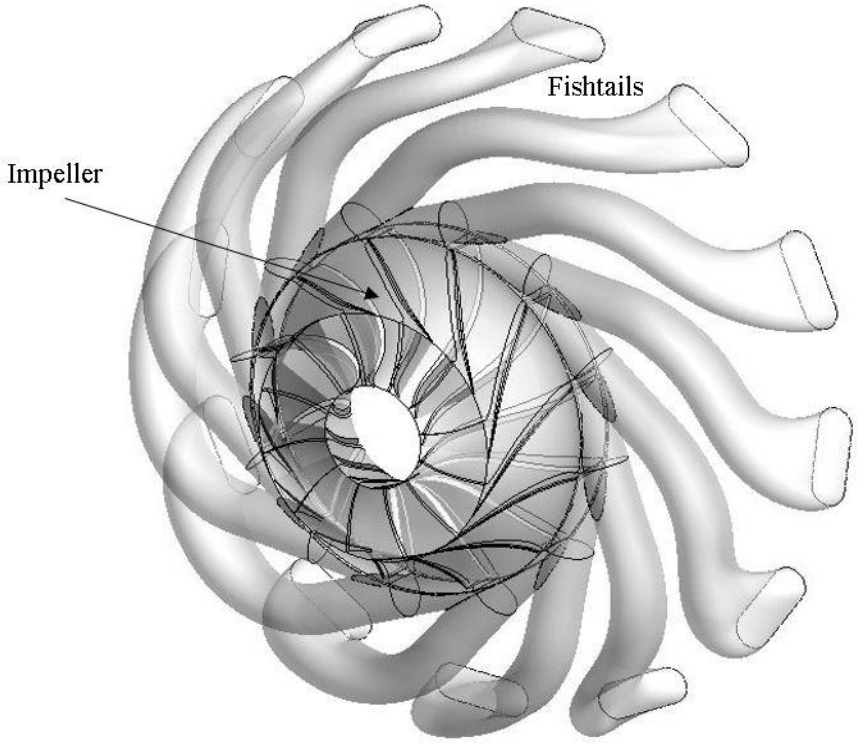

Figure 3.3: Low-speed centrifugal compressor design with fishtail pipe diffusers

Table 3.2: Design parameters of the low-speed centrifugal compressor stage

Parameter	Value
Design corrected speed (rpm)	7112
Design corrected mass flow rate (kg/s)	0.492
Design total-to-total pressure ratio	1.048
Design impeller efficiency (%)	95.09
Design stage efficiency (%)	87.45
Fishtail total pressure loss coefficient	0.1560
Impeller inlet circumferential tip speed (m/s)	57.175
Impeller tip radius inlet/exit (mm)	76.20/107.95
Impeller inlet hub radius/exit blade height (mm)	31.75/26.20
Number of impeller blades/fishtail pipes	12/12
Impeller tip clearance (mm)	0.381
Fishtail diffuser inlet radius (mm)	109.681
Fishtail diffuser exit shroud radius (mm)	219.866
Fishtail exit to throat area ratio	1.7786
Fishtail inlet incidence angle for maximum efficiency (degree)	-6

3.3 Flow Control Techniques

The general strategy hypothesized to improve the stall margin of centrifugal compressors with fishtail pipe diffuser consists of increasing the streamwise velocity of the low-momentum flow near the shroud downstream of the radial bend that grows in size toward the impeller exit (Eckardt [17]). The goal is to improve flow uniformity in the exducer and diffuser inlet (impeller exit) so as

to delay any flow separation that may occur and could lead to stall, respectively, on the exducer blade and in the diffuser.

To achieve this goal, potential flow control strategies that can increase flow uniformity are identified from the literature review. Beside this stated purpose, two other criteria are used for the selection. The first is that the flow control technique must be passive, meaning that it does not require energy input. The use of active flow control usually adds complexity in the form of actuator integration, robustness and maintenance, which may be impractical from a cost stand point. The second criterion is that priority be given to techniques placed in stationary components, in this case the impeller shroud and diffuser. Chapter 2 has shown that impeller redesign, such as tangential blade lean and curved blade elements, can be aerodynamically effective in improving exit flow uniformity. However, with the impeller subjected to high structural and thermal stresses, such impeller designs may not be practical. On the other hand, flow control strategies placed on stationary components can be implemented more easily either on new compressor designs or retroactively on existing compressors. The candidate passive flow control techniques satisfying these criteria fall under two categories, namely casing treatments and flow recirculation. Simulations of the two baseline compressors showed that the local flow recirculation zone (separation bubble) on the impeller shroud starts approximately at 30% shroud curve length from the impeller leading edge and is centred at about 40% shroud curve length. This will determine the location of the flow control devices.

3.3.1 Casing Treatments

Casing treatments in the form of circumferential grooves and slots placed over axial compressor rotors have been used for extending the stall margin. They work by transferring flow from the blade pressure side to the suction side over the blade tip clearance region. This transfer enhances flow mixing between the tip clearance flow and core flow and thus increases the streamwise momentum of the tip blockage region caused by the tip clearance flow. Thus, the proposed strategy is to place these two types of casing treatments over the impeller in the region of the radial bend where the tip blockage starts to grow towards the impeller exit. Casing treatments can reduce the size of this velocity deficit region that was first identified by Eckardt [17] through enhancing flow mixing with

the core flow. The successful circumferential grooves geometry from reference [40] and the slots configuration like the ones reported in [13, 34, 42] will be applied to the centrifugal compressor design. The proposed casing treatments are illustrated for the high-speed compressor in Figure 3.4. For both studied compressors, the groove and slots are centred at 40% shroud curve length (centre of separation bubble) with the meridional length chosen to cover the extent of the separation bubble at least. While the implementation of slots in the shroud of an impeller near the bend may pose difficulty for traditional machining, it would be relatively simple using 3D-printing technology.

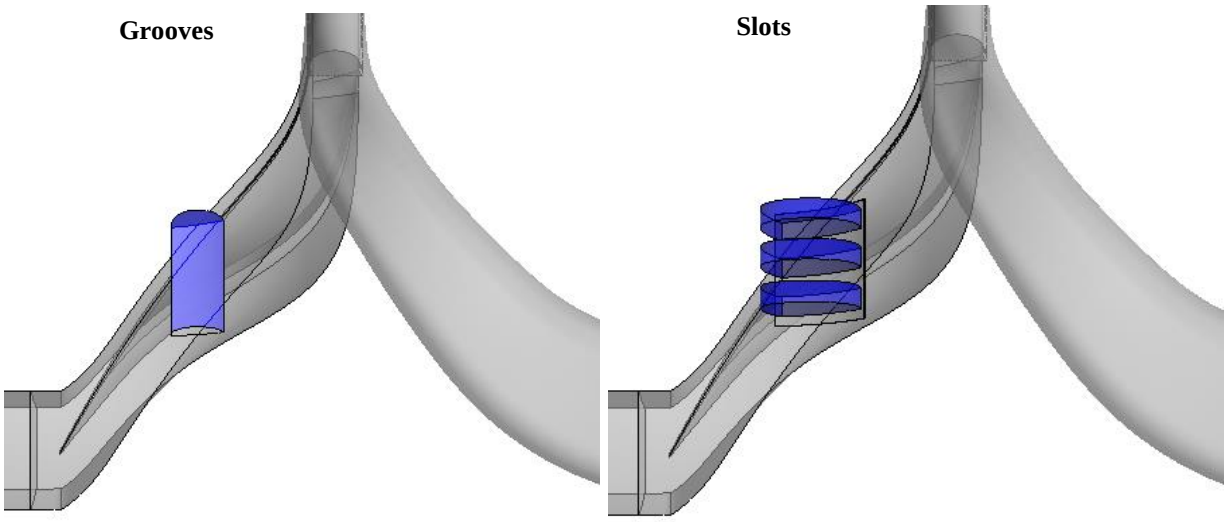

Figure 3.4: Proposed casing treatments applied at impeller radial bend

3.3.2 Flow Recirculation

Although casing treatments recirculate flow locally, flow recirculation pipes or channels, somewhat similar to those described in[15, 16], allow for the suction port to be located much further downstream in the compressor to increase the pressure difference between the suction and injection ports and thus increase the momentum of the injected air. The increased injection momentum associated with flow recirculation pipes reduces the amount of flow recirculation needed to achieve the same effect. Moreover, flow recirculation provides more control over the direction of flow injection through ability to set the direction of the injection hole such that the flow injection lines up better with the local streamwise direction in the relative (rotating) frame to maximize the

streamwise momentum addition. Last but not least, flow recirculation can take full advantage of 3D printing technology to easily integrate the recirculation pipes/channels in the design and manufacturing of the compressor components. However, recirculating flow on which work has been done by the impeller as well as the viscous loss in the recirculation pipes/channels can translate to higher efficiency penalty. Figure 3.5 illustrates the two proposed flow recirculation configurations for the centrifugal compressors under study. The first configuration recirculates air extracted within the impeller from its trailing edge, while the second extracts air from near the diffuser exit on its suction side, where the low-momentum air would likely be located and whose removal should be beneficial for both stall margin and performance. In all cases, the injection port is located at 30% shroud curve length from the impeller leading edge, which marks the onset of the flow recirculation zone on the impeller shroud of both centrifugal compressors studied.

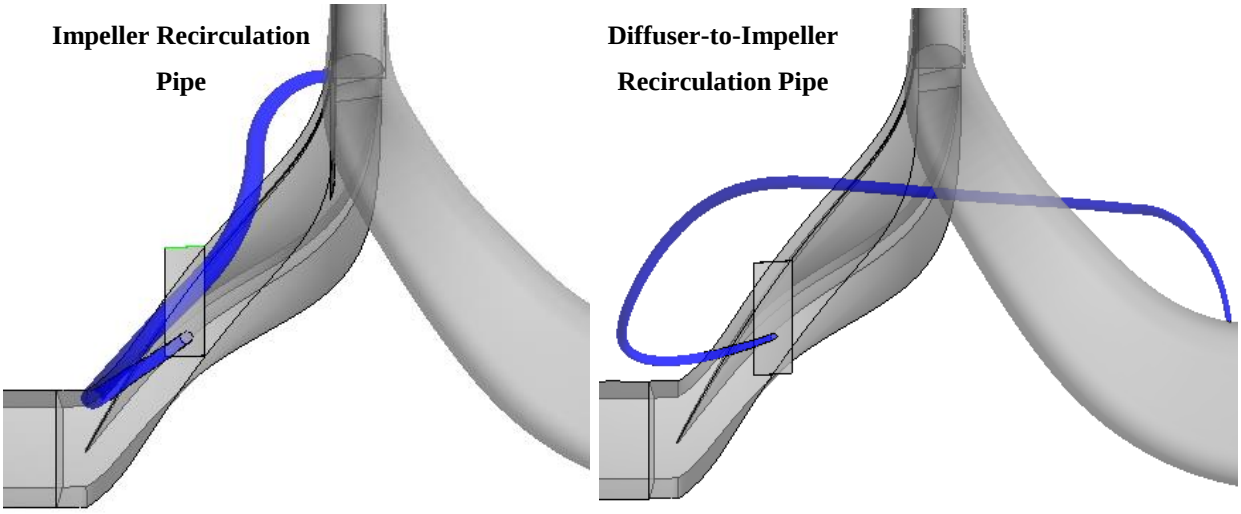

Figure 3.5: Proposed flow recirculation configuration with injection at impeller radial bend

3.4 Numerical Setup

Computational Fluid Dynamics (CFD) simulations are used to assess and compare the candidate flow control strategies. This numerical approach provides a low-cost and efficient way to quantify the effect of each strategy both on an integral level (compressor performance and stall margin) as well as on a detailed level in terms of modification to the flow field.

3.4.1 Numerical Tools

Numerical simulations of the centrifugal compressors without and with the different flow control strategies are carried out using ANSYS CFX Versions 14.5 and 18.2, mainly in unsteady mode to capture the blade passing effects between the impeller and diffuser, at least on a time-averaged basis. ANSYS CFX is a sophisticated commercial cell-centered, pressure-based, implicit, finite-volume Reynolds-Averaged Navier-Stokes (RANS) CFD code able to handle both structured and unstructured grids, and widely used for turbomachinery. While the available CFX version changed over the course of the project, simulations were carried out on a particular configuration to verify that the two versions gave the same result.

The mesh for the impeller domain and its upstream intake domain (representative of a Bellmouth intake) are generated using ANSYS TURBOGRID Versions 14.5 and 18.2, a meshing software designed for standard turbomachinery configurations which creates hexahedral elements. The meshes for all other domains, including the fishtail diffusers and sub-domains associated with flow control techniques, are created with ANSYS ICEM CFD Versions 14.5 and 18.2, a powerful meshing tool capable of creating structured and unstructured grids for arbitrary geometries.

Regarding turbulence modeling, the two-equation Reynolds-Averaged Navier-Stokes (RANS) Shear Stress Transport (SST) turbulence model is chosen for the simulations. This model combines the $k-\varepsilon$ and $k-\omega$ turbulence models, and is capable of predicting the onset and amount of boundary layer separation in an adverse pressure gradient, such as in the case of flows over curved surfaces [44]. ANSYS recommends the SST turbulence model whenever the accuracy of results is more important than the robustness of simulations [44]. Since the simulations in this research are mainly within the stable operating range up to the stall point, flow instabilities are not expected such that robustness is not an important consideration and the SST model can be used. The $\gamma-\theta$ transitional turbulence is selected for the SST turbulence model to model the laminar-turbulent transition. Bourgeois *et al.* [11] performed a numerical evaluation of four different turbulence models namely, $k-\varepsilon$, SST, SST-reattachment modification (RM) and Speziale- Sarkar- Gatski Reynolds stress model (RSM-SSG) for a centrifugal stages with fishtail diffusers. Simulations were carried using steady-state mixing plane in ANSYS CFX-11.0. Their simulation results revealed

that SST and RSM-SSG models perform very well in terms of predicting pressure and temperature ratio, stage efficiency and topological flow characteristics such as blockage and flow separation when compared with experimental results. However, the computational time for the RSM-SSG model was about five times that of the other models. Consequently, the SST model was chosen for the current research as it is the most advantageous model for rapid assessment and design optimization of flow control strategies.

Lastly, an ideal gas model is used for air for the low-speed compressor while a real gas model is used for the high-speed case. The real gas model is basically an ideal gas model that also takes into account the variation of viscosity and heat capacity with temperature which is not negligible in a transonic flow field.

3.4.2 Numerical setup for baseline compressors

Figures 3.6 and 3.7 show the computational domain along with the boundary conditions and interfaces for the baseline high-speed and low-speed centrifugal compressor stages, respectively. Both have a similar layout. An *intake* subdomain upstream of the impeller models a Bellmouth intake. Similarly, an *end duct* subdomain downstream of the fishtail diffuser models an exit plenum. All subdomains have the same circumferential extent, covering one impeller blade pitch as well as one diffuser pipe since the number of diffusers pipes equals that of the impeller blades. The subdomains are stationary, except for the impeller subdomain which is solved in the rotating frame of reference.

The most important interface is the *Transient Rotor-Stator* (sliding plane) interface between the impeller and diffuser subdomains. In the unsteady simulations performed in this research, this interface simulates the relative motion between the components on each side of the General Grid Interface (GGI) connection by updating their position at each time-step. In other words, it allows for the transfer of circumferential flow variation between these two components, which is required to capture the effect of flow unsteadiness generated by the impeller-diffuser interaction. Figure 3.8 shows how this type of interface successfully models the transfer of flow field from the impeller side to the fishtail diffuser side, illustrated here for the high-speed compressor, through the continuity of the entropy contours across the impeller-diffuser interface. As for the other interfaces,

a *Frozen Rotor* interface is applied between the stationary intake subdomain and the rotating impeller subdomain. This interface considers a fixed relative position between the components on each side of the interface and allows for flow circumferential variation to pass from one subdomain to another. It is essentially a low-cost approximation to a sliding plane interface. Finally, a simple GGI interface (with no Frame Change/Mixing Model) is implemented between the diffuser and virtual exit duct subdomains. This interface simply transfers all spatial distribution of flow properties from one domain to the other through interpolation.

In terms of boundary conditions, the inlet boundary conditions to the computational domain consists of uniform total pressure and total temperature taken at ambient conditions (about 1 atm and 21 deg C), zero swirl angle (axial flow) and a specified (medium) turbulence intensity of 5%, as suggested in [44]. At the outlet, a throttle boundary condition is used to find the stall point, while a mass flow boundary condition is used to capture the operating point at design mass flow rate. A throttle boundary condition can capture the stall point when the total-to-static pressure rise speedline has zero or positive slope which cannot be captured by a standard back static pressure boundary condition. Furthermore, it comes closest to capturing the actual physics of stall transient (during which the pressure rise follows the throttle line as shown in Figure 3.9) which is not captured by a mass flow boundary condition. The throttle boundary condition used here was set up by Dumas *et al.* [45]. It models the behaviour of a plenum and valve placed downstream of the compressor in a rig to set a dynamic static pressure at the exit of the compressor CFD domain (see inset of Figure 3.9). This pressure varies as a function of mass flow, plenum volume (fixed) and valve pressure drop characteristics set through a throttle constant (*Kt*) that is increased gradually to reduce the mass flow. A lateral periodic boundary condition is applied to the lateral boundaries of the inlet duct, impeller and diffuser (pseudo-vaneless space part) subdomains. All the solid surfaces are modeled as a no-slip wall considering the shear effects with the automatic wall function option able to switch between a no-slip wall and wall function based on the local y^+ value [44]. However, if a wall does not physically exist, as in the case for the virtual end duct subdomain, the wall will be modeled as free-slip/inviscid wall so that the shear effects are not considered. The stationary impeller shroud is defined as counter-rotating since the impeller domain is resolved in the rotating frame.

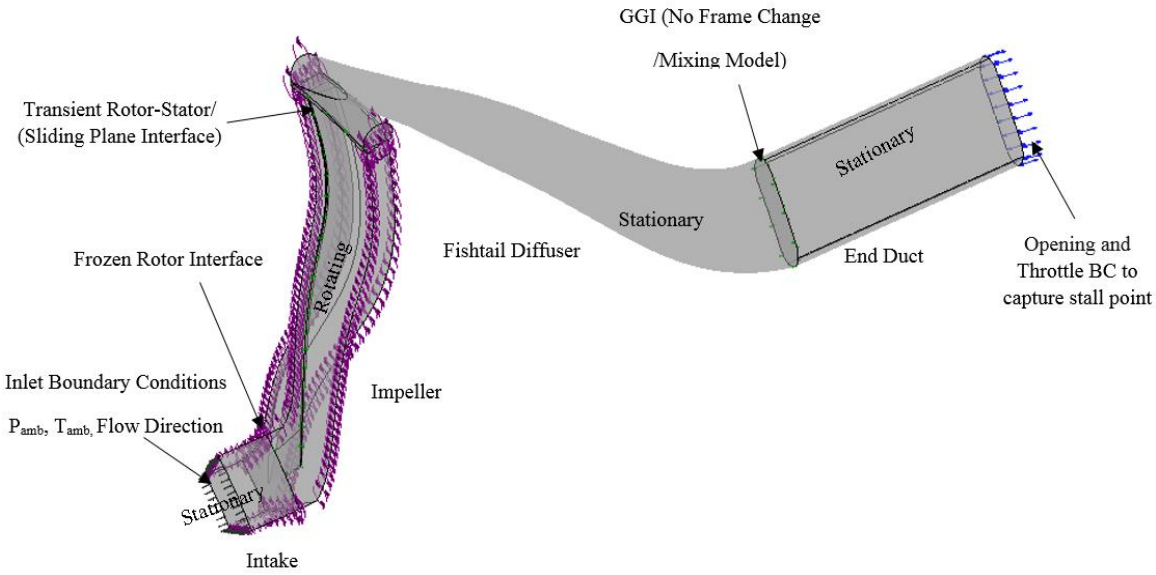

Figure 3.6: Computational domain for baseline high-speed centrifugal compressor stage

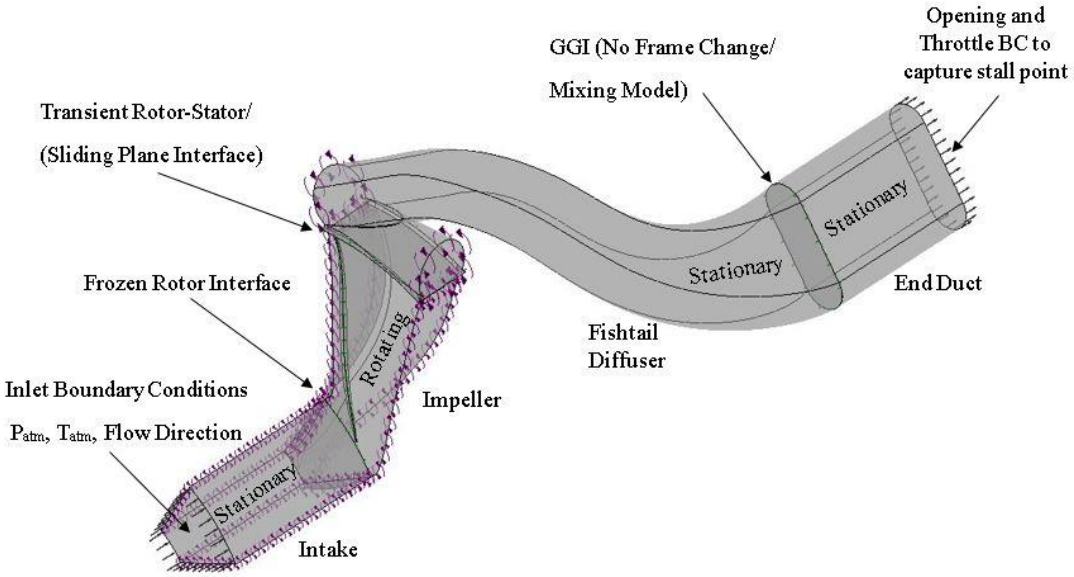

Figure 3.7: Computational domain for baseline low-speed centrifugal compressor stage

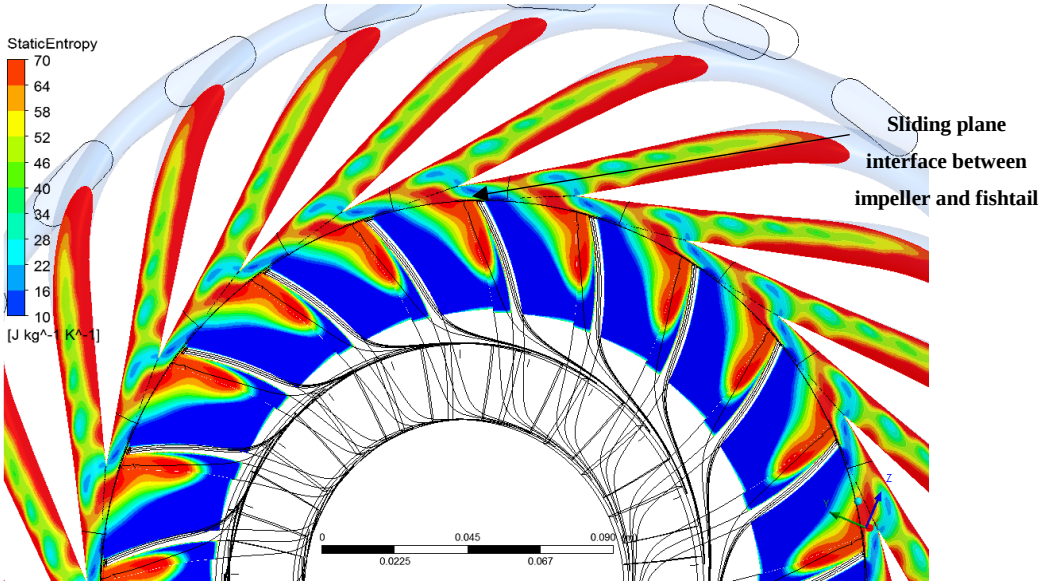

Figure 3.8: Static entropy contours across impeller and diffuser subdomains via sliding plane interface for high-speed centrifugal compressor stage

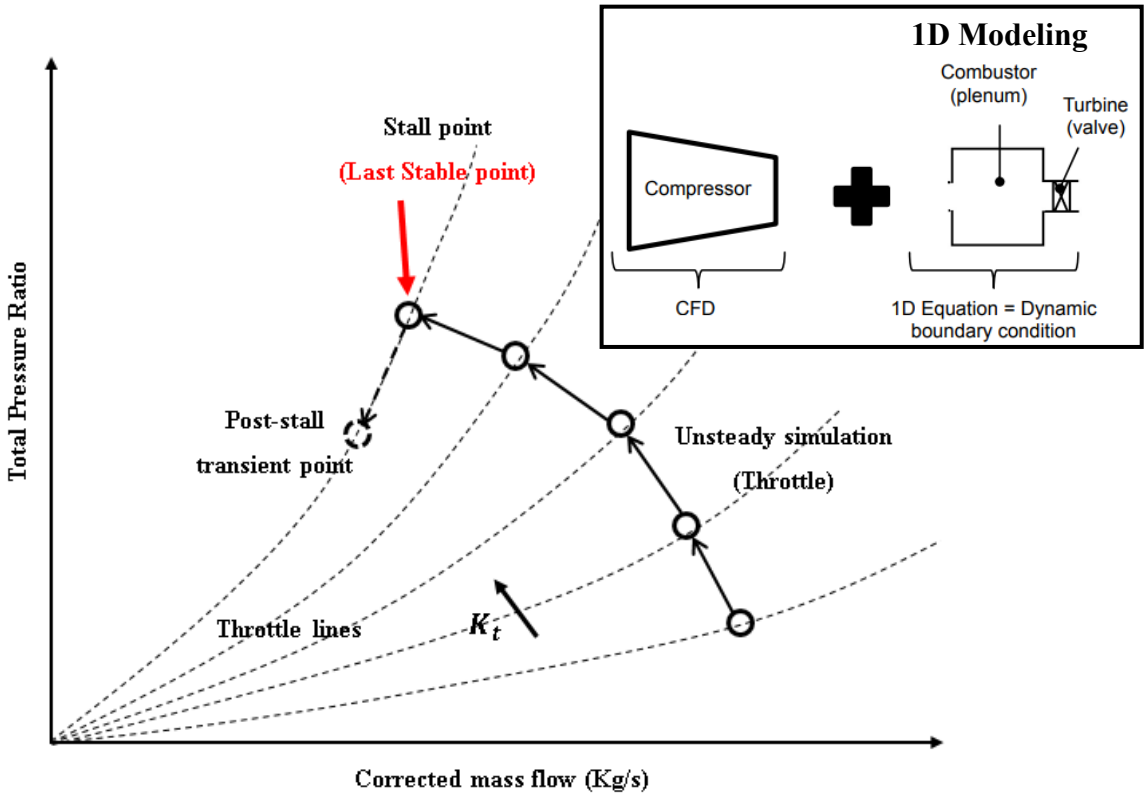

Figure 3.9: Throttle boundary condition to capture stall and post-stall points through increase in throttle constant (*Kt*), Inset from [45]

Figures 3.10 and 3.11 show the mesh for the baseline high-speed and low-speed centrifugal compressor stages, respectively. In both configurations, ANSYS TURBOGRID was used to generate a structured mesh for the intake and impeller subdomains, while the fishtail diffuser and end duct subdomains use an unstructured mesh with tetrahedral elements generated with ICEM CFD. A mesh study, described in Appendix B, was performed to obtain the final mesh as shown.

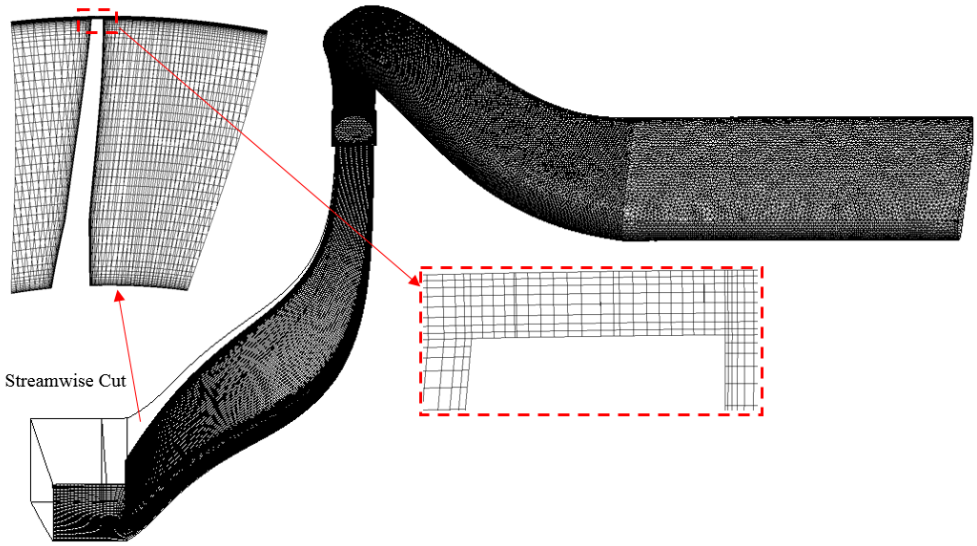

Figure 3.10: Mesh for baseline high-speed centrifugal compressor stage

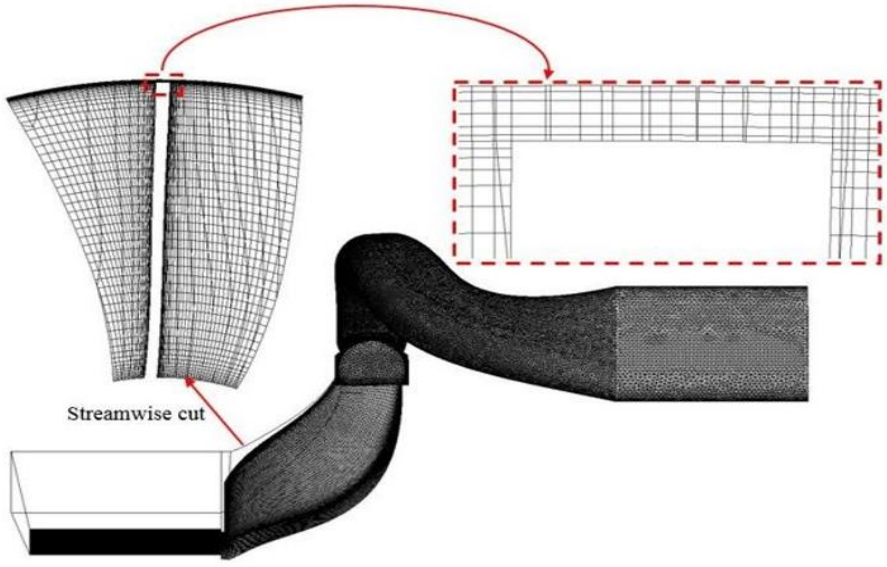

Figure 3.11: Mesh for baseline low-speed centrifugal compressor stage

For the high-speed compressor stage, the mesh study for the impeller subdomain yields 330, 45 and 50 nodes in the *meridional, pitch and radial* directions, respectively. There are 9 spanwise nodes in the tip clearance region with 20 mesh nodes over the impeller tip plane to capture accurately the tip clearance flow. This resolution is sufficient to provide reliable results according to reference [46]. The mesh for the short intake has 15 nodes in the streamwise direction with the same number of pitchwise and radial elements as the impeller to preserve mesh conformity with the adjacent impeller subdomain. The fishtail diffuser subdomain resulting from the mesh study has 2.298 million elements including 20 prism layers at the walls with a growth rate of 1.15 to capture the viscous boundary layer and its possible separation. The end duct subdomain mesh consists of 355,200 elements without prism layers since its lateral boundaries do not represent any physical wall and is set as free-slip. The average y^+ value at solid surfaces varies approximately between 5 for fishtail diffuser walls to 10 for impeller and intake walls. While the CFX Solver Modelling Guide [44] suggests a y^+ value of less than 2 for the SST model, this small y^+ value would significantly increase the computational cost. To resolve this issue, a near wall treatment has been considered in CFX which can smoothly shift between low-Reynolds numbers (linear velocity profile) near wall to wall function formulation (logarithmic velocity profile). This automatic wall treatment option uses a hybrid of low-Reynolds number and wall function models for y^+ values higher than 2 to provide an accurate prediction of the viscous wall effects [44].

For the mesh of the baseline low-speed compressor, the mesh study resulted in an impeller subdomain mesh with 150, 70 and 50 nodes in the *meridional, pitch and radial* directions, respectively. There are seven spanwise nodes in the tip clearance region which is enough to capture the tip clearance flow structures adequately [46]. The mesh for the intake has 50 nodes in the streamwise direction with the same number of elements in the pitch and radial directions as impeller to preserve similar mesh density between the two adjacent subdomains. The fishtail diffuser subdomain has a total of 1.854 million elements with 20 prism layers on its walls with a growth rate of 1.075 in order to capture the behaviour of the boundary layer. The end duct subdomain mesh consists of 212,000 elements without prism layers on its non-physical inviscid or free-slip walls. The average y^+ value at solid surfaces varies approximately between 7.5 for fishtail diffuser walls to 9.5 for impeller and intake walls, which is higher than the minimum suggested value of 2 [44].

3.4.3 Numerical Setup for stand-alone impellers

To simulate the stand-alone impeller, the diffuser and end-duct subdomains are replaced by a long radial vaneless diffuser subdomain, as illustrated in Figure 3.12 for both high-speed and low-speed impellers. A periodic condition is applied to the lateral boundaries of this diffuser subdomain. The endwalls of the diffuser are set as free-slip (inviscid) to ensure that no flow separation (thus source of stall) occurs in this diffuser so that any source of stall lies in the impeller alone. The structural mesh for the inviscid diffuser is generated in ICEM-CFD. The number of mesh elements in the circumferential and axial directions match those of the impeller exit plane with 150 and 80 elements in the radial direction for high-speed and low-speed, respectively, yielding 200,226 and 128,061 elements in total.

3.4.4 Numerical setup for flow control strategies

When flow control strategies such as casing treatments are implemented, the associated subdomains are added to the compressor computational subdomain to which the strategy is applied (usually impeller or diffuser subdomains). For a stationary flow control subdomain over the rotor, a *Frozen Rotor* interface is applied if the technique is axisymmetric (e.g. circumferential groove) or a *Transient Rotor-Stator* (sliding plane) interface if the technique is non-axisymmetric (e.g. slots or flow recirculation pipes). In contrast, any stationary flow control subdomain will be linked to the diffuser subdomain via a simple GGI interface. Although a mesh study was not done on the subdomains of the flow control devices, their mesh densities are matched as closely as possible to the compressor subdomains with whom they share an interface. In addition, the $y+$ values of the flow control subdomain mesh are on the same order of magnitude as those of the compressor subdomain.

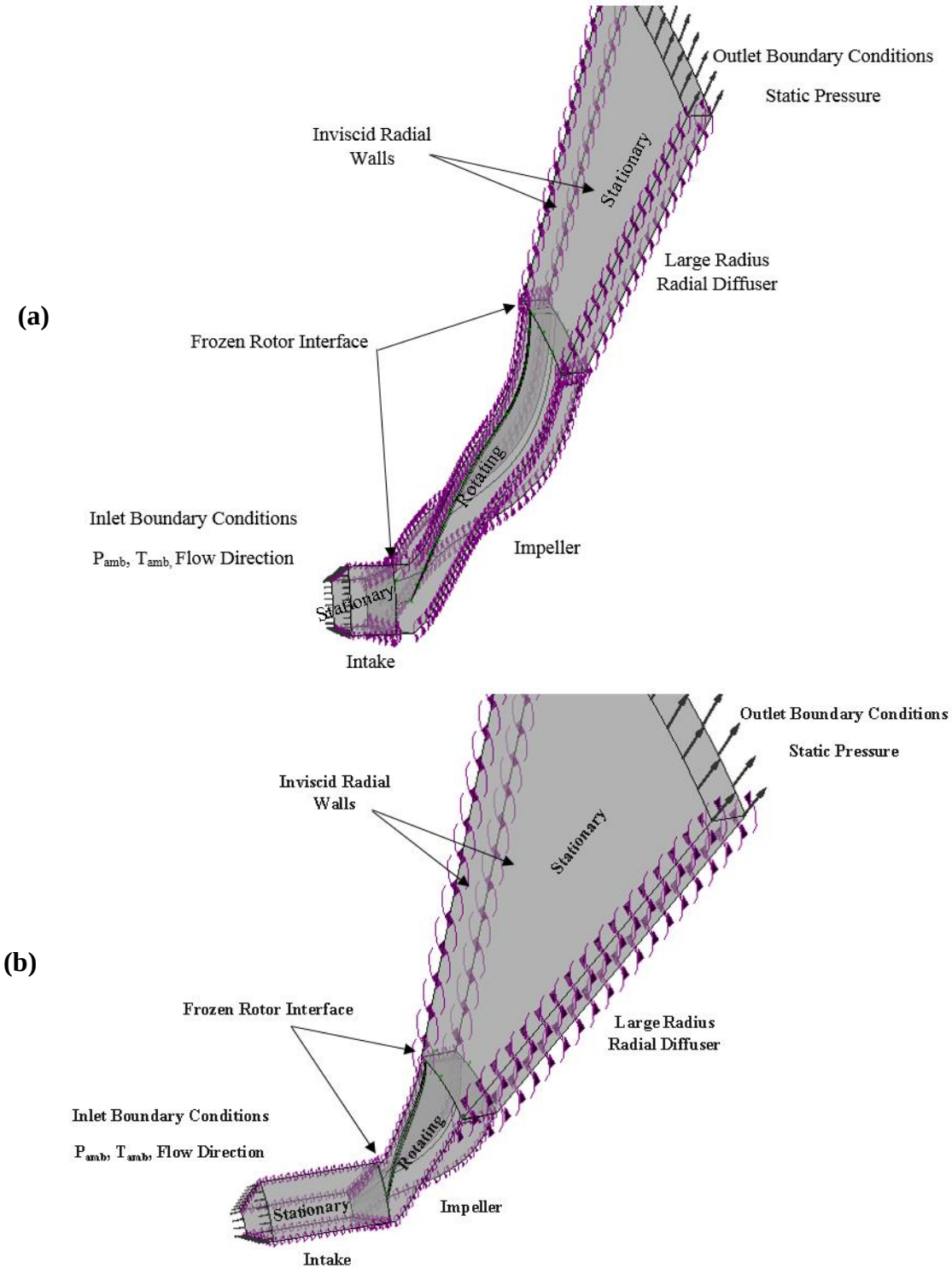

Figure 3.12: Computational domain and boundary conditions for stand-alone impeller simulation at (a) high-speed and (b) low-speed

Circumferential Groove

Figures 3.13 and 3.14 show the addition of the circumferential groove (and its mesh) on the impeller shroud of the high-speed and low-speed baseline compressors, respectively. In both cases, a semi-circular 5 mm radius circumferential groove was placed (measured at groove centre) at about 40% shroud curve length on the impeller casing to cover the axial extent of the recirculation zone seen on the baseline compressors. The circumferential extent of groove subdomain covers one impeller blade pitch to match that of the impeller subdomain. As such, the lateral boundaries of the groove use a rotational periodic boundary condition. A *Frozen Rotor* interface is defined between the impeller shroud and groove lower boundary (axisymmetric treatment). The groove's radially outer boundary is considered as no-slip wall.

For the high-speed compressor, the groove subdomain contains 105,800 mesh elements. The number of mesh elements in the meridional and circumferential directions conforms to that of the adjacent impeller subdomain. The y^+ value at the groove's wall is 10.4. For the low-speed compressor, the groove subdomain contains 51,200 mesh elements with a y^+ value of 9.1 at the groove's wall.

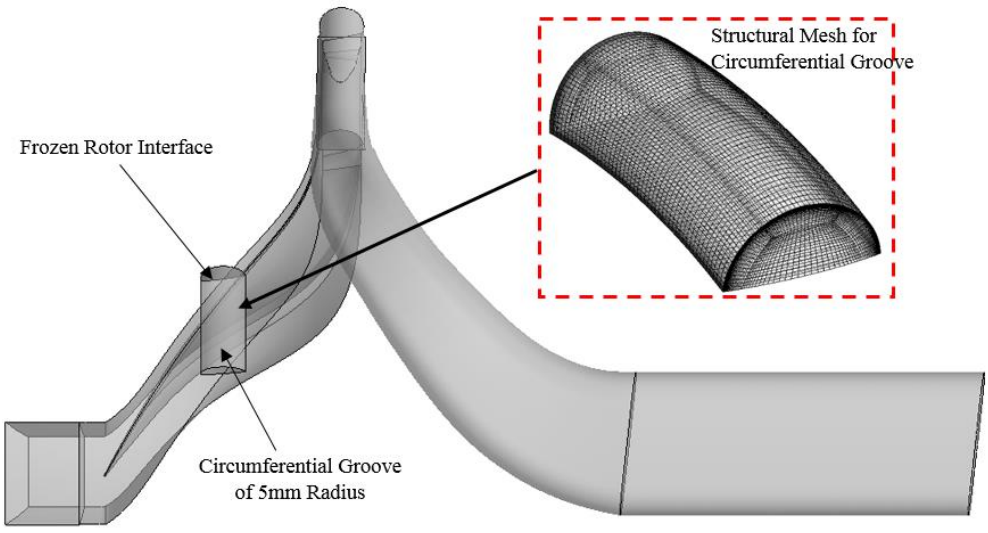

Figure 3.13: Computational domain and mesh for circumferential groove casing treatment on high-speed baseline centrifugal compressor

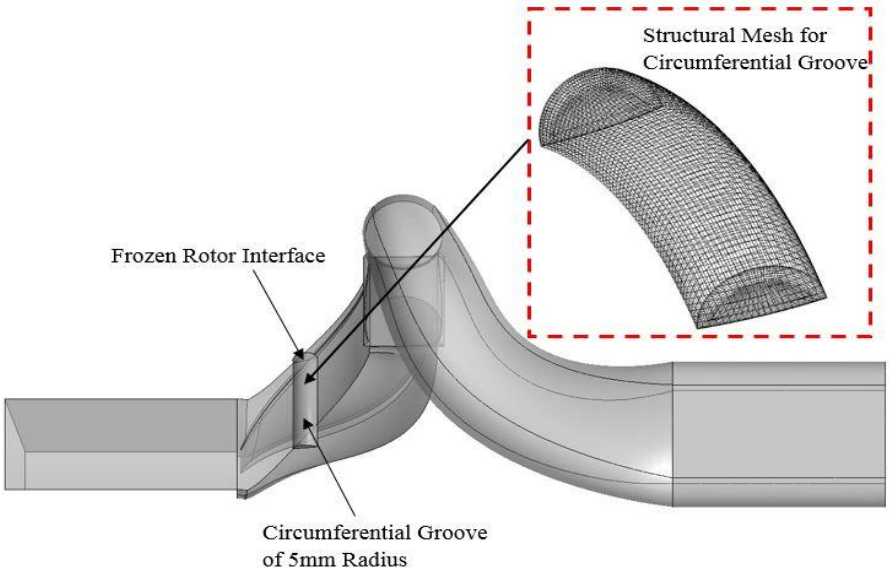

Figure 3.14: Computational domain and mesh for circumferential groove casing treatment on low-speed baseline centrifugal compressor

Slots

Figures 3.15 and 3.16 show the application of slots casing treatment (and associated mesh) to the impeller shroud of the high-speed and low-speed baseline compressors respectively, consisting in each case of three slots per impeller blade passage, placed at about 40% shroud curve length (centre of the local flow recirculation zone) on the impeller shroud. The integration of the slots to the compressor domain is problematic due to the individual slots subdomains not being circumferentially periodic. The solution was to insert a thin axisymmetric subdomain between the slots and impeller subdomains, extending radially outward from the shroud and with circumferential extent equal to the blade impeller blade passage width, as shown in the right insets of Figures 3.15 and 3.16. This thin subdomain is stationary and attached to all three slots subdomains through a simple GGI interface to account for the mesh change across the interface. An axisymmetric sliding plane fluid-fluid GGI interface is placed between the thin subdomain and the impeller subdomain. The lateral boundaries of the thin subdomain use periodic boundary conditions. The mesh density of the thin subdomain and slots subdomains are set similar to the adjacent impeller subdomain.

The initial slot geometry was set as semi-circular skewed slots with a skew angle of 60 degree (circumferential lean in impeller rotation direction) and 50% open area ratio (ratio of slots open area to the total area over slot meridional extent) based on the work by Djeghri *et al.* [34] on mixed-flow compressors. However, some preliminary optimization was carried out to improve the stall margin extension. For the high-speed baseline compressor stage, the resulting modified geometry consisted of unskewed (radial) with a semi-oval shape (to improve streamwise injection component) and dimensions as shown in Figure 3.15. The mesh of the slots subdomain has 172,000 elements with an average y^+ value of around 8.2 on the slot solid walls.

For the low-speed compressor, the preliminary optimization exercise yielded semi-circular slots that are staggered perpendicular to the local blade camber such that the flow ejected from the slots to increase the streamwise component of the flow injection, as shown in Figure 3.16. The slot radius, length and average width are 9.36, 18.73 and 7.05 mm, respectively. The mesh for the slots subdomain contains 34,800 elements with an average y^+ value of around 7 on the slot solid walls.

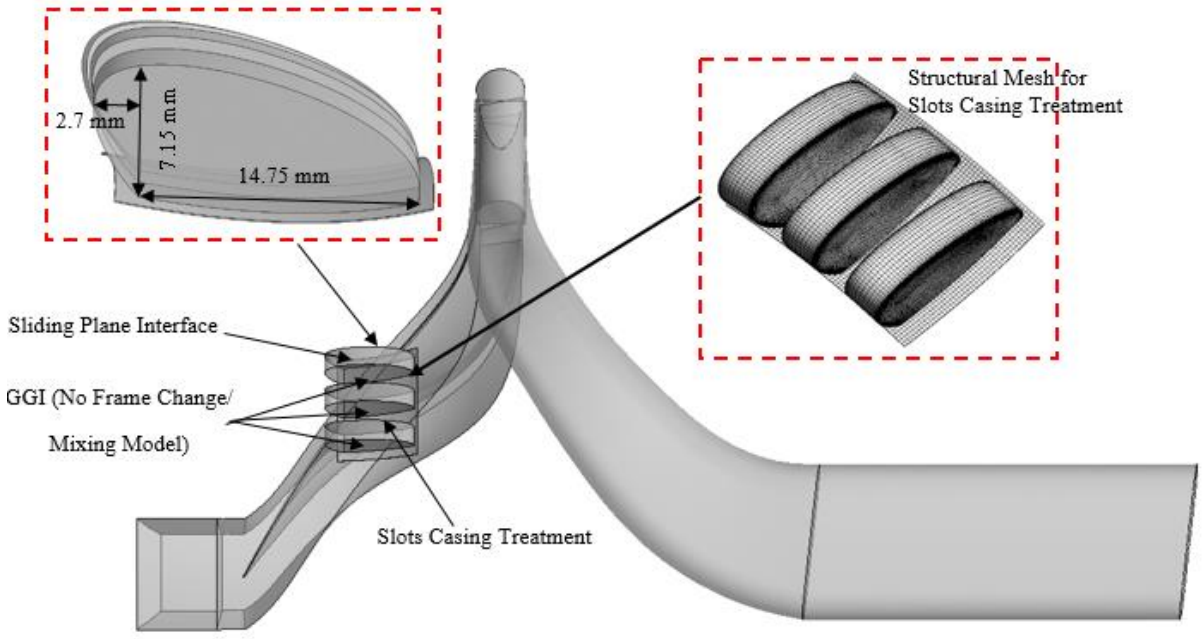

Figure 3.15: Computational domain and mesh for slots casing treatment on high-speed baseline centrifugal compressor

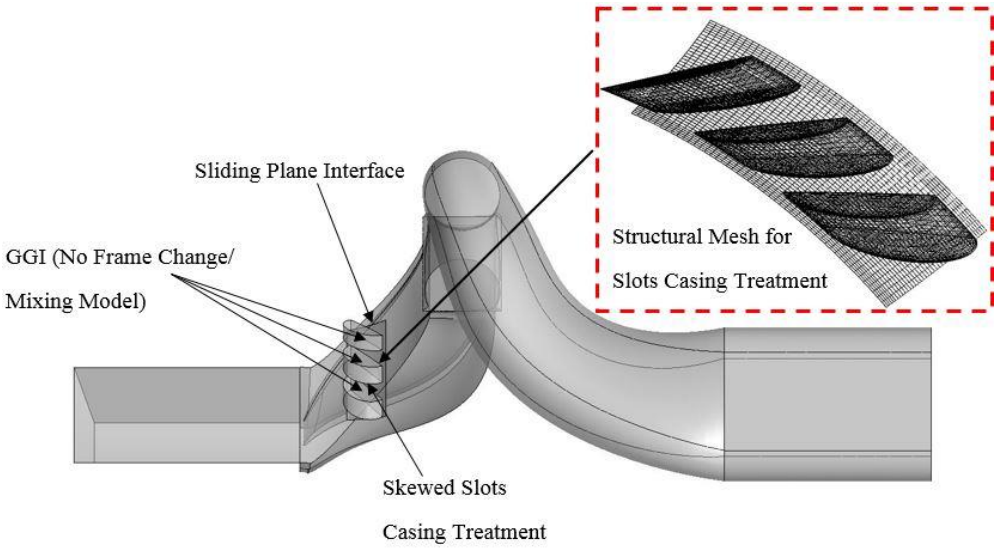

Figure 3.16: Computational domain and mesh for slots casing treatment on low-speed baseline centrifugal compressor

Impeller Recirculation Pipe

Figures 3.17 and 3.18 shows the impeller recirculation pipe applied respectively, to the high-speed and low-speed baseline centrifugal compressors, with one pipe per impeller blade passage. In both cases, the injection port is set at 30% shroud curve length (start of flow recirculation region) with an injection direction that is close to the local impeller gas path angle to maximize the streamwise velocity of the injected flow. The suction port is placed near the impeller exit without interfering with the diffuser vaneless region (taking into account the suction port diameter) which is 90% and 75% shroud curve length location for high-speed and low-speed impellers, respectively. The diameter of the suction/injection holes is set to provide a mass flow recirculation ($\dot{m}_r$) on the order of 1% of the passage mass flow ($\dot{m}_p$) at the design mass flow, with its central portion enlarged to reduce the flow velocity and thus minimize viscous losses. Similar to the slots casing treatment, the domain architecture involves placing two thin subdomains placed between the pipe openings and the impeller subdomain, illustrated in the right insets of Figures 3.17 and 3.18. These subdomains have a periodic boundary condition on their lateral boundaries. A simple GGI interface is considered between pipe's inlet/outlet and the thin subdomains (all stationary) and a sliding plane

fluid-fluid GGI interface is placed between these thin subdomains and the impeller subdomain. The mesh for the thin subdomains has a density similar to that of the impeller subdomain.

For the high-speed compressor, the impeller recirculation pipe has 2.4 mm diameter injection and suction ports providing a recirculated mass flow rate ($\dot{m}_r$) of 0.8% of the passage flow ($\dot{m}_p$) at the design mass flow. The pipe subdomain mesh is unstructured with 373,000 tetrahedral elements, having 15 layers of prism mesh on its walls with a growth ratio of 1.1. The average y^+ value at solid surfaces is around 2.4.

The recirculation pipe for the low-speed compressor has a diameter of 12 mm for the injection/suction ports, providing a recirculated mass flow ratio ($\dot{m}_r/\dot{m}_p$) of 1.0% at the design mass flow. The mesh for this pipe subdomain has 165,000 elements with an average y^+ value of around 5 at solid surfaces.

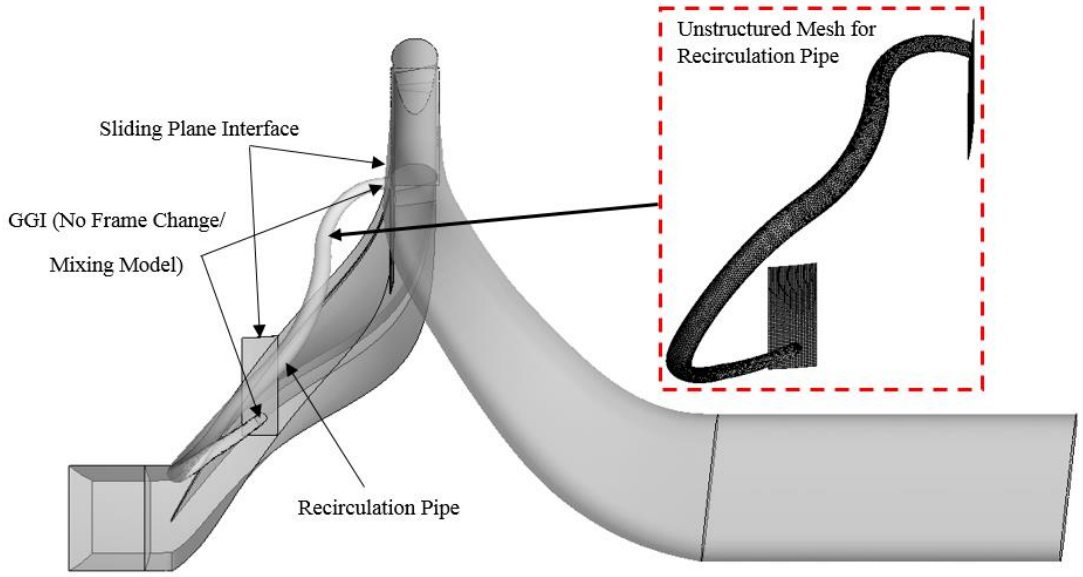

Figure 3.17: Computational domain and mesh for impeller recirculation pipe on high-speed baseline centrifugal compressor

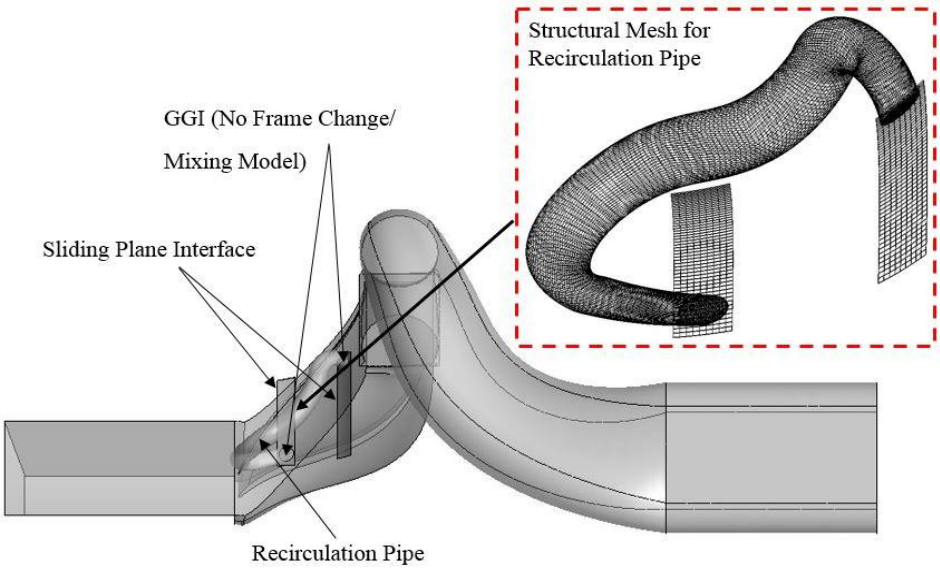

Figure 3.18: Computational domain and mesh for impeller recirculation pipe on low-speed baseline centrifugal compressor

Diffuser-to-Impeller Recirculation Pipe

The application of a diffuser-to-impeller recirculation pipe one per impeller blade passage, to the high-speed and low-speed baseline centrifugal compressors are shown in Figures 3.19 and 3.20, respectively. The direction and location of the injection port are the same as that for the impeller recirculation pipe, while the suction port is placed near the exit of the diffuser pipe on the suction side. The pipe suction/injection hole nominal diameter is sized to give a recirculation mass flow ratio ($\dot{m}_r/\dot{m}_p$) of around 0.5%. There is a slight enlargement of the pipe in the middle section. In terms of domain architecture, the integration of the injection port with the impeller subdomain is done through the thin subdomain structure, interface and periodic lateral boundary as was the case for the impeller recirculation pipe and the slots casing treatment. On the other hand, since the suction port is on the stationary diffuser subdomain, a simple GGI interface is used between the suction port and the fishtail diffuser wall.

For the high-speed compressor, the injection and suction ports have a diameter of 1.2 mm. This results in a recirculation mass flow ratio ($\dot{m}_r/\dot{m}_p$) of 0.46% at the design mass flow rate. The long pipe has an unstructured mesh made of tetrahedral elements with 15 prism layers with a growth

ratio of 1.1 resulting in an average y^+ value of around 7.5 at solid surfaces. The total number of mesh elements including the thin subdomain is 1.595 million.

For the low-speed compressor, the injection and suction ports have a nominal diameter of 2 mm to provide a recirculated mass flow ratio ($\dot{m}_r/\dot{m}_p$) of 0.34% at the design mass flow. However, larger ports (and pipe) diameters up to 12 mm (as shown in Figure 3.20) were also simulated to provide up to 2.2% of recirculated mass flow ratio to look at the effect of this parameter on stall margin improvement. The mesh in the pipe is the same type with the same number of prism layers and growth ratio as that on the high-speed compressor, resulting in an average y^+ value of around 2 at solid surfaces. The total number of mesh elements, including the thin subdomain, is 1.035 million.

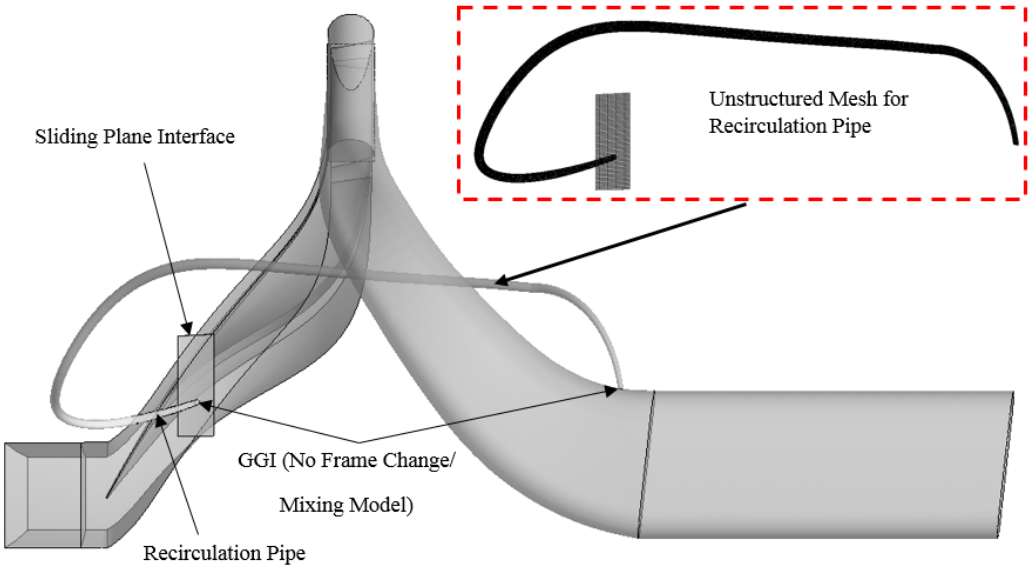

Figure 3.19: Computational domain and mesh for diffuser-to-impeller recirculation pipe on high-speed baseline centrifugal compressor

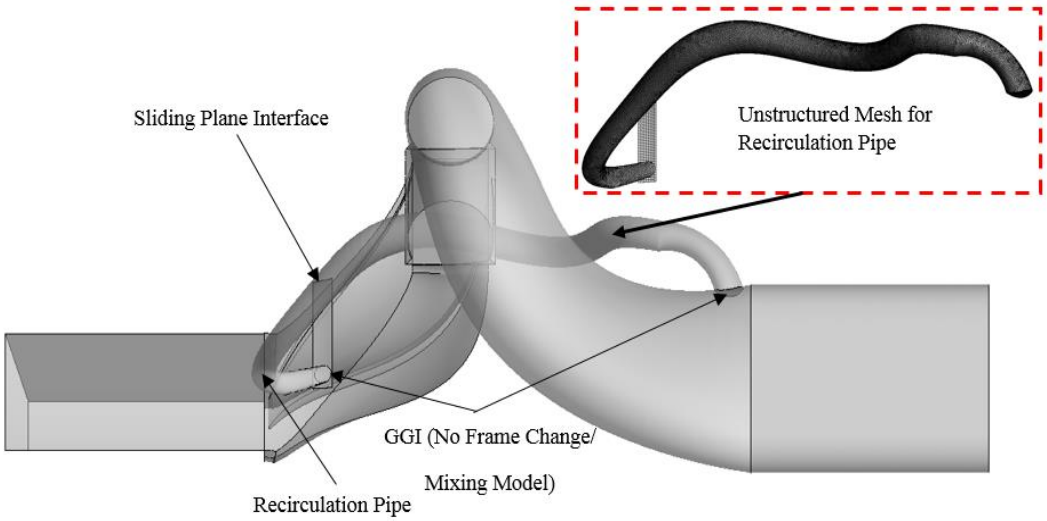

Figure 3.20: Computational domain and mesh for diffuser-to-impeller recirculation pipe on low-speed baseline centrifugal compressor

3.5 Simulation and Analysis Procedure

3.5.1 Simulation procedure

The simulation procedure to obtain the speedline for each baseline compressor stage starts with an unsteady simulation at a low initial value of the throttle constant (K_t) to get stable solution close to choke. The time-step size is chosen based on a sensitivity study in Appendix C. According to this study, the optimum number of iterations per impeller blade passage is set to be 10. This is also in line with the suggested number required to adequately capture the flow physics[44]. For each gradual increase in the value of K_t, an unsteady simulation is performed using the solution of the previous value of K_t as the initial guess to accelerate convergence. The design mass flow is that of the point with the highest isentropic efficiency (calculated as described in Section 3.5.2) and the stall point is the solution at the highest value of K_t for which convergence occurs, also referred to as the convergence limit.

To obtain the speedline for the configurations with flow control, the procedure is similar, except that the first simulation occurs at the baseline design mass flow using a mass flow exit boundary condition. This simulation is first carried out in steady mode (with sliding plane interfaces replaced

by mixing plane interfaces) for about 100 iterations to obtain a semi-converged solution, which is then used to initialize the corresponding unsteady simulation to obtain the final solution. K_t is then gradually increased from its value at the baseline design point for each subsequent unsteady simulation until the convergence limit.

For the unsteady simulations, convergence is reached when either outlet mass flow or static pressure are oscillating around a single value. Since the converged solution from the unsteady simulations are by nature oscillatory due to the impeller-diffuser interaction, the flow field is time-averaged over an integer number of oscillation period. This period is calculated as the time between two consequent peaks in area-averaged static pressure at the diffuser or impeller outlet. All of the analysis is carried out on this time-averaged flow field which incorporates the time–averaged effects of the unsteady flow structures.

For the baseline (no flow control) configurations, an unsteady simulation at a K_t value just beyond that of the last converged solution is performed for which the instantaneous solution at different time steps during the solution divergence (which represent a periodic stall transient) are recorded to look into the flow field breakdown for determination of the stall mechanism.

3.5.2 Calculation of integral parameters

In order to compare quantitatively the effectiveness of each flow control strategy versus the baseline case, a set of performance and stall margin parameters are calculated from the CFD simulations results for each simulated configuration. These parameters include corrected mass flow, total-to-total pressure ratio, isentropic efficiency, non-dimensional loss within the fishtail and stall margin improvement. These parameters rely on total pressures (P_T) and temperatures (T_T) that are mass-averaged from simulation results at strategic planes defined in the compressor domain. Figure 3.21 shows the location of these planes for the compressor stages studied. Plane 1 is the inlet plane which lies over the bellmouth inlet and upstream of the impeller leading edge, Plane 2 is at the interface between the impeller and diffuser subdomains, Plane 3 is at the tongue of the diffuser and Plane 4 is the stage outlet plane, which lies just downstream of the fishtail diffuser pipe exit.

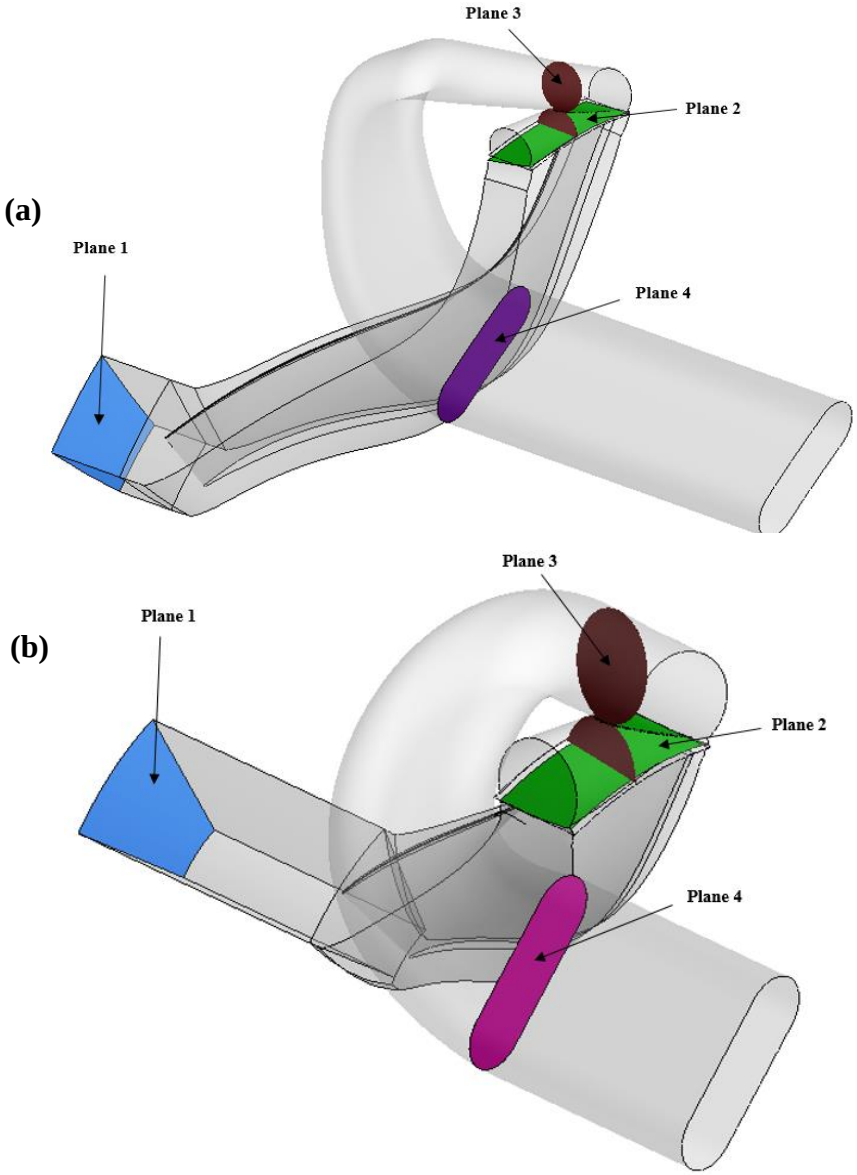

Figure 3.21: Planes for performance calculation inside computational domain of (a) high speed and (b) low-speed baseline centrifugal compressors

To compare performance with different inlet conditions (which is not the case here), a corrected mass flow is usually used in turbomachinery application. It is defined by Equation (3.1), where it is linked to total temperature and pressure on the inlet plane and the reference temperature (288.15 K) and reference pressure (1 atm or 101325 Pa).

$$\dot{m}_c = \dot{m} \times \sqrt{\frac{\frac{T_{tin}}{T_{ref.}}}{\frac{P_{tin}}{P_{ref.}}}} \tag{3.1}$$

The stage total-to-total pressure ratio (PR_{T-T}) is the ratio of the mass-averaged total pressure at the fishtail diffuser exit (P_{T4}) to the inlet total pressure (P_{T1}), as defined by equation (3.2).

$$PR_{T-T} = \frac{P_{T4}}{P_{T1}} \tag{3.2}$$

The isentropic efficiency is calculated with equation (3.3) where n = 4 for stage efficiency (η) and n = 2 for impeller efficiency (η_i).

$$\eta = \frac{\frac{P_{Tn}}{P_{T1}}^{\frac{\gamma-1}{\gamma}} - 1}{\frac{T_{Tn}}{T_{T1}} - 1} \tag{3.3}$$

As shown in Equation (3.4), the diffuser loss coefficient (σ) is defined as the difference in total pressure between the inlet and exit of the fishtail diffuser over its inlet dynamic head (P_{T2} -P_{S2}), where P_{S2} is the area-averaged static pressure at the diffuser inlet (Plane 2).

$$\sigma = \frac{P_{T2} - P_{T4}}{P_{T2} - P_{S2}} \tag{3.4}$$

The diffuser loss can further be broken into the loss coefficients upstream of the tongue (σ_u) and downstream of the tongue (σ_d), as defined by Equations (3.5) and (3.6). Both are non-dimensionalized by the diffuser inlet dynamic head so that the resulting loss coefficients add up to that of the entire diffuser.

$$\sigma_u = \frac{P_{T2} - P_{T3}}{P_{T2} - P_{S2}} \tag{3.5}$$

$$\sigma_d = \frac{P_{T3} - P_{T4}}{P_{T2} - P_{S2}} \tag{3.6}$$

Finally, the stall margin improvement (*SMI*) is defined as the ratio between the difference in corrected mass flow rate between the stall point (convergence limit) with flow control and baseline stall point to the corrected mass flow rate of the baseline (no flow control) configuration, as shown

in equation (3.7). This is the same definition that has been used for the literature review in Chapter 2.

$$SMI = \frac{\dot{m}_{c\,(flow\ control\ stall)} - \dot{m}_{c\,(baseline\ stall)}}{\dot{m}_{c\,(baseline\ stall)}} \tag{3.7}$$

3.5.3 Analysis Procedure

Phase 1: Identification of source of stall

To identify the source of stall for each baseline centrifugal compressor, the simulated speedlines for the stand-alone impeller and stage configurations are compared to determine whether the impeller or the fishtail diffuser is causing the baseline stage to stall. As mentioned in Section 3.1, if the stage stalls at a higher mass flow than the stand-alone impeller, then the diffuser is responsible for stall. Otherwise, the impeller is the stalling component.

The source of the stall can then be investigated through examining the flow field inside the component responsible for stall at points just prior to and including the convergence limit and for time instants during the stall transient with a mass flow lower than the stall point. Specifically, this investigation is performed by plotting the contours of velocity (or if possible streamwise velocity) at different meridional planes as well as the streamlines for the time-averaged flow field at stable operating points and instantaneous flow field at stall transient points. The procedure consists of identifying regions of low flow momentum and/or flow recirculation and to see which region grows as the mass flow decreases to the stall point and continue to grow past the stall point as the flow field breaks down during the stall transient.

When the impeller is responsible for stall, one can also take the opportunity to verify whether the inducer may be responsible for stall through the tip clearance flow through one of the criteria proposed by Vo *et al.* [29, 30] for axial compressors and later assessed by Ashrafi *et al.* [21] for a low-speed centrifugal compressor, namely tip clearance flow spillage at the leading edge. This is done by plotting the time-averaged entropy contours at the impeller blade tip span to see if the

incoming/tip clearance flow interface (region of high entropy gradient) lies at the leading edge plane at the stall point.

Phase 2: Elucidation of Stall Delay Mechanism

For each compressor stage, the speedlines for each of the proposed flow control techniques are obtained from simulations for comparison with the baseline (no flow control or smooth casing) configuration. In each case, the speedline must include a point at a mass flow very close to the stalling mass flow of the baseline compressor stage as well as one at the nominal design mass flow. The comparison is first carried out on integral basis through many of the parameters of Sections 3.5.2. While emphasis is placed on the stall margin extension at this phase, the total-to-total pressure ratio and efficiency at the design point are included to consider the effect on performance of each flow control technique. For the flow recirculation techniques, the recirculated mass flow is calculated and listed from the time-averaged flow field in the recirculation pipe at design mass flow.

The flow field inside the stalling component for two selected flow control techniques (the most successful and one less successful in terms of stall margin improvement) are then compared to that of the baseline (smooth casing) configuration at the baseline stalling mass flow to elucidate the stall delay mechanism. This procedure consists of first plotting the contours of velocity (or streamwise velocity) at different meridional planes as well as the streamlines to see if the flow structure responsible for stall has been suppressed by the flow control techniques. Streamlines are then used to link this region to the flow emanating from the flow control devices to understand how the flow control suppresses the flow structure responsible for stall. The flow fields for the two flow control techniques are compared to see if there is a correlation between the degree of suppression of these structures with the stall improvement numbers to further support the identified flow mechanism.

Phase 3: Identify sources of efficiency loss

As a preliminary investigation into the sources of losses associated with the proposed flow control techniques, the flow control configurations are compared to the baseline (no flow control) case at the design mass flow. An integral comparison is first carried out to get an idea of which section of the compressor stage contribute most to the efficiency penalty in the presence of the flow control. To do this, the stage efficiency for each flow control configuration is first broken into the impeller efficiency and total pressure loss in the diffuser upstream and downstream the tongue (Eqns. 3.5 and 3.6). Through the change in impeller efficiency and loss in each section of the diffuser relative to the baseline case, one can get an idea of the dominant sources of losses caused by each flow control technique.

An examination of the flow field for selected flow control configurations, versus the baseline compressor is then carried out to get an idea of the loss mechanism. This investigation consists of comparing contours of velocity (or streamwise velocity) and turbulence kinetic energy (TKE) to identify location of high velocity gradients and flow mixing, both of which can induce shear and mixing losses.

CHAPTER 4 HIGH-SPEED CENTRIFUGAL COMPRESSOR RESULTS

4.1 Stalling Component

As outlined in Section 3.1, simulations of the baseline high-speed centrifugal compressor stage and its impeller (coupled with an inviscid radial diffuser) are first carried out up to their respective stall points to identify whether the stall is initiated in the impeller or the diffuser. Figure 4.1 shows the resulting (time-averaged) speedlines of these two configurations, with points *A* and *Ai* being the last stable operating point (also referred to as convergence limit or stall point) for the stage and impeller configuration, respectively. The dashed points labelled "*S*", "*S1, S2 and S3*"are instantaneous points recorded during divergence (also interpreted as periodic stall transient) as the simulation is pushed beyond the convergence limit, for which the mass flow time-trace is shown in Figure 4.2. Points *B* and *C* are respectively, the second-to-last stable point and the design point for the stage.

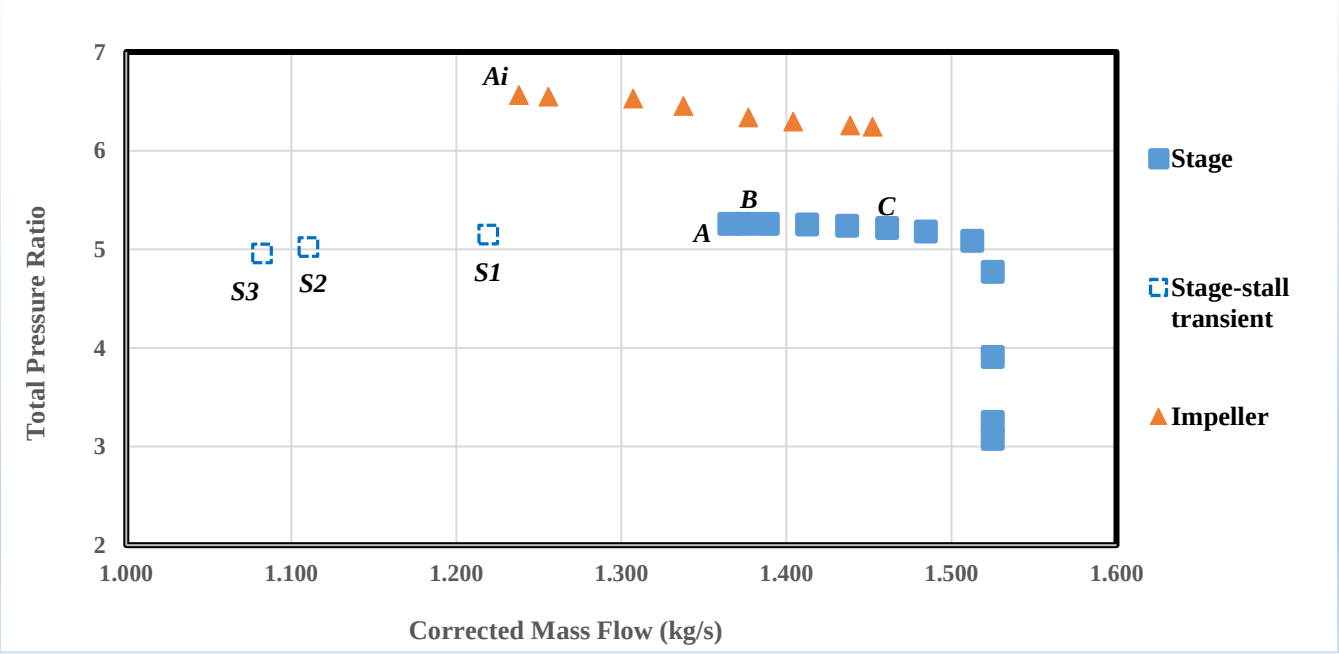

Figure 4.1: Time-averaged speedlines for high-speed centrifugal stage versus impeller

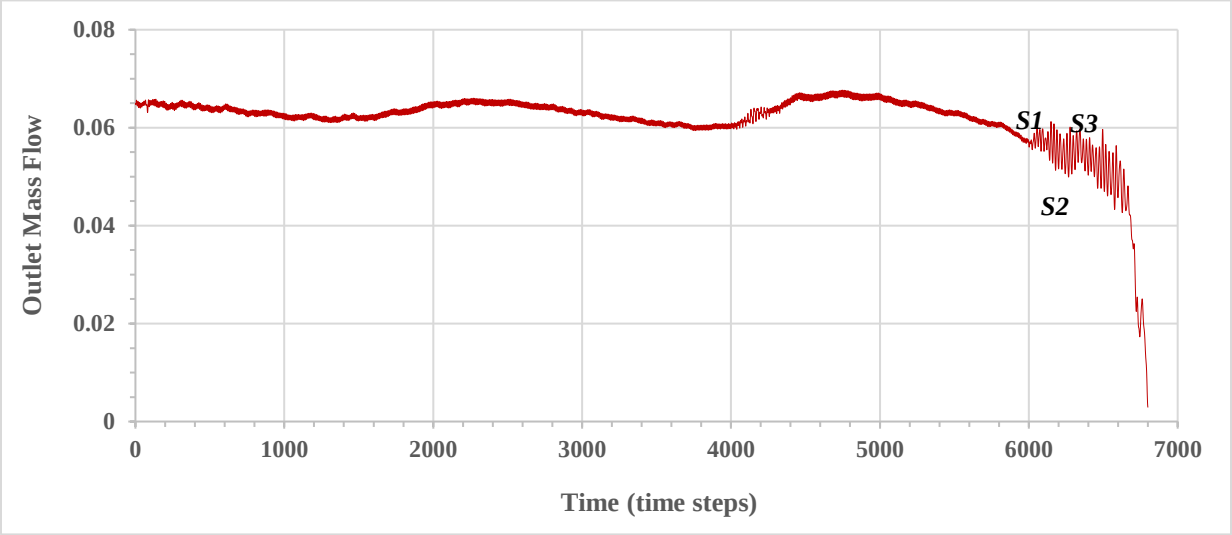

Figure 4.2: Outlet mass flow time-trace during (axisymmetric) stall transient of high-speed stage

Since the impeller stalls at a much lower corrected mass flow rate than the stage (points *Ai* versus *A* in Figure 4.1), it can be inferred that the fishtail diffuser is the source of stall for the baseline stage.

An investigation of the near-stall flow field in the impeller also supports this conclusion. First Figure 4.3 plots the time-averaged static entropy contours at the impeller blade tip for the last stable point *A* on the stage speedline of Figure 4.1 to look for any sign of tip clearance flow spillage at the leading edge, shown in Chapter 2 to be a criterion for rotating stall inception in axial compressors and also seen on mixed-flow compressor [34] and a centrifugal compressor [21]. Figure 4.3 indicates that the incoming/tip clearance flow interface is still downstream of the blade leading edge such that stall is not caused by tip clearance flow in the inducer.

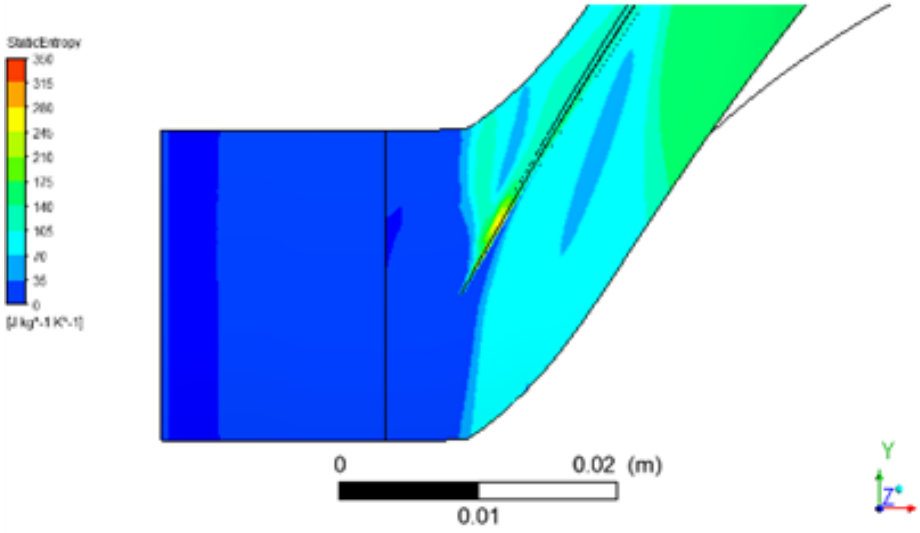

Figure 4.3: Time-averaged static entropy contours at impeller tip at stall point (point *A*) for high-speed centrifugal stage

Looking at the exducer flow field, Figure 4.4 plots the streamwise velocity contours at different planes in the impeller passage for the last two stable points of the stage simulation (points *A* and *B*). There is no noticeable change in the flow field as the compressor is throttled toward stall from point *B* to point *A*, particularly in the low-speed (blue) regions, which would be expected to grow if stall was initiated in the impeller exducer.

In summary, all evidence points to stall being initiated in the diffuser for which a flow field analysis is carried out in Section 4.2 to find the cause of stall.

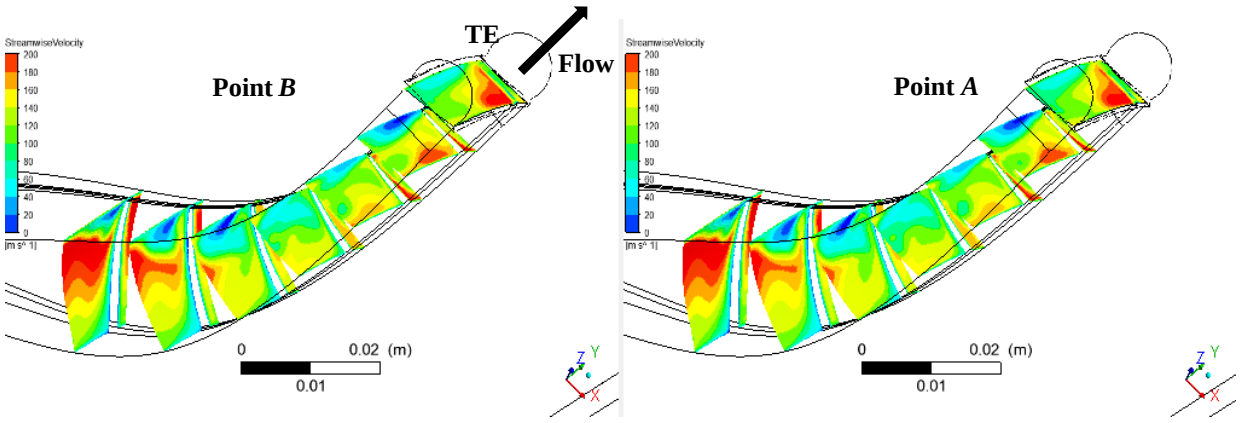

Figure 4.4: Time-averaged streamwise velocity contours at different impeller streamwise planes for the last two stable points of high-speed centrifugal stage

4.2 Stall Mechanism

An analysis of the flow field evolution in the fishtail diffuser from near-stall and post-stall is performed to identify the flow structure associated with stall in the high-speed centrifugal compressor stage. Figure 4.5 plots the time-averaged velocity contours at different planes along the fishtail diffuser for the last two stable points (points *A* and *B*) as well as the instantaneous velocity contours for three time instants of the stall transient (points *S1*, *S2* and *S3*). The plots show two low-velocity regions in the diffuser. The first, referred to as 'Region 1' and shown through the dashed black line linking its location on different planes, is formed on the radially inner surface of the fishtail diffuser and grows as the flow moves toward the differ exit. This region is present for stable operating points and does not seem to change as the compressor is throttled toward stall (points *B* to *A*), nor does it grow much as the mass flow drops in the stall transient. On the other hand, a second low velocity region, referred to as 'Region 2' originating in the radially outer wall of the diffuser and shown with solid line, appears during the stall transient (point *S1*) and grows very rapidly as the mass flow drops (from points *S1* to *S3*). These results point to Region 2 as the flow structure initiating stall in the compressor. Figure 4.6 plots the streamlines on a half-pitch plane of the diffuser for the same points as in Figure 4.5. The results show that significant flow recirculation occurs in Region 2, as highlighted by the black oval and the spatial extent of this

recirculation increases as the stall transient develops. As such, the source of rotating stall for the baseline high-speed centrifugal compressor is flow separation initiated in the radially outer wall of the fishtail diffuser.

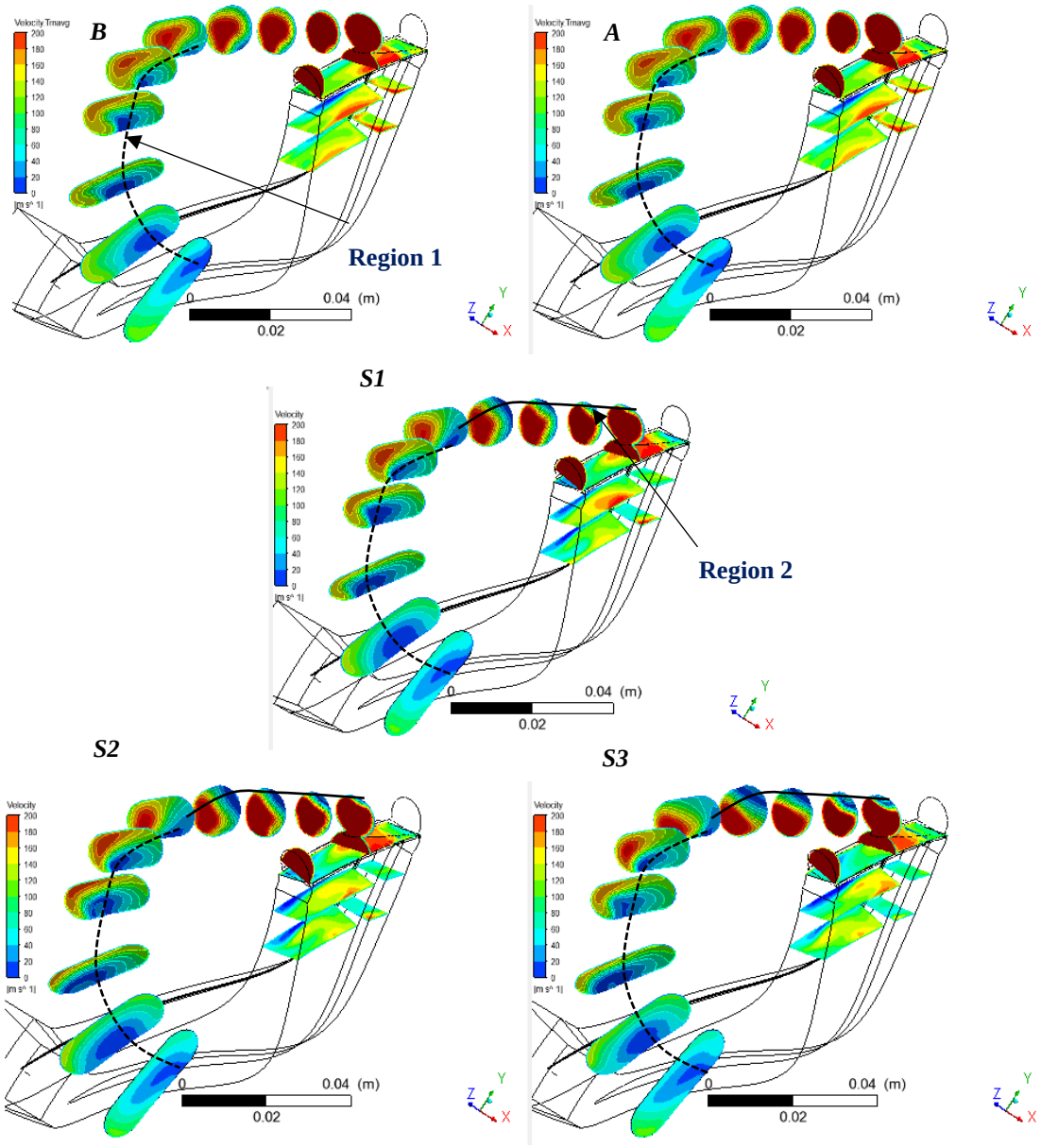

Figure 4.5: Velocity contours at different planes in fishtail diffuser of high-speed stage for near-stall (time-averaged velocity) and post stall (instantaneous velocity) points

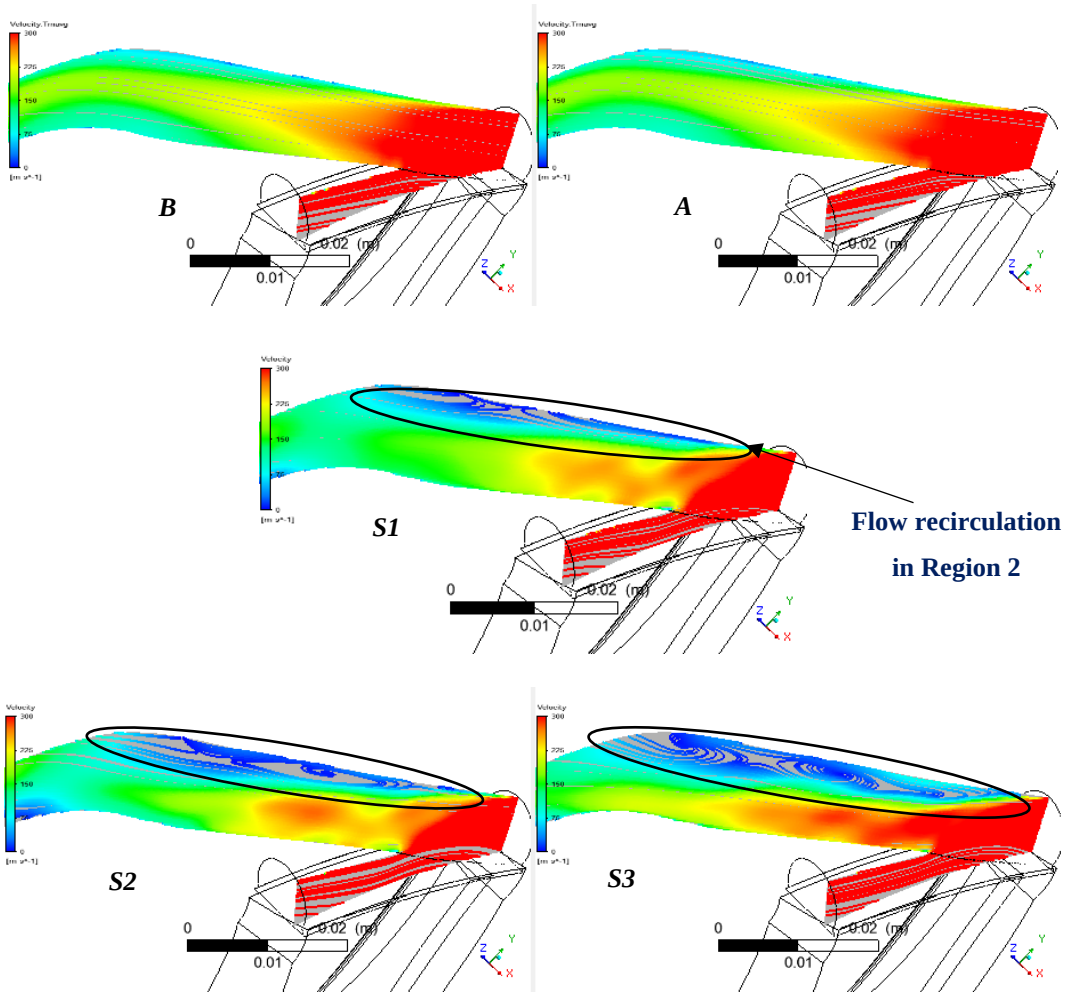

Figure 4.6: Streamlines on half-pitch in upstream part of fishtail diffuser of high-speed stage for near-stall (time-averaged) and post-stall (instantaneous) points

4.3 Effect of Flow Control at Impeller Radial Bend

In this section, the impact of the different flow control techniques applied at the radial bend are assessed, first on an integral basis with regard to performance and stall margin, and then on the flow field level to elucidate the mechanism by which they can suppress stall for centrifugal compressor stages in which the fishtail pipe diffuser is the source of stall.

4.3.1 Integral Effect

Table 4.1 compares the performance parameters (stage total pressure ratio and isentropic efficiency) *at the design mass flow* and the stall margin improvement for the simulated flow control techniques at the impeller radial bend versus the baseline (smooth casing) configuration for the high-speed baseline centrifugal compressor stage. The techniques are placed in ascending order of stall margin improvement. For techniques involving flow recirculation from far downstream locations, the amount of recirculated mass flow is also listed (*at the design mass flow*, quoted as a percentage of total mass flow). The general trend observed is that stall margin improves at the expense of efficiency. In other words, increase stall margin is generally associated with lower isentropic efficiency (at the design mass flow) which is consistent with past observations for casing treatments in axial compressors [47].

Table 4.1: Integral effect of flow control techniques at impeller radial bend on high-speed centrifugal compressor stage

Flow Control Strategy **High Speed**	PR_{T-T}	η **(%)**	***SMI* (%)**	$\frac{\dot{m}_r}{\dot{m}_p}$ **(%)**
Baseline	5.22	84.01	-	-
Diff-Impeller Recirculation-Pipe	5.20	83.41	3.15	0.46
Slots	5.18	82.73	3.57	-
Impeller Recirculation-Pipe	5.21	83.12	4.96	0.8
Groove	4.87	80.61	9.39	-

It is also noted that the slots casing treatment was also placed and simulated at the impeller leading edge (LE) in order to compare with the data for slots in Table 4.1 to get an idea of the increased effectiveness of placing flow control at the radial bend. As detailed in Appendix D, the results showed that the LE slots provide only a 2.60% stall margin improvement, indicating that flow control at the impeller radial bend can be more effective than at the impeller leading edge for centrifugal compressors exhibiting diffuser stall.

Furthermore, the data in Table 4.1 also shows that the two best techniques for stall margin improvement are the groove and impeller recirculation pipe (RP) with the former providing almost double the stall margin improvement of the latter. Figure 4.7 shows the effects of these two flow control techniques on the speedline of the baseline compressor. Points *Ag* and *Ar* correspond to the stage stall points associated with the groove and impeller recirculation pipes, respectively, while point *Bg* and *Br*, their operating points at approximately the baseline (smooth casing) stalling mass flow (that of point *A*) and *Cg* and *Cr* the corresponding operating points at the design mass flow (mass flow of point *C* in baseline configuration). This Figure allows one to appreciate the significant extension of the operating range (difference in mass flow between choke and stall) provided by these two flow control techniques, along with an idea of the penalty in total pressure ratio. The effect of these two techniques on the flow field will be studied in Section 4.3.2 to elucidate the mechanism by which stall is delayed by flow control at the impeller radial bend. The mechanism associated with loss in performance will be investigated in Section 4.4.

4.3.2 Stall Delay Mechanism

The first step in elucidating the stall delay mechanism is to assess the effect of flow control on the flow structure responsible for stall, namely the low-velocity "Region 2" from Figure 4.5. Figure 4.8 shows the time-averaged velocity contours at different planes along the fishtail diffuser and the streamlines on a half-pitch plane of the diffuser for the stall point with the groove (point *A*g), which is close in mass flow to the stall transient point *S1* for the baseline (smooth casing) configuration. A comparison of Figure 4.8 with the correspond plots for point *S1* in Figures 4.5 and 4.6 indicates that the flow control at the radial bend has eliminated the flow recirculation region (low-velocity

Region 2) alleged to be responsible for stall. Figure 4.9 compares the velocity contours inside diffuser around the stalling mass flow of the baseline (smooth casing) case for the configuration with grooves (point *Bg*) versus the baseline case (point *A*). The results show that relative to the baseline case, the groove increases the flow velocity (reduced boundary layer thickness) at the location in the diffuser where the low-velocity region (Region 2) would form and cause flow separation to initiate stall. By increasing velocity in this region, flow control basically delays the occurrence of Region 2 and associated flow separation to a lower mass flow, resulting in the stall margin improvement.

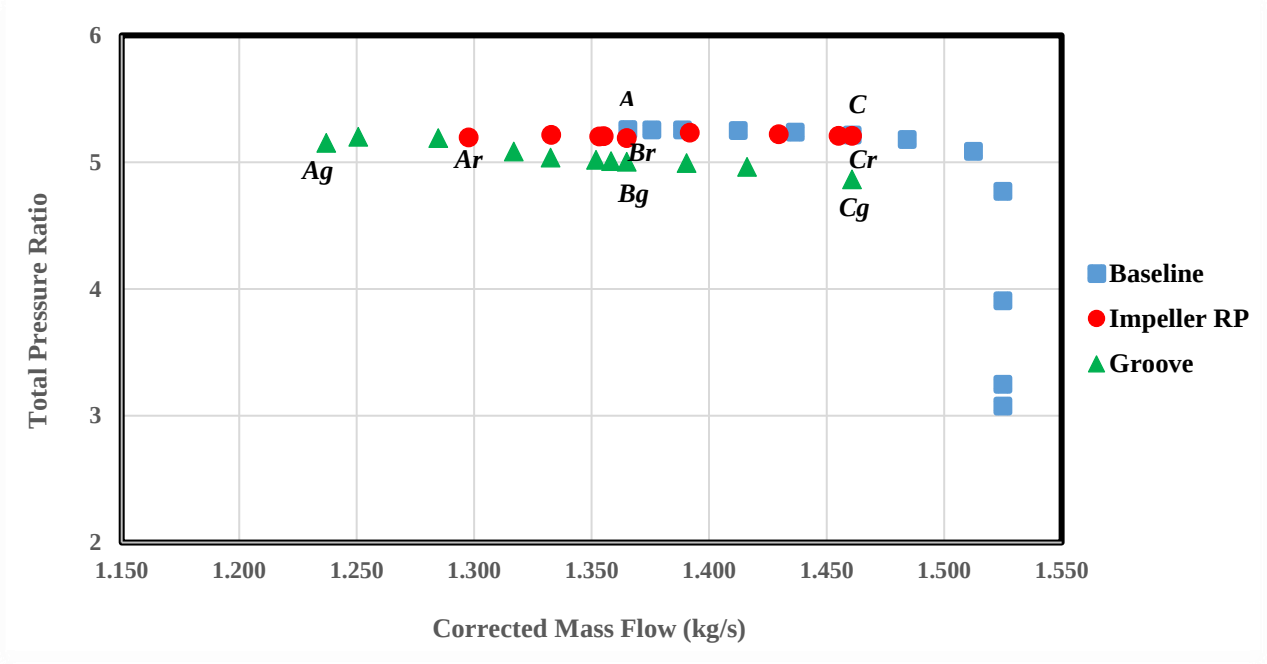

Figure 4.7: Effect of two best flow control techniques on speedline of high-speed centrifugal compressor stage

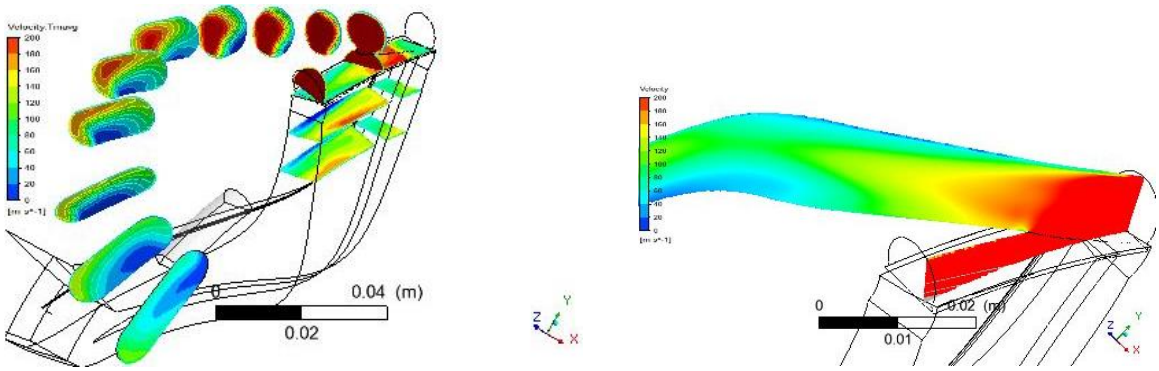

Figure 4.8: Time-averaged velocity contours (left) and streamlines in half-pitch mid-plane (right) in fishtail diffuser at stall point (Point *Ag*) of high-speed stage with groove flow control

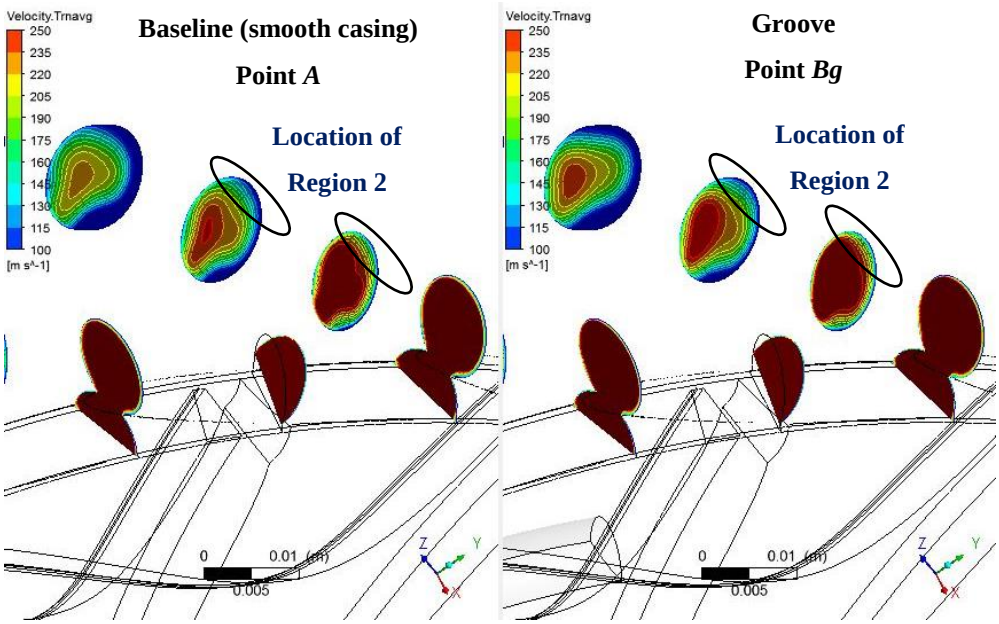

Figure 4.9: Time-averaged velocity contours in fishtail diffuser around stalling mass flow of baseline high-speed stage for the baseline (smooth casing) configuration (Point *A*) versus the configuration with groove (Point *Bg*)

To understand how the flow control at the radial bend increases velocity at the location of Region 2 in the diffuser, one should retrace the flow from the location of Region 2 in the diffuser to the impeller exit plane and then to the flow control location at the radial bend. Figure 4.10 shows the

time-averaged (absolute) streamlines going through the locations of the two low-velocity regions (Region 1 and Region 2) identified in Figure 4.5 for the two best flow control techniques (impeller recirculation pipe and groove) at points *Br* and *Bg*, *i.e.* around the stalling mass flow of the baseline (smooth casing) stage. In addition, the streamlines are continued upstream in the relative (rotating) frame of the impeller blade passage all the way up to the radial bend. By following the streamlines in Figure 4.10, one can see that the flow at the locations of the two low-velocity regions of the diffuser, including that of Region 2 responsible for stall, can be traced back to the region on the lower span and closer to the blade suction surface (SS) at the impeller trailing edge (highlighted by red oval) and then to the shroud at the radial bend where flow is injected into the impeller passage by the flow control devices.

Next, to link the pertinent flow feature in the diffuser with the flow field in the impeller blade passage, one needs to examine the impeller exit plane flow field at the streamlines' location (highlighted by red oval in Figure 4.10). Figure 4.11 plots the absolute velocity contours and relative streamwise velocity contours at the impeller exit plane for the two best flow control configurations as well as for the baseline (smooth casing) case around the baseline stalling mass flow, i.e. for points *Br*, *Bg* and *A*, respectively. Comparison of the contours of absolute velocity for the three cases indicate that the flow control increases the absolute velocity in the lower span region closer to the blade suction side at the impeller trailing edge relative to the baseline case, as highlighted by the ovals. The increase is highly noticeable for the groove configuration, which gives, by far, the largest stall margin increase. The bottom part of Figure 4.11 indicates that this absolute velocity increase in this region corresponds to a decrease in (relative) streamwise velocity in the impeller rotating frame, with the decrease again being most noticeable for the groove configuration. This can be explained by the velocity triangles in Figure 4.12, which show that for a given rotational velocity ($\Omega \cdot r$), the lower streamwise velocity in the rotating frame of the impeller ($V'rel. < Vrel$) corresponds to a higher absolute velocity ($V'stn. > Vstn$) in the diffuser (stationary) frame. In other words, by slowing down the (relative) impeller passage flow in the lower span near the impeller exit suction side, one can increase the (absolute) velocity in the critical location of Region 2 of the fishtail pipe diffuser, alleged to be responsible for stall.

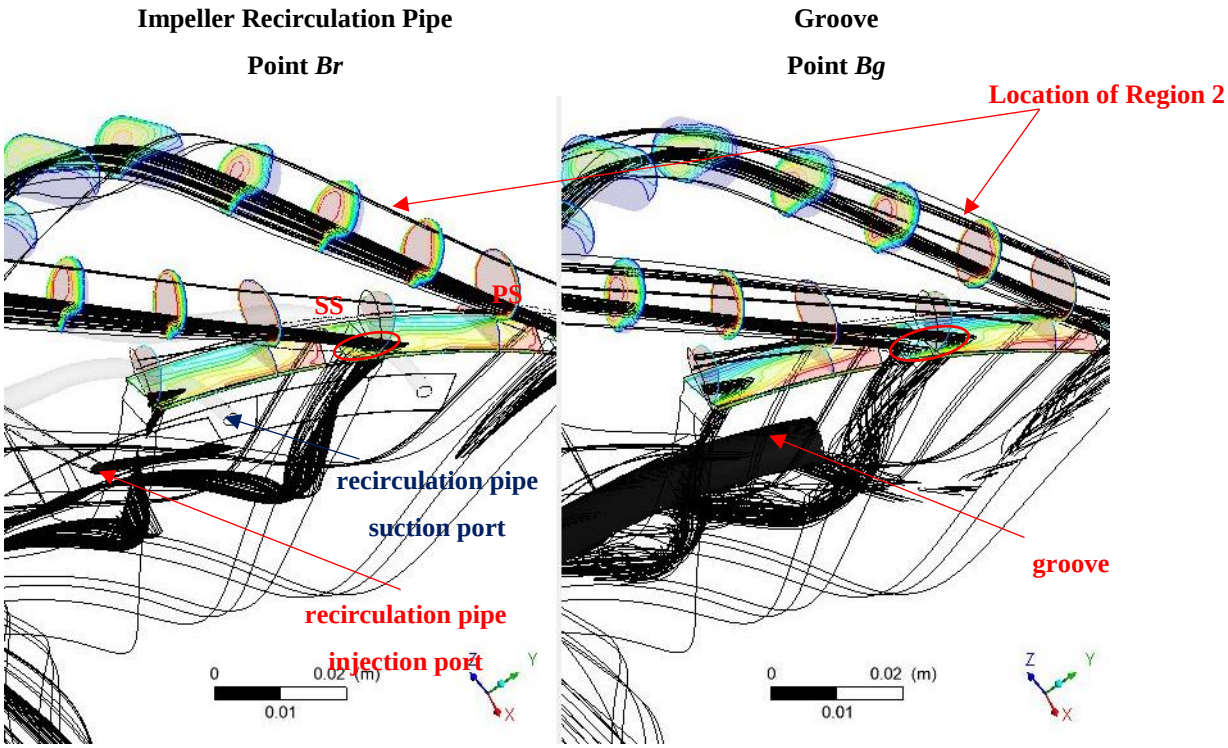

Figure 4.10: Time-averaged streamlines through low-speed regions in diffuser superposed over time-averaged absolute velocity contours in diffuser and time-averaged relative streamwise velocity contours in impeller for points *Br* and *Bg*

The final step to elucidate the stall delay mechanism is to find out how the flow control devices at the radial bend reduce the (relative) streamwise velocity in the lower span region near the impeller blade exit suction side. The time-averaged streamlines in the impeller passage as shown in Figures 4.10 and 4.11 indicate that the flow control devices inject air into the blade passage like a jet in cross flow. As such, this injected fluid has a lower (relative) streamwise momentum than the passage flow. Furthermore, in addition to moving toward the hub, the injected fluid moves toward the suction side as it convects toward the impeller exit plane. This movement toward the suction side, as clearly shown by the axial view of the exducer in Figure 4.13, creates the low-relative streamwise velocity region shown in Figure 4.11 that is responsible for suppressing the flow separation in the diffuser associated with stall.

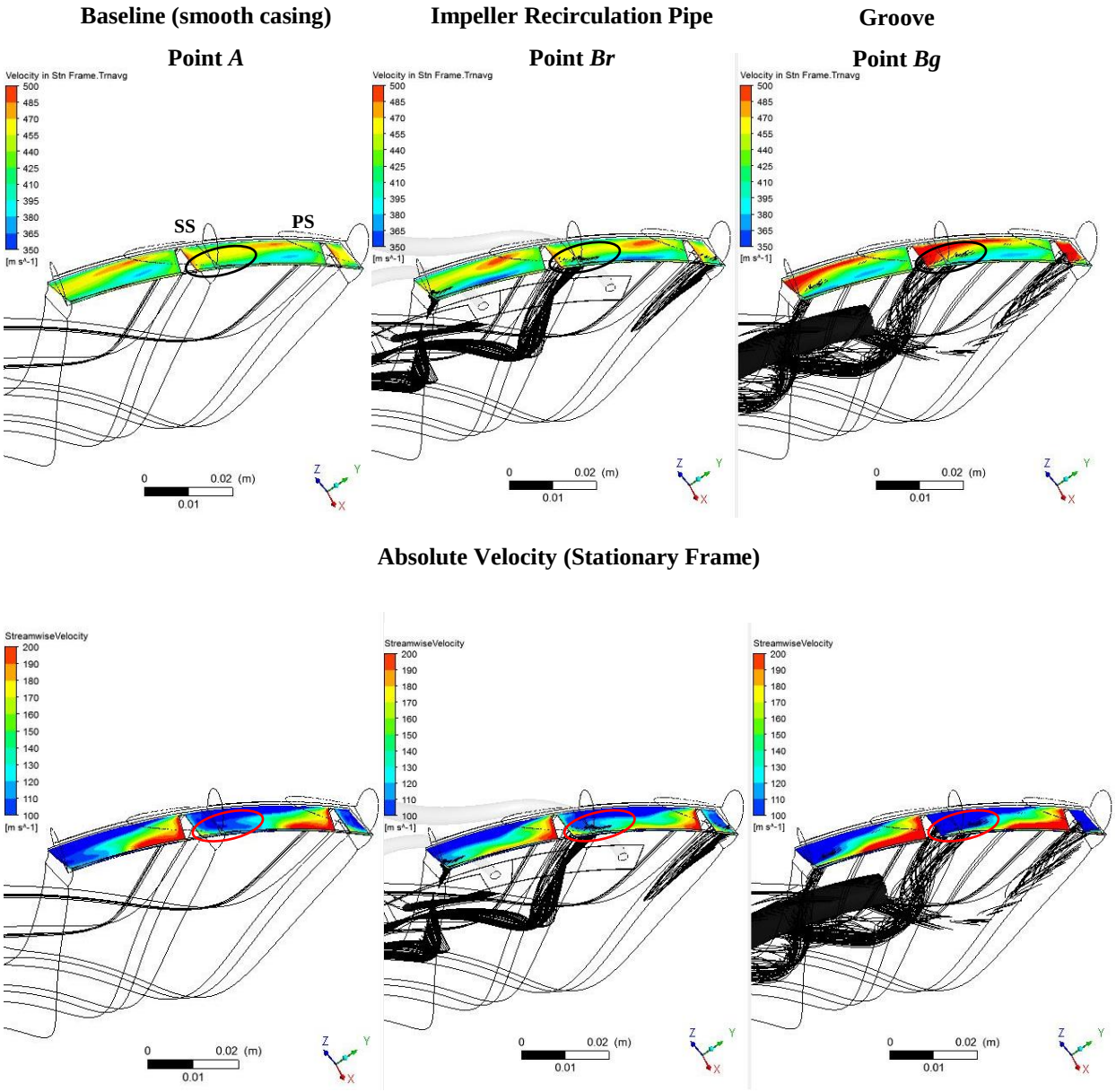

Figure 4.11: Time-averaged relative streamlines emanating from flow control devices and contours of time-averaged absolute velocity (top) and time-averaged relative streamwise velocity (bottom) at impeller exit plane for points *A*, *Br* and *Bg*

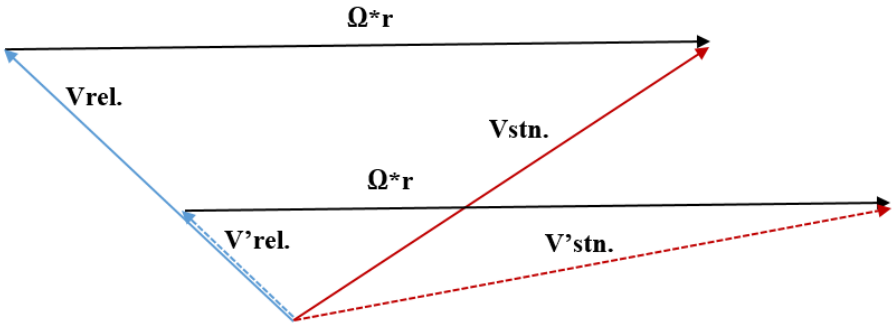

Figure 4.12: Velocity triangle linking relative and absolute velocities at impeller

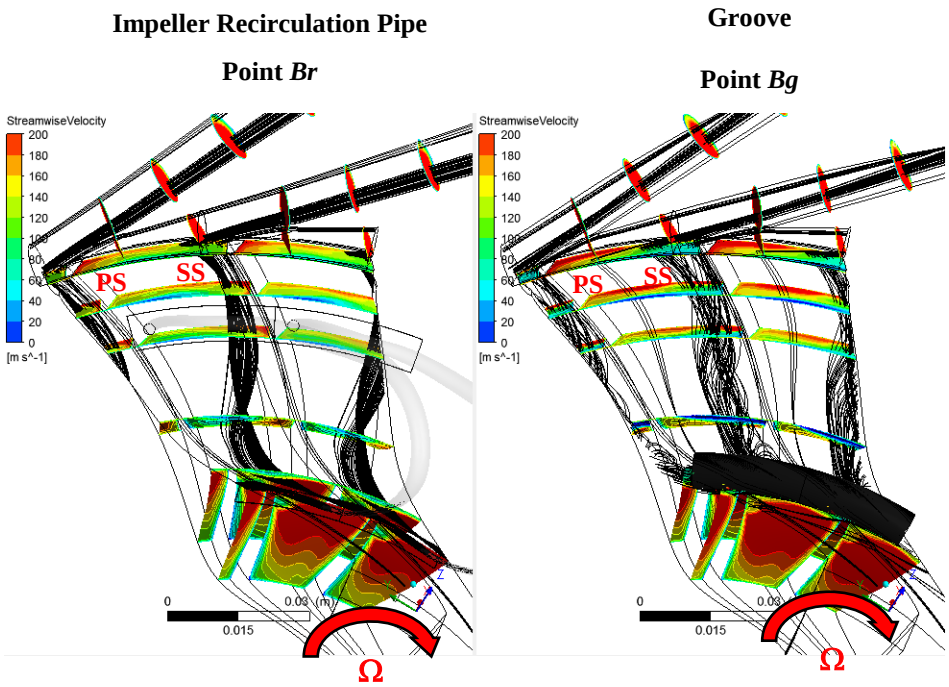

Figure 4.13: Axial view of time-averaged relative streamlines emanating from flow control devices at radial bend for points *Br* and *Bg*

The movement of the injected fluid from the flow control device towards the suction side within the rotating frame of reference of the impeller passage can be explained by considering the balance between the pressure force and the pseudo-forces, specifically the Coriolis force. (The details of the pseudo-forces in a rotating frame of reference are given in Appendix E.) As illustrated in Figure 4.14, in the exducer, the relative velocity component normal to the rotation axis is mainly radial

with a smaller circumferential component. As such, the Coriolis force, which is proportional to the streamwise velocity (V_{strm}), acts in the direction opposite to the rotation. The pressure gradient in the impeller blade passage is set by the mainstream (core) flow. In other words, the static pressure field is such that the net pressure force (F_p) on a mainstream flow particle (Particle 1) balances the Coriolis force ($F_{Cori.}$) to allow the particle to follow the channel (exducer passage) shape. However, a flow particle ejected from the flow control device (Particle 2) experiences a smaller Coriolis force due to its lower streamwise velocity compared to the core flow ($V_{strm2}<V_{strm1}$), but is subjected to the same net pressure force (F_p) as a mainstream flow particle. The result is a net force driving the fluid particle towards the impeller suction surface, illustrated by the dotted line on Figure 4.14.

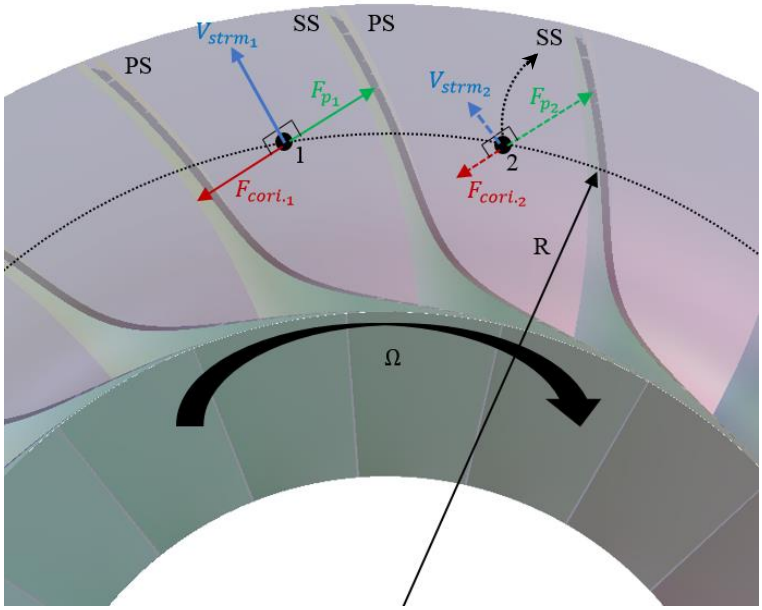

Figure 4.14: Forces acting on flow particles in the exducer rotating frame (axial view)

To summarize the flow control mechanism, the ejected flow from the flow control device at the radial bend has lower relative streamwise momentum than the main passage flow in the exducer, resulting in a movement toward the suction side which, combined with its deep spanwise penetration into the passage, results in a region of low (relative) streamwise momentum at the impeller exit in the lower span close to the suction side in the rotating frame of the passage, but

high velocity in the stationary frame of the diffuser. Since part of the flow from this region goes to the radially outer wall of the diffuser pipe where flow separation forms and initiates stall, the increased flow velocity suppresses flow separation and results in stall delayed.

4.4 Flow Control Impact on Peak-Efficiency and Losses

As can be seen in Table 4.1, the stage efficiency penalty for the configuration with the groove is 3.4%, which is rather large by industry standard. Given that performance, especially (design point) efficiency penalty, is always a factor in the selection of stall margin improvement strategies, this section provides a preliminary investigation of the source of aerodynamic loss at design mass flow incurred by the different simulated flow control techniques at the radial bend. The results should help in optimizing the flow control techniques to reduce efficiency penalty while maintaining/increasing stall margin improvement. The investigation starts with an integral breakdown of the loss by component followed by the examination of the flow field in the impeller and diffuser to look for the sources of loss.

Table 4.2 compares the isentropic efficiency at design mass flow for the baseline (smooth casing) versus those with the studied flow control techniques. Similar to Table 4.1, the configurations are placed in ascending order of stall margin improvement. The stage efficiency (η) is separated into impeller efficiency (η_i) and diffuser loss coefficient (σ) (total pressure loss, non-dimensionalized by diffuser inlet dynamic head), the latter also decomposed into the loss for the part upstream (σ_u) of the elliptical ridges/scalloped leading edge (also called tongue) and the part downstream of the tongue (σ_d).

The data in Table 4.2 indicate that the impeller efficiency decreases when flow control is applied at the radial bend, with the decrease being generally the largest for the cases with the best stall margin improvement. The reason for the efficiency decrease and the observed trend can be seen in Figure 4.15, which shows the streamlines (in the relative frame) of the ejected flow from the flow control devices overlay over contours of turbulence kinetic energy (TKE) at planes downstream of the flow control in the radial bend. This is a jet-in-cross-flow phenomenon that produces mixing

losses due to the directionality difference between the injected flow and the mainstream flow, which is evident from the high TKE seen in the region of the streamlines in Figure 4.15. This Figure also indicates that the losses especially (turbulent) shear loss continue downstream of the initial mixing zone of injection as a result of the velocity gradient due to the difference in streamwise velocity between the injected flow and the mainstream flow that persists all the way to the impeller exit (and beyond). Moreover, it can be inferred from the streamlines that the flow injected from the groove has a noticably deeper spanwise penetration (low streamwise momentum relative to radial momentum) than the impeller recirculation pipe (which was shown in Section 4.3 to make it more effective for stall margin improvement). This deep spanwise penetration translates to higher mixing and shear losses and explains the lower impeller efficiency associated with the groove.

Table 4.2: Efficiency and Loss at design mass flow at high-speed

Flow Control Strategy **High Speed**	η_i **(%)**	**Diffuser Loss Coefficient**			η **(%)**
		σ	σ_u	σ_d	
Baseline (point *C*)	91.42	0.167	0.076	0.091	84.01
Diff-Impeller Recirculation-Pipe	91.22	0.184	0.071	0.113	83.41
Slots	90.52	0.182	0.070	0.112	82.73
Impeller Recirculation-Pipe (point *Cr*)	91.04	0.187	0.068	0.118	83.12
Groove (point *Cg*)	89.67	0.212	0.103	0.109	80.61

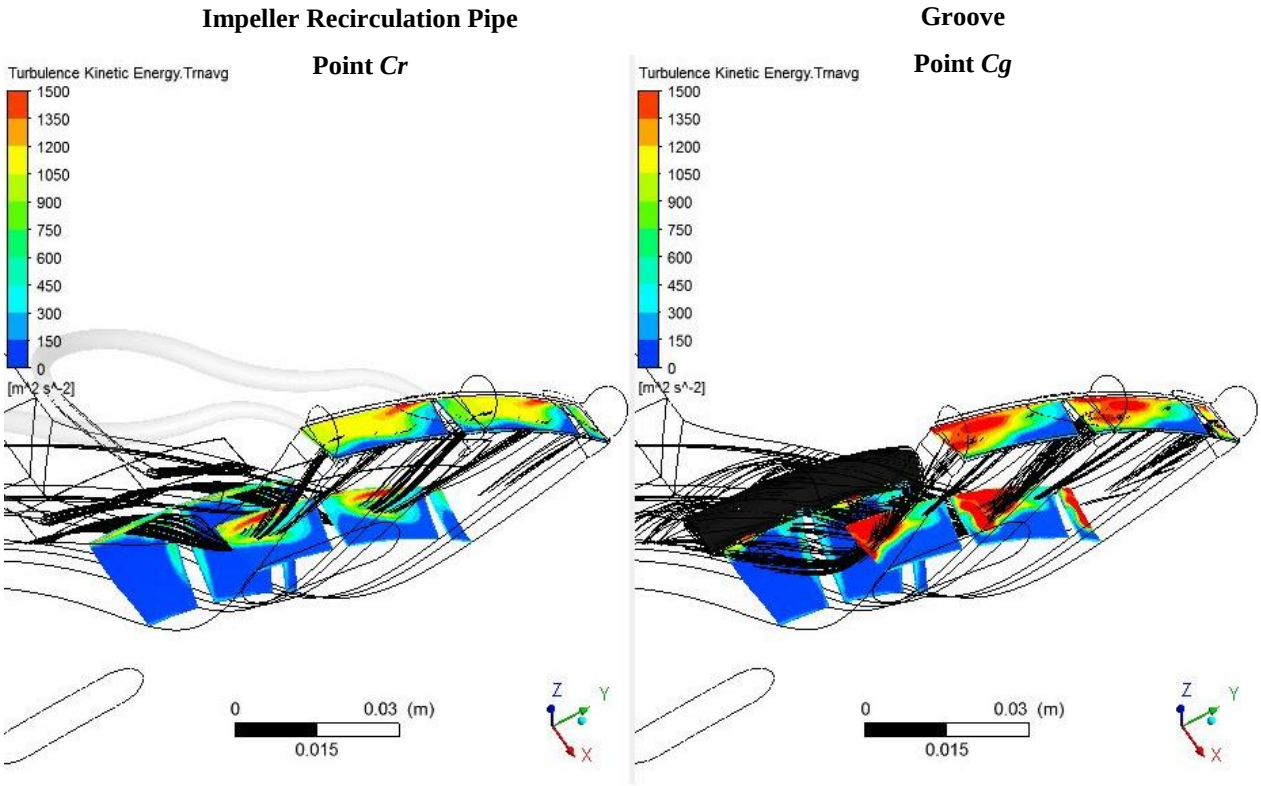

Figure 4.15: Time-averaged relative streamlines emanating from flow control devices and contours of time-averaged turbulence kinetic energy (TKE) at planes downstream of radial bend for impeller recirculation pipe and groove at baseline design mass flow (points *Cr* and *Cg*)

As for the fishtail pipe diffuser, the data in Table 4.2 show that, with the exception of the groove, all simulated flow control techniques resulted in a significant increase in losses in the fishtail diffuser downstream of the tongue, while losses uptream of the tongue remains similar or slightly decreased. For the groove, the increase in losses is spread out over both region of the fishtail pipe diffuser. A comparative analysis of the flow field in the diffuser between the baseline configuration (smooth casing) and those with the impeller reciculation pipe and the groove at the design mass flow in terms of velocity gradient and TKE are shown in Figures 4.16 and 4.17 for the region upstream and downstream of the tongue, respectively.

The zones highlighted by the dashed ovals in Figure 4.16 indicate that, relative to the baseline case, the flow redistribution in the first part of the diffuser (upstream of the tongue) causes a significant increase in the velocity gradient only for the grooved case, which results in larger TKE and

consequently higher shear losses, while having the opposite (albeit lower) effect for the impeller recirculation pipe and reducing losses slightly for this configuration.

On the other hand, Figure 4.17 suggests that downstream of the tongue, the flow redistribution results in significant increase in velocity gradient (and TKE) for the impeller recirculation pipe (and other flow control techniques with the exception of the groove) relative to the baseline configuration resulting in larger shear losses. Howerver, the configuration with the grooves shows little change from the baseline, explaining the lower increases in losses in this region for this configuration relative to the baseline, as shown in Table 4.2.

Baseline (smooth casing) **Impeller Recirculation Pipe** **Groove**

Point *C* **Point *Cr*** **Point *Cg***

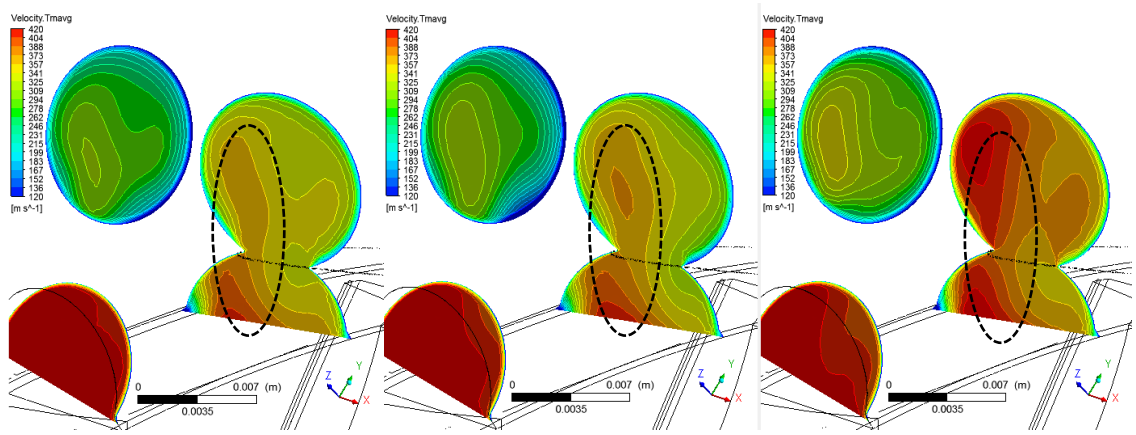

Relative Streamwise Velocity (Rotating Frame)

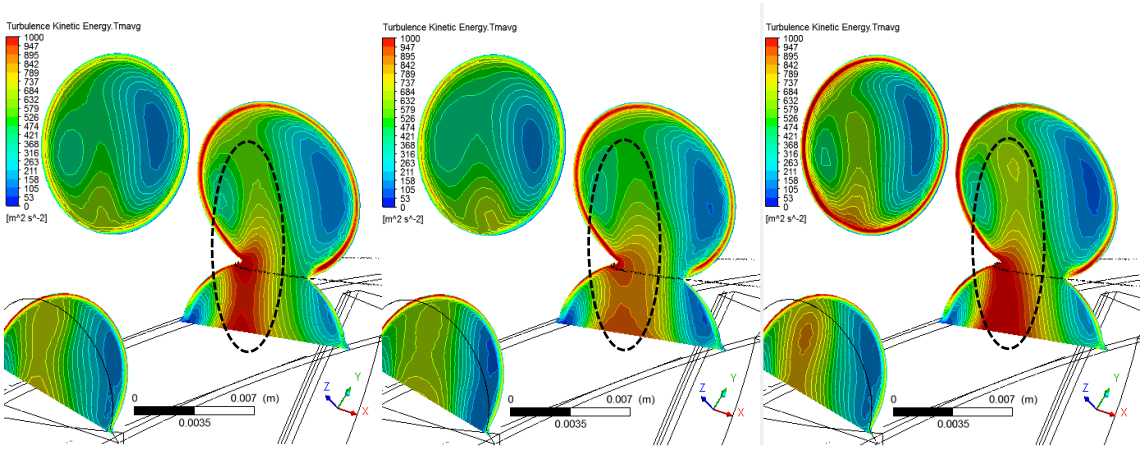

Turbulence Kinetic Energy

Figure 4.16: Contours of time-averaged relative streamwise velocity (top) and TKE (bottom) at planes near fishtail pipe diffuser tongue for baseline (smooth casing), impeller recirculation pipe and groove at baseline design mass flow (points *C*, *Cr* and *Cg*)

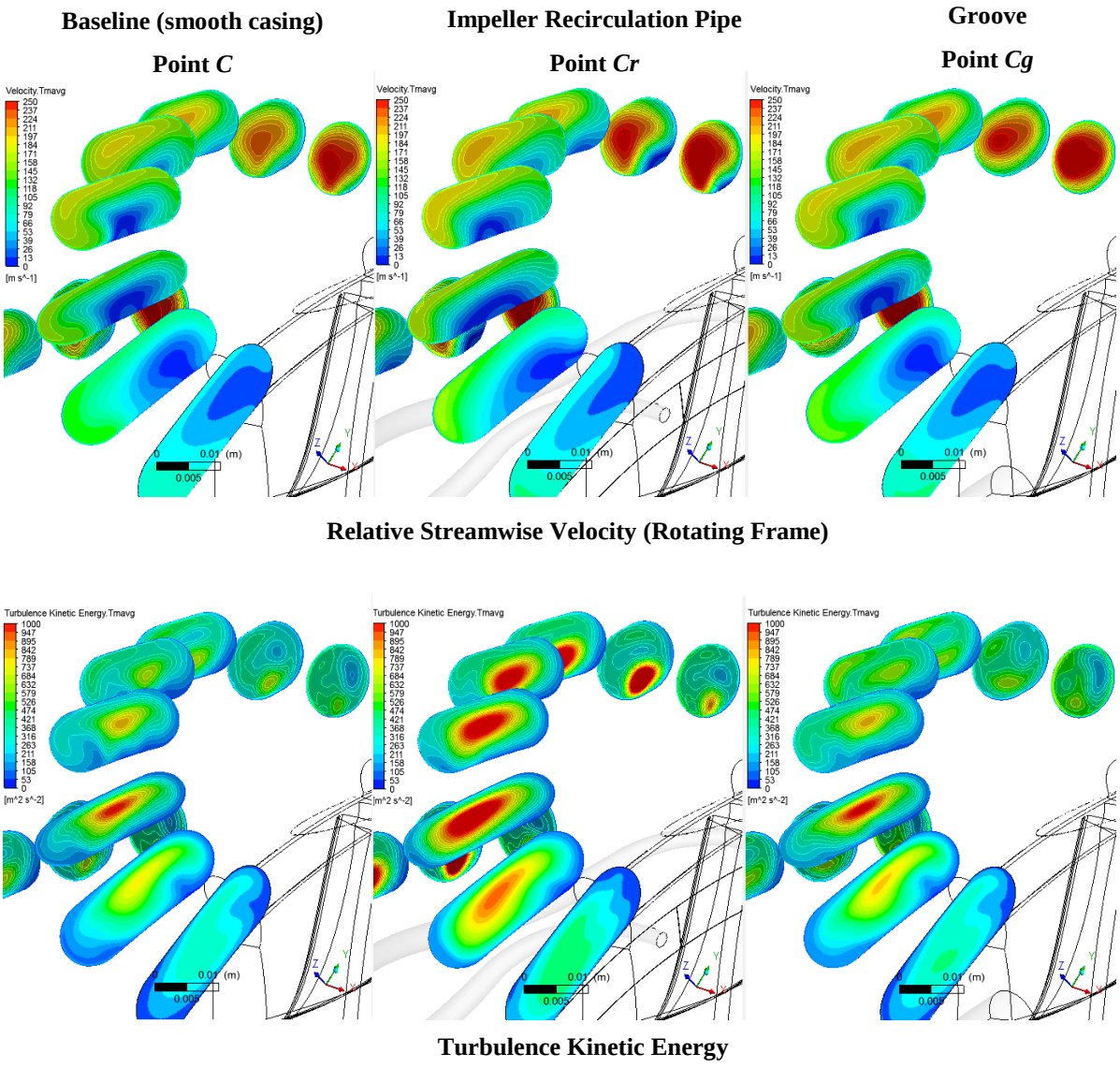

Figure 4.17: Contours of time-averaged relative streamwise velocity (top) and TKE (bottom) at planes downstream of fishtail pipe diffuser tongue for baseline (smooth casing), impeller recirculation pipe and groove at baseline design mass flow (points *C*, *Cr* and *Cg*)

CHAPTER 5 LOW-SPEED CENTRIFUGAL COMPRESSOR RESULTS

5.1 Stalling Component

Figure 5.1 shows the (time-averaged) speedlines from simulations of the baseline low-speed centrifugal compressor stage (impeller-diffuser) and the stand-alone impeller, with points *A* and *Ai* being the last stable (stall) points for the stage and impeller configurations, respectively. For the stage, points *B* and *C* are, respectively, the second-to-last stable point and the design point. The dashed point labelled "*S*" is a point along the periodic stall transient for the stage.

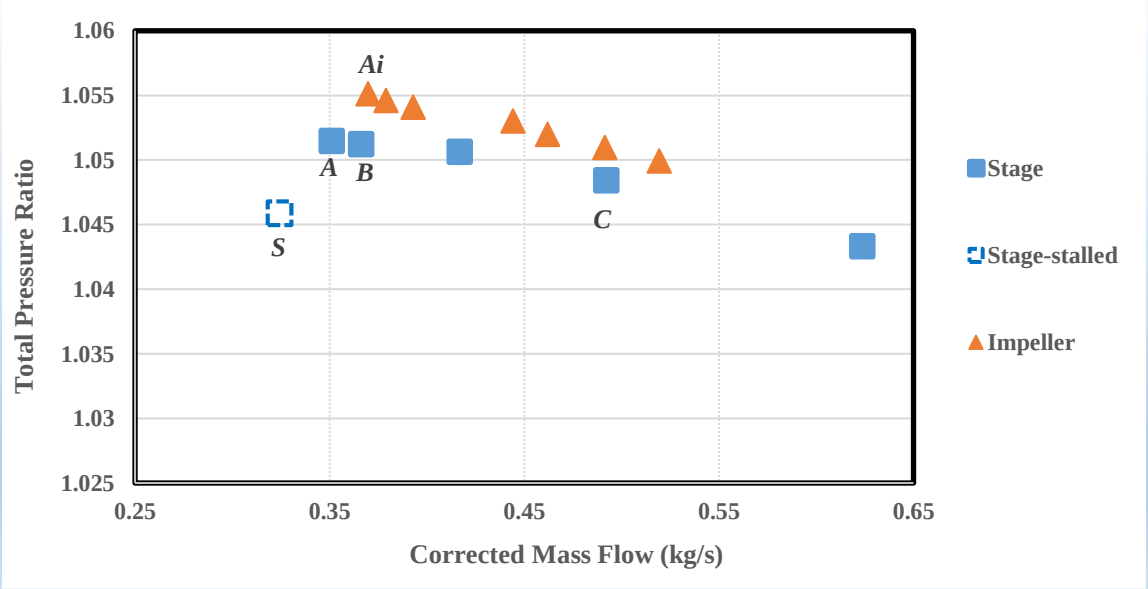

Figure 5.1: Time-averaged speedlines for low-speed centrifugal stage versus impeller

Since the impeller configuration stalls at a higher corrected mass flow rate than the stage configuration (points *Ai* versus *A* in Figure 5.1), it can be concluded that the impeller is the source of stall for the low-speed baseline centrifugal compressor stage. It can also be inferred that the presence of the diffuser is actually helping to stabilize the impeller (as will be discussed further in Section 5.2).

5.2 Stall Mechanism

The flow field in the impeller will now be investigated to find the source of stall. First, one can check for stall inception in the inducer due to tip clearance flow. Figure 5.2 shows the time-averaged static entropy contours at the impeller blade tip for the stage stall point (point *A*) to assess the leading edge tip clearance flow spillage criterion that had been shown to apply to some axial, mixed-flow and centrifugal compressors. The contours in Figure 5.2 show that the incoming/tip clearance interface has already moved upstream of the impeller leading edge at the stall point (i.e. leading edge spillage has already occurred), indicating that stall is not caused by tip clearance flow in the inducer.

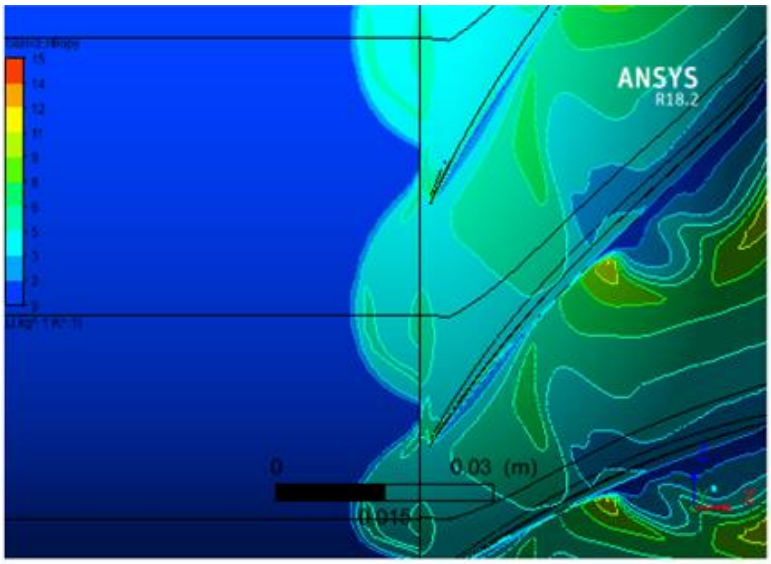

Figure 5.2: Time-averaged static entropy contours at impeller tip at stall point (point *A*) for low-speed centrifugal stage

Next, the investigation moves to the exducer. Figures 5.3 and 5.4 plots the contours of the time-averaged wall shear and the relative (rotating frame) streamlines on the impeller blade suction surface for the last two stable points of the low-speed centrifugal compressor stage (points *A* and *B*) as well as the post-stall point *S* of the stage. Figure 5.3 shows a region of low wall shear formed on the impeller tip blade suction surface close to its trailing edge (highlighted by dashed oval),

which grows in size as the mass flow reduces toward stall (points *B* to *A*), and which continues to grow during the stall transient (point *S*). The surface streamlines in Figure 5.4 indicate that this region contains a zone of boundary layer separation.

Figure 5.5 plots the relative streamwise velocity contours at different planes inside the impeller for the same points as in Figure 5.4. Results show a trend in which the size of the low-velocity or separation region increases on the impeller suction surface for the planes downstream of the radial bend by moving to lower mass flow rates. A similar mechanism for stall (suction side boundary layer separation) was first discovered in the study by Eckardt *et al.* [17].

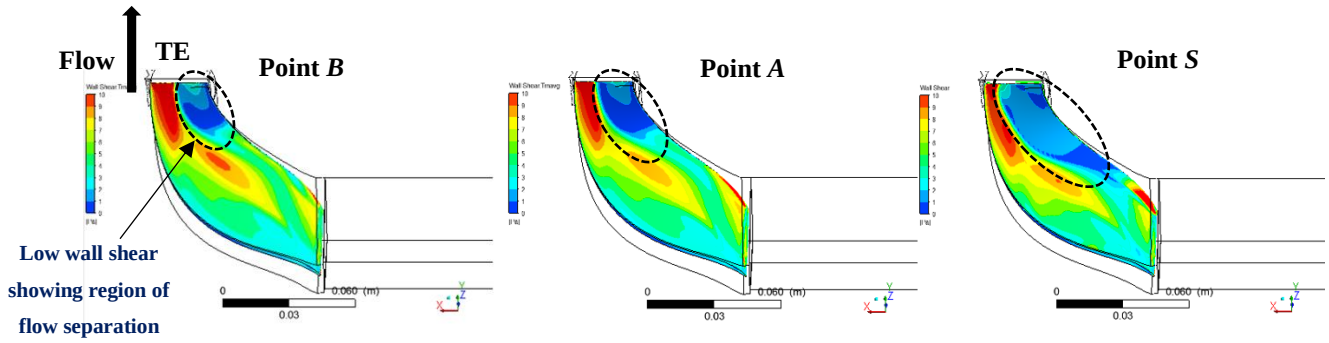

Figure 5.3: Time-averaged wall shear contours on impeller blade suction side for near-stall (points *A* and *B*) and post-stall (point *S*) of the low-speed stage

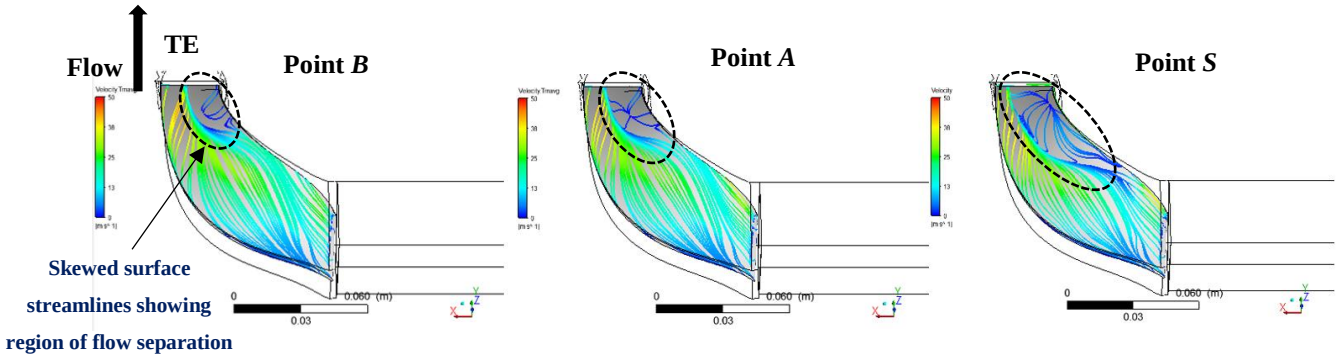

Figure 5.4: Time-averaged surface relative streamlines on impeller blade suction side for near-stall (points *A* and *B*) and post-stall (point *S*) of the low-speed stage

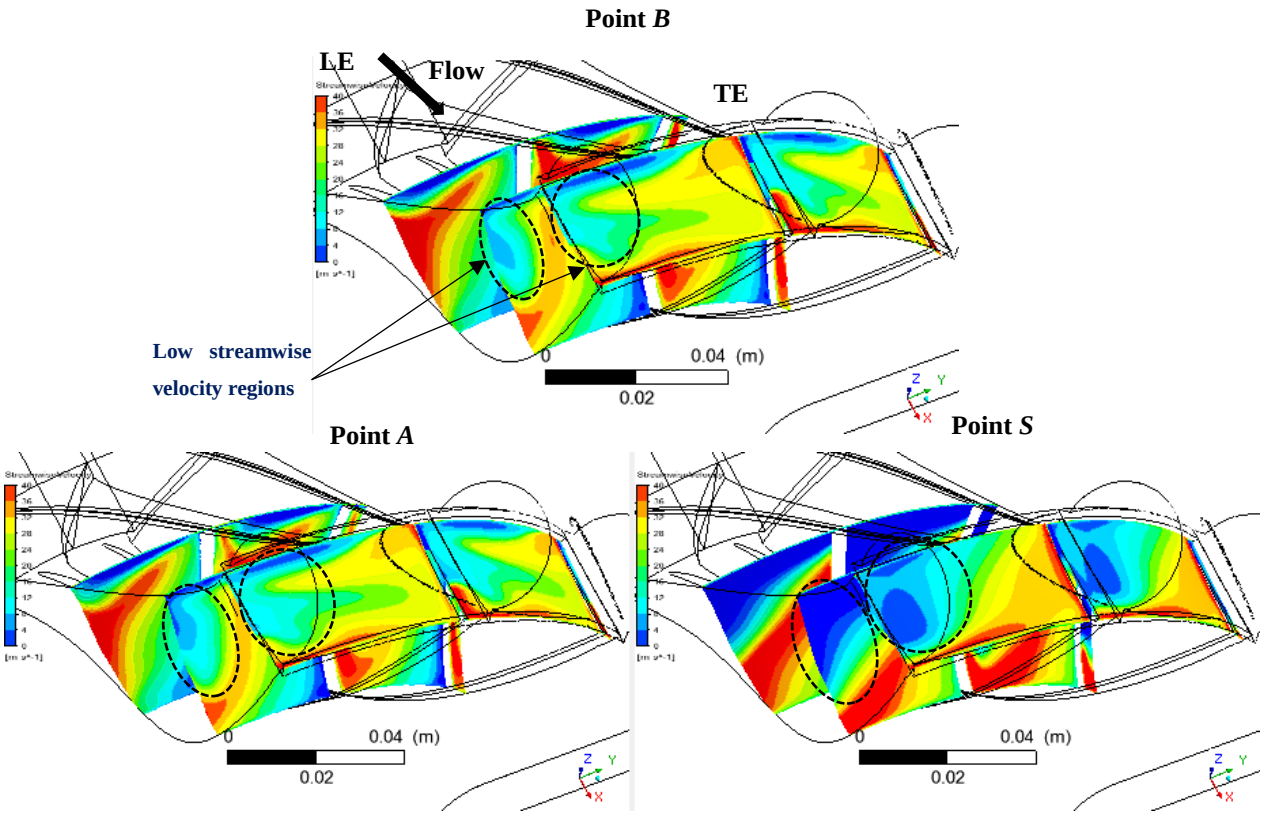

Figure 5.5: Relative streamwise velocity contours at different impeller streamwise planes for near stall (points *A* and *B*) and post stall (point *S*) of the low-speed stage

As inferred from the speedlines in Figure 5.1, the fishtail diffuser is marginally stabilizing the low-speed baseline centrifugal stage. Indeed, a comparison of the surface shear stress on the impeller suction side between impeller-alone and stage configurations at the impeller-alone stalling mass flow (points *Ai* versus *B*) in Figure 5.6 shows that the presence of fishtail diffuser in the stage configuration increases the shear stress (reduction in extent of dark blue region) in the region responsible for stall.

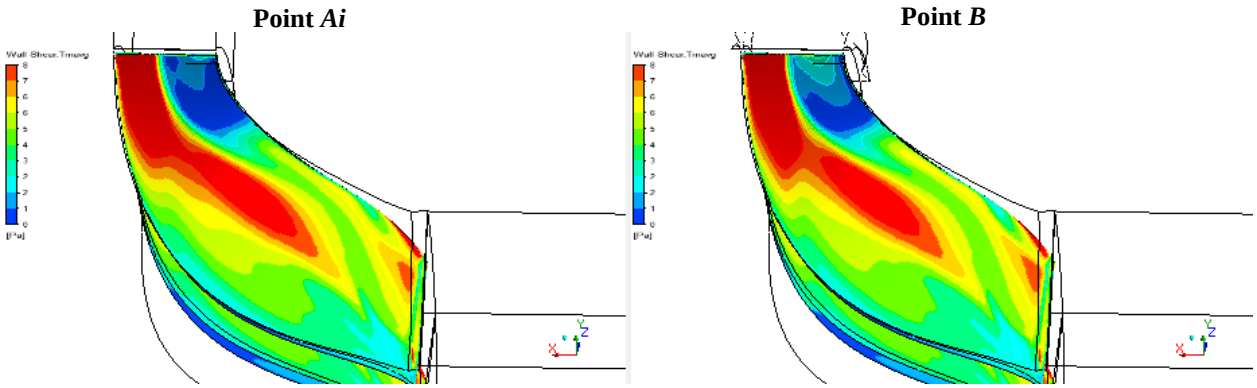

Figure 5.6: Time-averaged wall shear contours on impeller blade suction side at stand-alone impeller stalling mass flow for impeller (point *Ai*) and stage (point *B*)

5.3 Effect of Flow Control at Impeller Radial Bend

As was the case in Section 4.3, the impact of different flow control devices applied at the impeller radial bend are first assessed on an integral basis with regard to performance and stall margin improvement. Subsequently, the flow field is studied in order to elucidate the mechanism by which flow control at the radial bend delays stall for a centrifugal compressor in which the impeller exducer is the source of stall.

5.3.1 Integral Effect

Table 5.1 compares the performance parameters (stage total pressure ratio and isentropic efficiency) *at the design mass flow* and the stall margin improvement for the simulated flow control techniques at the impeller radial bend versus the baseline (smooth casing) configuration for the low-speed centrifugal compressor stage. The techniques are sorted in ascending stall margin improvement. For recirculating flow techniques with fluid extraction further downstream, the amount of recirculated mass flow (as a percentage of total mass flow) at the design mass flow is also listed. As mentioned in Chapter 3, for the diffuser-impeller recirculation pipe, two more sizes of the pipe are simulated to assess the impact of the amount of flow recirculation in stall margin.

Table 5.1: Integral effect of flow control techniques at impeller radial bend on low-speed centrifugal compressor stage

Flow Control Strategy **Low Speed**	PR_{T-T}	η (%)	*SMI* (%)	$\frac{\dot{m}_r}{\dot{m}_p}$ (%)
Baseline	1.0484	87.45	-	-
Groove	1.0481	86.35	0.34	-
Impeller Recirculation-Pipe	1.0487	87.10	4.0	1.0
Skewed Slots	1.0489	87.37	4.4	-
Diff-Impeller Recirculation-Pipe	1.0486	87.35	4.10	0.34
	1.0486	87.34	6.36	0.84
	1.0489	86.92	8.16	2.1

Contrasting the data in Table 5.1 for the low-speed compressor against those of Table 4.1 for the high-speed compressor, two observations can be made immediately. First, the trend in terms of effectiveness of the proposed flow control techniques is reversed. For the low-speed compressor, the groove provides the lowest stall margin improvement (virtually ineffective at only 0.34%) while the diffuser-impeller flow recirculation is the most effective at improving stall margin (and its effectiveness increases with recirculated mass flow). This is the opposite of the high-speed compressor. This is likely due to the difference in stall mechanism and stall delay mechanism, to be discussed in Section 5.3.2. The second observation is that the trade-off between stall margin improvement and design point efficiency is not as clear as was the case for the high-speed compressor. Indeed, the groove has both the least stall margin improvement and the highest stage efficiency penalty. Some of the reasons for this will be explored in Section 5.4.

5.3.2 Stall Delay Mechanism

Given the contrast in effectiveness between the groove and the diffuser-impeller recirculation pipe, they are selected for flow field analysis to elucidate the stall delay mechanism associated with the case where stall occurs due to blade boundary layer separation on the exducer. To identify the important points for flow field analysis, Figure 5.7 shows the speedlines for these two flow control techniques along with that of the low-speed baseline (smooth casing) centrifugal compressor. For the diffuser-impeller recirculation, the configuration with the highest flow recirculation (largest stall margin extension) is chosen. Points *Ar* and *Ag* correspond to the stall points for the configurations with the diff-impeller recirculation pipe and groove, respectively, while point *Br* and *Bg* are their operating points at around the baseline (smooth casing) stalling mass flow (that of point *A*) and *Cr* and *Cg* the corresponding operating points at the design mass flow (mass flow of point *C* in baseline configuration). Note that for the groove, the stall margin extension is marginal; resulting in the virtual overlap of points *Ag* and *Bg*.

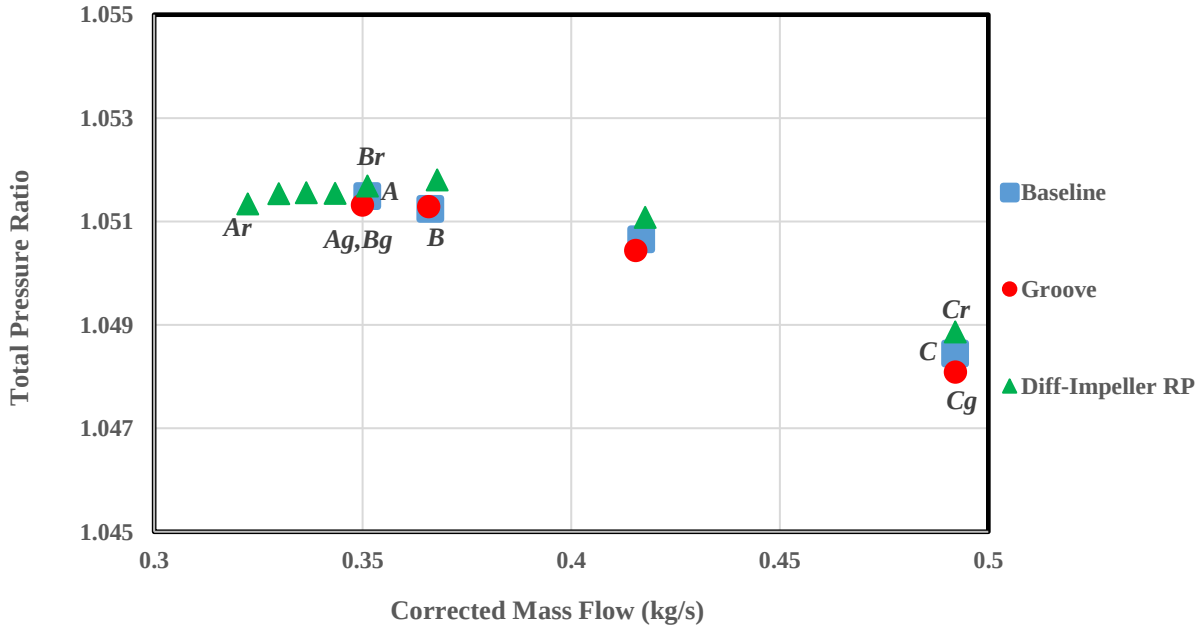

Figure 5.7: Speedlines of flow control techniques selected for flow field analysis of low-speed centrifugal compressor stage

As a first step in understanding the stall suppression mechanism, the effect of these two flow control techniques on the structure responsible for stall is assessed. Figure 5.8 shows the time-averaged wall shear contours on the impeller blade suction surface around the baseline stalling mass flow for the configurations with groove (point *Bg*) and diffuser-impeller recirculation pipe (point *Br*) versus the baseline case (point *A*). Figure 5.9 shows the surface relative streamlines for the corresponding points. The results show that the diffuser-impeller recirculation pipe completely removes the flow structure responsible for stall, namely the low-shear/boundary layer separation zone on the impeller TE tip suction side, which is consistent with its large stall margin improvement. On the other hand, the groove actually increases the overall extent of the low-shear region. However, it also increases the shear stress (reduction in extent of dark blue region in Figure 5.8) and reduces the extent of the flow separation region (reversed streamlines region in Figure 5.9), which is consistent with the very small stall margin improvement.

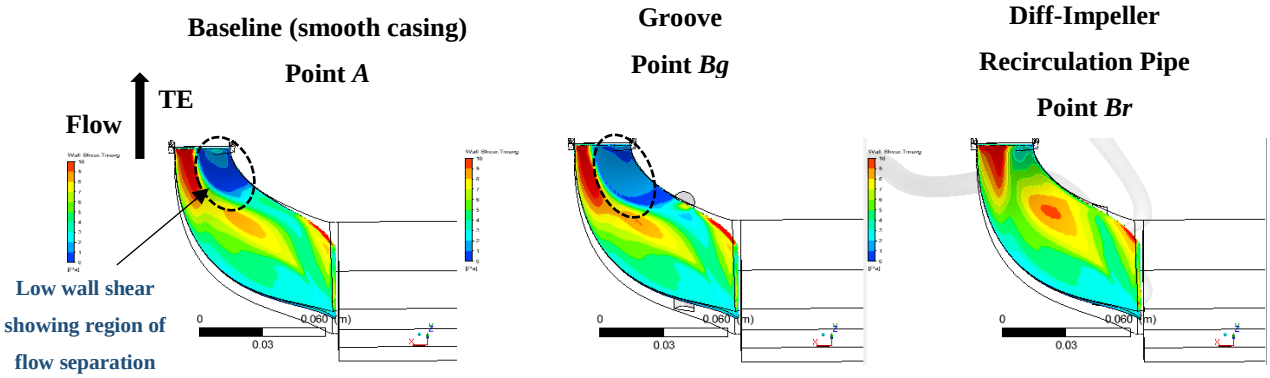

Figure 5.8: Time-averaged wall shear contour on impeller suction side around stalling mass flow of baseline low-speed stage for the baseline (smooth casing) configuration (Point *A*) versus the configuration with groove (Point *Bg*) and diffuser-impeller recirculation pipe (Point *Br*)

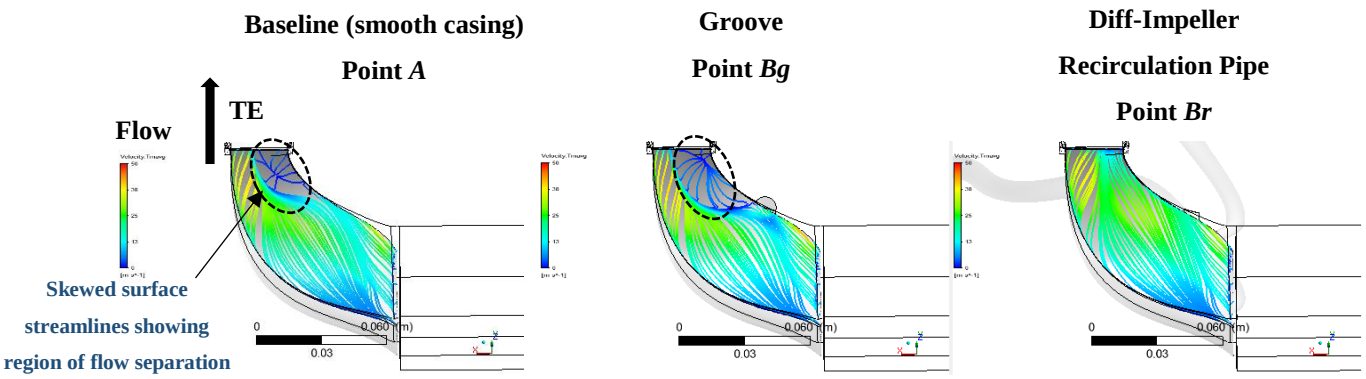

Figure 5.9: Time-averaged surface relative streamlines on impeller suction side around stalling mass flow of baseline low-speed stage for the baseline (smooth casing) configuration (Point *A*) versus the configuration with groove (Point *Bg*) and diff-impeller recirculation pipe (Point *Br*)

To explain the contrasting effect on the critical low-shear region between the two analyzed flow control techniques, Figure 5.10 plots the relative streamwise velocity contours at planes from downstream of the radial bend to the impeller trailing edge for the cases in Figures 5.8 and 5.9. The time-averaged relative streamlines emanating from the flow control device up to the exit plane are also shown. This Figure shows that relative streamwise velocity in the upper span region near the suction side on the two downstream planes (region highlighted by dashed oval) has been markedly increased in the presence of diffuser-impeller flow recirculation. Moreover, the streamlines indicate that this increase is the result of fluid injected from the diffuser-impeller recirculation, which stays in the upper span region and migrates toward the suction side as it flows toward the trailing edge, which is the very region where the boundary layer separation occurs. In contrast, the flow from the groove is injected at a much steeper angle with respect to the shroud and results in the deeper spanwise penetration ending up more in the middle to lower span on the impeller suction side near the trailing edge and not improving the streamwise velocity in the region of interest at higher span.

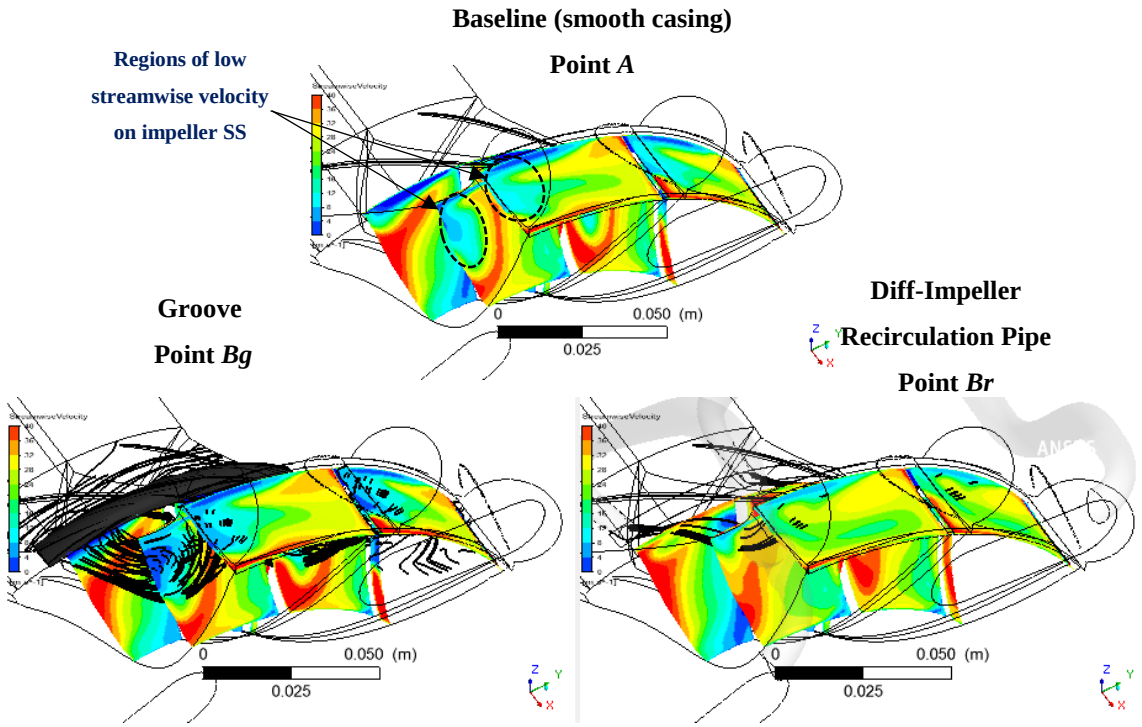

Figure 5.10: Time-averaged streamlines emanating from flow control devices and contours of time-averaged relative streamwise velocity at different impeller streamwise planes for points *A*, *Bg* and *Br*

The movement of the injection flow toward the blade suction side is common to both flow control techniques and can be explained by the imbalance between the pressure and Coriolis forces on the injected flow particles as previously illustrated by Figure 4.14 in Section 4.3.2. However, the contrasting behaviour in terms of radial penetration of the injected flow and its impact on the streamwise momentum of the passage flow can be explained through calculation of the radial and axial momentum of the injected fluid. These parameters are obtained by time-averaging the radial and axial momentum of the injection flow at the radial bend shroud (which are identified by negative radial velocity over the injection area at each time instant). The time-averaged momentum components (in $[kg{\cdot}m/s^2]$) of the injected flow are shown both numerically and graphically (in vector format) in Figure 5.11 for points *Bg* and *Br*. One can see that while the radial (close to spanwise) and axial (close to streamwise) momentums are similar for flow injected by the groove, the axial momentum is about five times greater than the radial momentum for the flow injected by recirculation pipe and ten times the value of the axial momentum of the flow injected by the groove.

This is due to the smaller angle between the injection port of the recirculation pipe and the shroud and the greater pressure difference between the suction and injection ports in the case of the recirculation pipe. For the configuration with the diffuser-impeller recirculation pipe, the result is a shallower spanwise penetration of the injected flow to reach the critical region (upper span suction side near trailing edge) and larger streamwise momentum addition (to prevent boundary layer separation in this region).

In summary, shallow spanwise penetration and high streamwise momentum of the injected flow from the flow control device (as is the case for the diffuser-impeller recirculation pipe) are the two critical features for delaying impeller exducer stall because it allows for the injected fluid to reach the upper span blade suction side near the impeller trailing edge and energize the boundary layer there to prevent its separation. By contrast, a deep spanwise penetration and low streamwise momentum of the injected flow (as is the case with the groove) means that this flow does not reach the critical region nor increase flow momentum there to suppress boundary layer separation effectively and to delay stall in this case. However, it is perfect for addressing the stall mechanism associated with flow separation in the pipe diffuser through the mechanism outlined in Section 4.3.2. This contrast explains the opposite trend in stall margin improvement from the proposed flow control techniques between the low-speed and high-speed compressors.

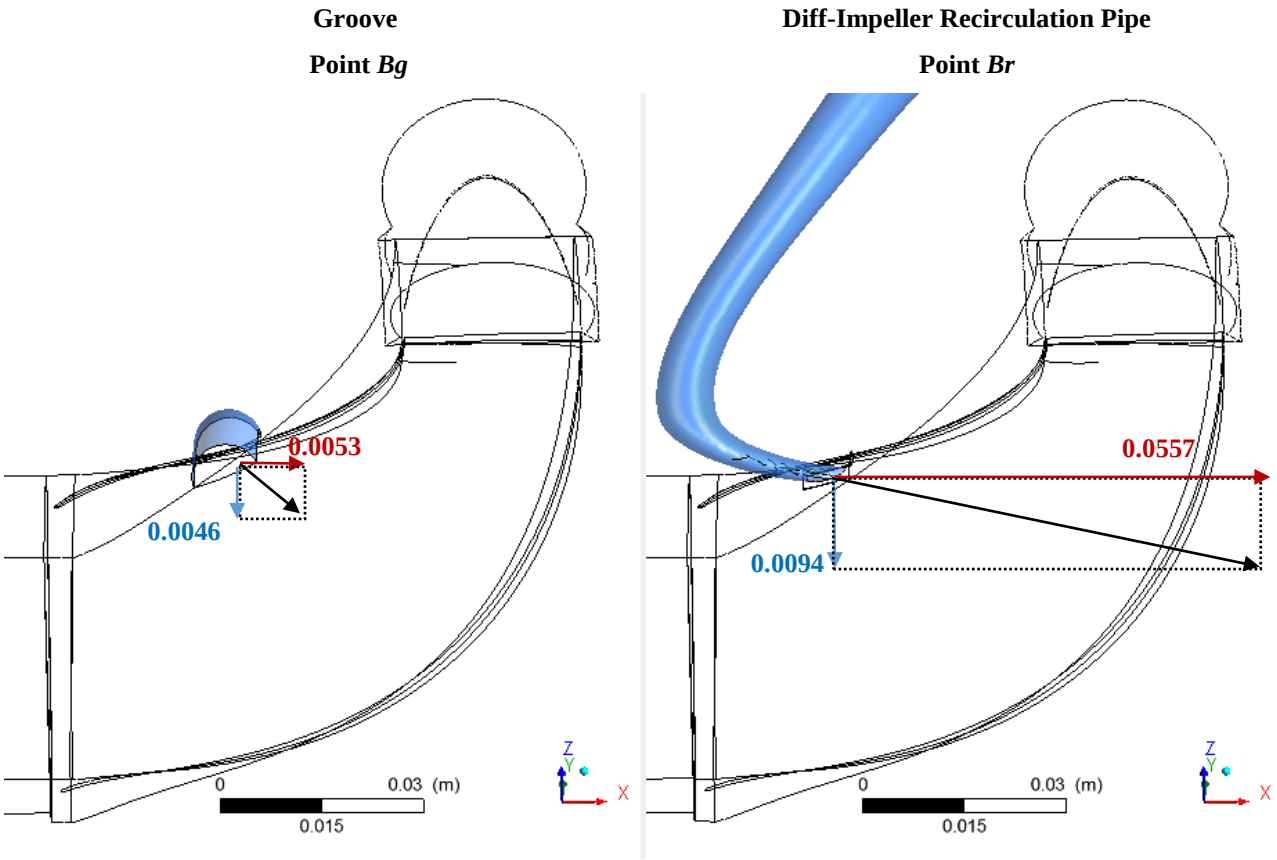

Figure 5.11: Meridional view of impeller passage showing vectors of radial and axial momentum components of flow injected by flow control devices for points *Bg* and *Br*

5.4 Flow Control Impact on Peak-Efficiency and Losses

Table 5.2 compares the isentropic efficiency at baseline (smooth casing) design mass flow for the low-speed centrifugal compressor with different flow control techniques. For the diffuser-impeller recirculation, only the configuration with the best stall margin improvement (highest recirculated mass flow) is included. The stage efficiency (η) is separated into impeller efficiency (η_i) and diffuser loss coefficient (σ) (total pressure loss non-dimensionalized by diffuser inlet dynamic head). The diffuser loss coefficient itself is split into the loss for the regions upstream (σ_u) and downstream (σ_d) of the tongue.

Table 5.2: Efficiency and Loss at design mass flow at low-speed

Flow Control Strategy **Low Speed**	η_i **(%)**	**Diffuser Loss Coefficient**			η **(%)**
		σ	σ_u	σ_d	
Baseline (point *C*)	95.09	0.156	0.068	0.088	87.45
Groove (point *Cg*)	93.61	0.187	0.102	0.084	86.35
Impeller Recirculation-Pipe	94.50	0.147	0.058	0.089	87.10
Skewed Slots	94.77	0.144	0.054	0.090	87.37
Diff-Impeller Recirculation-Pipe (point *Cr*)	93.89	0.142	0.053	0.089	86.92

The results indicate that the simulated flow controls all result in loss in impeller efficiency, only the groove increases loss in the diffuser, and mostly before the tongue. The grooves also stands out in having the largest impeller effciency penalty. A closer look at the flow field can reveal the reasons behind these observations.

The first flow field analysis aims to the sources of loss in the impeller due to flow control. Figure 5.12 overlays the time-averaged relative streamlines associated with the flow injected from the groove and diffuser-impeller flow reciculation pipe over corresponding contours of (TKE) at streamwise planes from just downstream of the radial bend to the impeller exit at the baseline design mass flow. One can observe that this is a jet-in-cross-flow phenomenon, which by nature generates mixing and shear losses, as shown with regions of high TKE around the streamlines. Moreover, for the groove whose injection penetrates deeper toward the hub (due to low streamwise momentum relative to spanwise momentum), the amplitude and extent of the high-TKE region is higher from the injection location (high mixing loss between two streams with large directionality

difference) all the way to the impeller exit (high turbulent shear loss from large streamwise velocity gradient). By contrast, the streamlines emanating from the diffuser-impeller reciculation pipe has shallower penetration (larger streamwise mometum realtive to spanwise). This factor results in lower mixing losses (smaller angle difference between two streams) and lower shear losses (lower streamwise velocity gradient), as evidenced by the smaller amplitude and extent of the high-TKE region relative to the groove. This explains the lower impeller efficiency penalty associated with the diffuser-impeller reciculation pipe compared to the groove. The diffrence would likely be even higher, were it not for the viscous losses associated with the long recicrculation pipe (which results in lower momentum of injected flow than would have been the case if the pipe was inviscid).

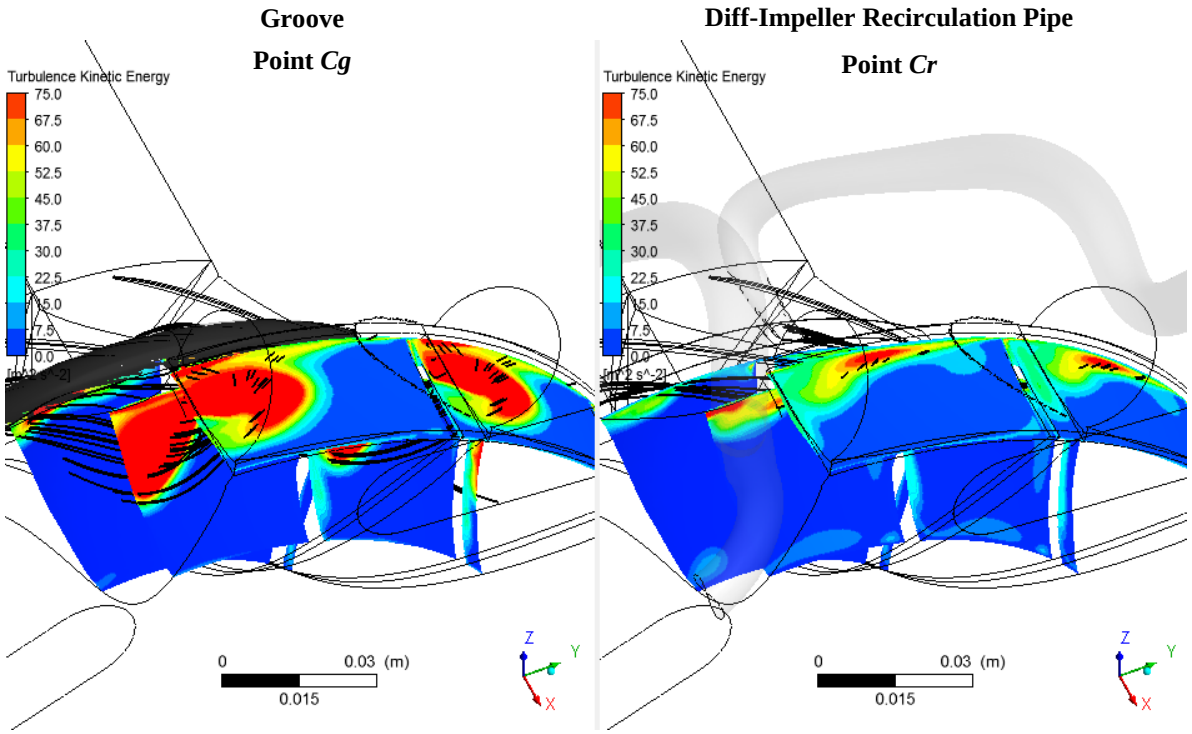

Figure 5.12: Time-averaged streamlines emanating from flow control devices and contours of time-averaged turbulence kinetic energy (TKE) at planes downstream of radial bend for groove and diffuser-impeller recirculation pipe at baseline design mass flow (points *Cg* and *Cr*)

Regarding the losses in the fishtail pipe diffuser, the data in Table 5.2 indicate that, with the exception of the groove, all simulated flow control techniques decrease the losses in the fishtail

diffuser upstream of the tongue (accounting for approximately 40% of the total diffuser loss), while losses downstream of the tongue remain more or less the same. For the groove, the losses upstream of the tongue are almost doubled those of the baseline and the other flow control techniques and account for the higher total diffuser loss. To explain this phenomenon, Figure 5.13 shows a comparative analsysis of the flow field in the diffuser close to the tongue between the baseline (smooth casing) configuration and those with the groove and the diffuser-impeller reciculation pipe at the design mass flow in terms of velocity gradient and TKE. The zones highlighted by the dashed ovals indicate that the flow redistribution in the first part of the diffuser from flow control causes a significant increase in the velocity gradient only for the groove configuration, which results in larger shear losses, as indicated by higher TKE than in the baseline case. The opposite is true for the diffuser-impeller recirculation pipe (and the other two effective flow control devices) with smaller velocity gradient and lower shear losses (lower TKE).

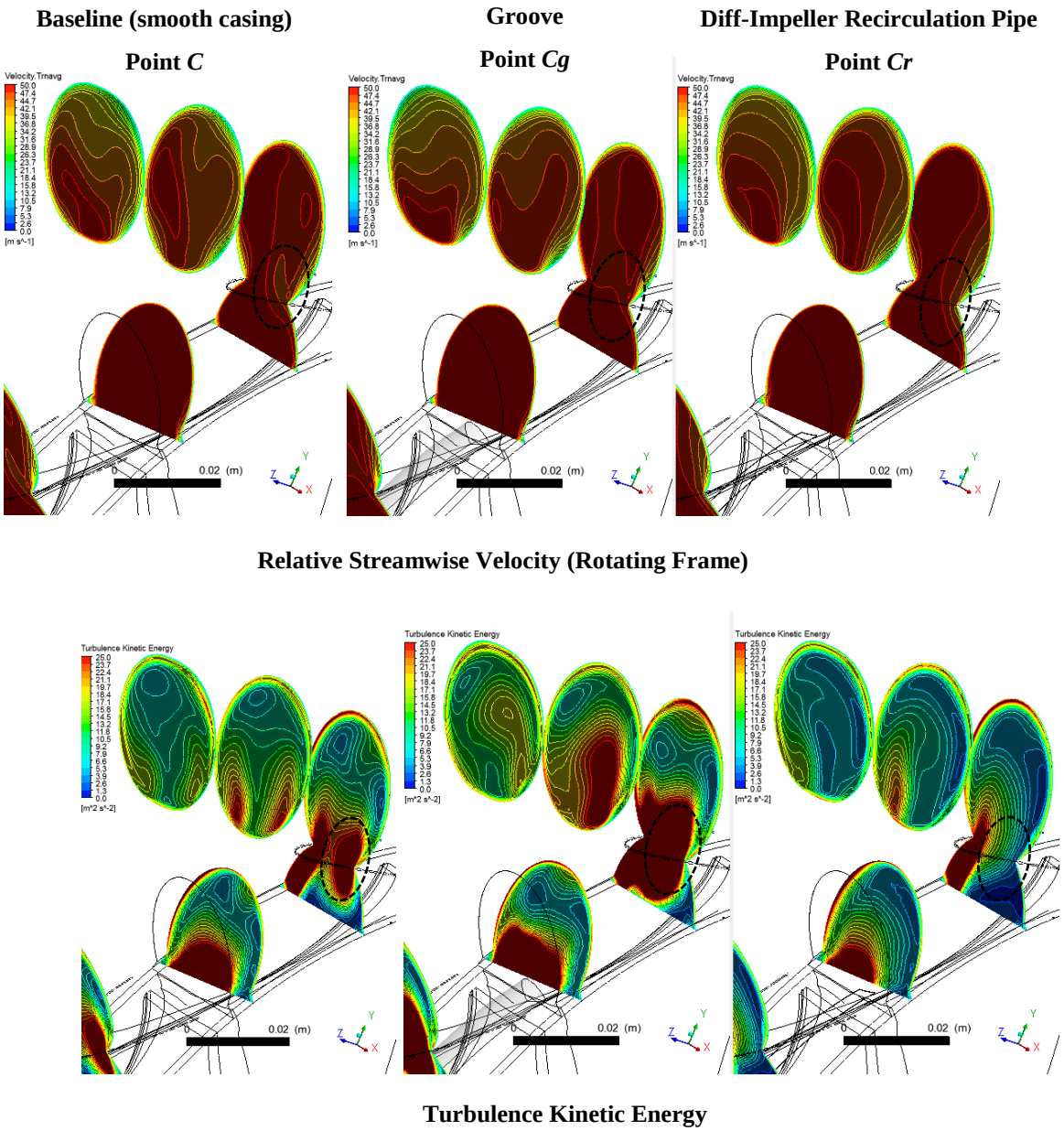

Figure 5.13: Contours of time-averaged relative streamwise velocity (top) and TKE (bottom) at planes near tongue for baseline (smooth casing), groove and diff-impeller recirculation pipe at baseline design mass flow (points *C*, *Cg* and *Cr*)

CHAPTER 6 CONCLUSIONS (AND RECOMMENDATIONS)

An assessment of passive flow control placed on the impeller shroud at the radial bend for stall margin improvement was carried out for two centrifugal compressor stages with fishtail pipe diffusers, one operating in the transonic regime with diffuser stall and the other in the low subsonic regime with impeller exducer stall. Four candidate flow control techniques: circumferential grooves, slots, impeller recirculation pipe and diffuser-impeller recirculation pipe were considered. RANS CFD simulations were performed on each compressor without (baseline) and with each of the four flow control techniques to confirm the stalling component and assess the stall mechanism, to elucidate the mechanism by which effective passive flow control from the radial bend delays stall, and to investigate the sources of efficiency penalty at design mass flow associated with this flow control strategy. The flow physics gained from this pioneering investigation into passive flow control at the impeller radial bend can be used to refine the proposed passive flow control techniques and devise new flow control techniques to maximize stall margin extension while minimizing efficiency penalty for this type of compressor. The Section 6.1 summarizes the main conclusions while Section 6.2 proposes follow-up works to take this research further toward commercial application.

6.1 Conclusions

6.1.1 Compressor with Diffuser Stall

The findings for a centrifugal compressor with fishtail pipe diffuser exhibiting diffuser stall, such as the high-speed centrifugal compressor studied in this research, are as follows:

- Diffuser stall is caused by flow separation on the radially outer wall of the fishtail diffuser pipe.
- Passive flow control at the impeller radial bend can be very effective in extending the stall margin by suppressing the separation region in the diffuser. This is best done by deep spanwise

flow injection with low relative streamwise momentum from the flow control device at the radial bend. Due to the its lower relative streamwise momentum compared to that of the main passage flow, the injected flow experiences a lower Coriolis force and migrates in the direction of rotation ending up on the lower span region not far from the blade suction side near the impeller trailing edge. The result is a reduced relative streamwise velocity and higher velocity in the stationary frame for the flow in this region, which convects to the location in the fishtail pipe diffuser where flow separation leads to stall. The increased absolute flow velocity in the critical region of the diffuser provided by the injected flow at the radial bend though the path described above suppresses flow separation and thus stall. Among the proposed stall control devices, the circumferential groove most effectively implements this stall suppressing mechanism.

- The efficiency penalty associated with passive flow control at the radial bend is the result of additional losses incurred in the impeller and the diffuser. The additional losses in the impeller stems from the jet-in-cross-flow phenomenon associated with the flow injection which produces mixing losses near the injection location and shear losses downstream, due to the difference in streamwise velocity between the injected flow and the mainstream flow. As such deeper spanwise injection with low streamwise momentum, such as is the case with the groove, would incur a greater efficiency penalty in the impeller. In the diffuser, shear losses can increase or decrease depending on whether the flow redictribution increase or decrease veloity gradients. For flow recirculation techniques, the viscous losses associated with wetted surfaces in the long recicrculation pipe contribute to the losses in the impeller through the lower momentum of the injected flow than for the ideal case of a pipe with inviscid walls.

6.1.2 Compressor with Impeller Exducer Stall

The findings for a centrifugal compressor with fishtail diffuser exhibiting impeller exducer stall, such as the low-speed centrifugal compressor studied in this research, are as follows:

- Impeller exducer stall is associated with suction side blade boundary layer separation in the upper span region of the impeller exit.
- Effective passive flow control increases the streamwise velocity in this region to suppress boundary layer separation and delay stall to a lower mass flow. This is done by shallow spanwise flow injection (with high relative streamwise momentum) from the flow control device at the radial bend. The shallow penetration of the injected flow combined with its migration in the direction of rotation (from weak Coriolis force) and relatively higher streamwise momentum ensures that this flow will reach the impeller blade suction side tip region near the trailing edge to energize the boundary layer and suppress its separation. For the passive flow techniques studied, this is best done by diffuser-to-impeller recirculation pipe due to the high injection momentum form large pressure difference and shallow injection angle.
- The sources of additional losses leading to efficiency penalty from flow controls are essentially the same as described previously for the compressor with diffuser stall: mixing and shear losses in the impeller from the jet-in-cross flow situation and additional or reduced shear losses in the diffuser from flow redistribution. However, since the impeller exducer stall is best suppressed though shallow spanwise injection with high streamwise velocity, the successful flow control techniques in this case tend to have a reduced efficiency penalty, in contrast to those that are successful for suppressing diffuser stall.

6.2 Future Work

1) Optimize the proposed flow control techniques in order to improve their effectiveness in stall delay and reduce efficiency penalty. Examples include:
   - moving the suction port of the diffuser-impeller recirculation pipe to the location in the fishtail pipe diffuser where the critical flow separation leading to stall is initiated
   - moving the flow control device downstream of the radial bend to reduce spanwise penetration for more effective suppression of impeller exducer stall and reduced impeller efficiency penalty

2) Devise new flow control techniques for diffuser stall and impeller stall to maximize stall margin extension while reducing the penalty in efficiency
3) Assess the effectiveness of passive flow control at the impeller radial bend for centrifugal compressor with stall initiated in vaned and channel diffusers
4) Experimentally validate flow control techniques in compressor test rigs

REFERENCES

[1] Lutte, R. K., ICAO, 2015, "Air navigation report," International Civil Aviation Organization, Montreal, Canada.

[2] Bousquet, Y., Binder, N., Dufour, G., Carbonneau, X., Roumeas, M., and Trebinjac, I., 2016, "Numerical simulation of stall inception mechanisms in a centrifugal compressor with vaned diffuser," ASME Journal of Turbomachinery, Vol. 138, No. 12, p. 121005, 9 pages.

[3] Campbel, J., 1992, "Gas conditioning and processing, Volume 2: The equipment modules," Campbell Petroleum Series, Norman, Oklahoma.

[4] Cumpsty, N. A., 1989, Compressor aerodynamics, Longman scientific & technical.

[5] Anish, S., Sitaram, N., and Kim, H., 2014, "A numerical study of the unsteady interaction effects on diffuser performance in a centrifugal compressor," ASME Journal of Turbomachinery, Vol. 136, No. 1, p. 011012, 10 pages.

[6] Deniz, S., Greitzer, E. M., and Cumpsty, N. A., 1998, "Effects of inlet flow field conditions on the performance of centrifugal compressor diffusers: Part 2—straight-channel diffuser," Proc. ASME 1998 International Gas Turbine and Aeroengine Congress and Exhibition, pp. V001T001A112, 8 pages.

[7] Han, G., Lu, X., Zhao, S., Yang, C., and Zhu, J., 2014, "Parametric studies of pipe diffuser on performance of a highly loaded centrifugal compressor," Journal of Engineering for Gas Turbines and Power, Vol. 136, No. 12, p. 122604, 10 pages.

[8] Boyce, M. P., 1993, "Principles of operation and performance estimation of centrifugal compressors," Proc. of Turbomachinery Symposium, pp. 161-177.

[9] Kenny, D. P., 1968, "Novel low-cost diffuser for high-performance centrifugal compressors," United Aircraft of Canada Limited, Ville Jacques Cartier, P. Q., Canada. Vol. 91, No. 1, pp. 37-46.

[10] Bryans, A. C., 1986, "Diffuser for a centrifugal compressor," US patent number 4,576,550, page 8.

[11] Bourgeois, J. A., Martinuzzi, R. J., Savory, E., Zhang, C., and Roberts, D. A., 2011, "Assessment of turbulence model predictions for an aero-engine centrifugal compressor,"ASME Journal of Turbomachinery, Vol. 133, No. 1, p. 011025, 15 pages.

[12] Han, G., Lu, X., Zhang, Y., Zhao, S., Yang, C., and Zhu, J., 2016, "Study of geometric parameter influence on fishtail pipe diffuser performance," Proc. ASME Turbo Expo: Turbomachinery Technical Conference and Exposition, pp. V02DT42A028, 9 pages.

[13] Koyyalamudi, V., and Nagpurwala, Q. H., 2016, "Stall margin improvement in a centrifugal compressor through inducer casing treatment," International Journal of Rotating Machinery, Article ID 2371524, 19 pages.

[14] Chen, H., and Lei, V.-M., 2013, "Casing treatment and inlet swirl of centrifugal compressors," ASME Journal of Turbomachinery, Vol. 135, No. 4, p. 041010, 8 pages.

[15] Wang, T., Xu, W., Gu, C., and Xiao, J., 2010, "A new type of self-adaptive casing treatment for a centrifugal compressor," Proc. ASME Turbo Expo: Power for Land, Sea, and Air, pp. 2065-2074.

[16] Zheng, X., Zhang, Y., Yang, M., Bamba, T., and Tamaki, H., 2013, "Stability improvement of high-pressure-ratio turbocharger centrifugal compressor by asymmetrical flow control—Part II: Nonaxisymmetrical self-recirculation casing treatment," ASME Journal of Turbomachinery, Vol. 135, No. 2, p. 021007, 8 pages.

[17] Eckardt, D., 1980, "Flow field analysis of radial and backswept centrifugal compressor impellers. Part 1-Flow measurements using a laser velocimeter," Performance Prediction of Centrifugal Pumps and Compressors, Proc. ASME, pp. 77-86.

[18] Japikse, D., 1988, Centrifugal compressor design and performance: Course Held at Wilder, Vermont, 19.9.-23.9. 1988, Concepts ETI.

[19] Ibaraki, S., Matsuo, T., Kuma, H., Sumida, K., and Suita, T., 2003, "Aerodynamics of a transonic centrifugal compressor impeller," ASME Journal of Turbomachinery, Vol. 125, No. 2, pp. 346-351.

[20] Kaneko, M., and Tsujita, H., 2015, "Numerical investigation of influence of tip leakage flow on secondary flow in transonic centrifugal compressor at design condition," Journal of Thermal Science, Vol. 24, No. 2, pp. 117-122.

[21] Ashrafi, F., Michaud, M., and Vo, H. D., 2016, "Delay of rotating stall in compressors using plasma actuators," ASME Journal of Turbomachinery, Vol. 138, No. 9, p. 091009, 12 pages.

[22] Vrana, J. C., 1967, "Diffuser for centrifugal compressor," US Patent 3,333,762.

[23] Grates, D. R., Jeschke, P., and Niehuis, R., 2014, "Numerical investigation of the unsteady Flow inside a centrifugal compressor stage with pipe diffuser," ASME Journal of Turbomachinery, Vol. 136, No. 3, p. 031012, 14 pages.

[24] Zachau, U., Niehuis, R., Hoenen, H., and Wisler, D. C., 2009, "Experimental investigation of the flow in the pipe diffuser of a centrifugal compressor stage under selected parameter variations," Proc. ASME Turbo Expo: Power for Land, Sea, and Air, pp. 1213-1223.

[25] Moore, F., 1984, "A theory of rotating stall of multistage axial compressors: part I—Small disturbances." Journal of Engineering for Gas Turbines and Power, Vol. 106, No. 2, pp. 313-320.

[26] Moore, F. K., and Greitzer, E. M., 1986, "A theory of post-stall transients in axial compression systems: Part I—Development of equations." Journal of Engineering for Gas Turbines and Power, Vol. 108, No. 1, pp. 68-76.

[27] Day, I., 1993, "Stall inception in axial flow compressors." ASME Journal of Turbomachinery, Vol. 115, No. 1, pp. 1-9.

[28] Camp, T., and Day, I., 1997, A study of spike and modal stall phenomena in a low-speed axial compressor, American Society of Mechanical Engineers.

[29] Vo, H. D., Tan, C. S., and Greitzer, E. M., 2005, "Criteria for spike initiated rotating stall," Proc. ASME Turbo Expo: Power for Land, Sea, and Air, pp. 155-165.

[30] Vo, H. D., Tan, C. S., and Greitzer, E. M., 2008, "Criteria for spike initiated rotating stall," ASME Journal of turbomachinery, Vol. 130, No. 1, p. 011023, 9 pages.

[31] Deppe, A., Saathoff, H., and Stark, U., "Spike-type stall inception in axial-flow compressors," Proc. of 6th Conference on Turbomachinery, Fluid Dynamics and Thermodynamics, Lille, France. 11 pages.

[32] Hah, C., and Krain, H., 1999, "Analysis of transonic flow fields inside a high pressure ratio centrifugal compressor at design and off design conditions," Proc. ASME 1999 International Gas Turbine and Aeroengine Congress and Exhibition, pp. V001T003A069, 15 pages.

[33] Cameron, J. D., and Morris, S. C., 2013, "Analysis of axial compressor stall inception using unsteady casing pressure measurements," ASME Journal of Turbomachinery, Vol. 135, No. 2, p. 021036, 12 pages.

[34] Djeghri, N., Vo, H. D., and Yu, H., 2015, "Parametric study for lossless casing treatment on a mixed-flow compressor rotor," Proc. ASME Turbo Expo : Power for Land, Sea and Air, Montreal, Canada. pp. V02AT37A025, 8 pages.

[35] Sitaram, N., and Swamy, S., 2012, "Performance improvement of a centrifugal compressor by passive means," International Journal of Rotating Machinery, Vol. 2012, ID 727259, 9 pages.

[36] Skoch, G. J., "Experimental investigation of centrifugal compressor stabilization techniques," Proc. ASME Turbo Expo: Power for Land, Sea, and Air, pp. 765-776.

[37] Hiradate, K., Kobayashi, H., Sugimura, K., Ito, T., and Nishida, H., 2015, "Proposal and experimental verification of design guidelines for centrifugal compressor impellers with curvilinear element blades to improve compressor performance," ASME Journal of Turbomachinery, Vol. 137, No. 5, p. 051008, 11 pages.

[38] Shibata, T., Yagi, M., Nishida, H., Kobayashi, H., and Tanaka, M., 2011, "Performance improvement of a centrifugal compressor stage by increasing degree of reaction and optimizing blade loading of a 3D impeller," ASME Journal of Turbomachinery, Vol. 133, No. 2, p. 021004, 8 pages.

[39] Ganesh, C. S., Nagpurwala, Q., and Dixit, C., 2010, "Effect of leading edge sweep on the performance of a centrifugal compressor impeller," SASTech-Technical Journal of RUAS, Vol. 9, No. 2, pp. 55-62.

[40] Müller, M. W., Schiffer, H.-P., and Hah, C., 2007, "Effect of circumferential grooves on the aerodynamic performance of an axial single-stage transonic compressor," Proc. ASME Turbo Expo: Power for Land, Sea, and Air, pp. 115-124.

[41] Guinet, C., Streit, J. A., Kau, H.-P., and Gümmer, V., 2014, "Tip gap variation on a transonic rotor in the presence of tip blowing," Proc. ASME Turbo Expo: Power for Land, Sea, and Air, pp. V02AT37A002, 10 pages.

[42] Wilke, I., and Kau, H.-P., 2004, "A numerical investigation of the flow mechanisms in a high pressure compressor front stage with axial slots," ASME Journal of Turbomachinery, Vol. 126, No. 3, pp. 339-349.

[43] Vo, H. D., and Trépanier, J.-Y., 2016, "Undergraduate project in compressor rig design, fabrication, and testing for complete engineering training," Journal of Engineering for Gas Turbines and Power, Vol. 138, No. 5, p. 052604, 13 pages.

[44] Guide, Ansys CFX Modeling Guide, 2012, "Release 14.5," Ansys Inc.

[45] Dumas, M., Vo, H. D., and Yu, H., "Post-surge load prediction for multi-stage compressors via CFD simulations," Proc. ASME Turbo Expo: Power for Land, Sea, and Air, pp. V02BT39A022, 12 pages.

[46] Wood, J. R., Hathaway, M. D., and Okiishi, T. H., 2000, "Recommendations for achieving accurate numerical simulation of tip clearance flows in transonic compressor rotors.", ASME Journal of Turbomachinery, Vol. 122, No. 4, pp. 733-742.

[47] Takata, H., and Tsukuda, Y., 1977, "Stall margin improvement by casing treatment—its mechanism and effectiveness.", Vol. 99, No. 1, pp. 121-133.

[48] Bennett, I., Tourlidakis, A., and Elder, R., 1998, "Detailed measurements within a selection of pipe diffusers for centrifugal compressors," Proc. ASME 1998 International Gas Turbine and Aeroengine Congress and Exhibition, pp. V001T001A028, 8 pages.

[49] Han, G., Lu, X., Zhang, Y., Zhao, S., and Zhu, J., 2015, "Study of a highly loaded centrifugal compressor with pipe diffuser at design and off-design operating conditions," Proc. ASME Turbo Expo 2015: Turbine Technical Conference and Exposition, pp. V02CT42A030, 12 pages.

[50] Dolan, F. X., and Runstadler Jr, P. W., 1973, "Pressure recovery performance of conical diffusers at high subsonic mach numbers," NASA Contractor Report 2299.

APPENDIX A DESIGN GUIDELINES FOR EFFICIENT FISHTAIL PIPE DIFFUSER

A few studies for the efficient design of pipe diffusers have been published. Blair *et al.* [5] looked into the effect of pipe throat blockage, inlet Mach number, number of pipes and rate of area change. Bennett *et al.* [48] performed a detailed experimental measurements on different pipe diffuser with different throat shapes (circular or oval). They also investigated the impact of the number of pipes. In one of the first efforts to simultaneously investigate the effect of multiple geometrical parameters on pipe diffusers' performance, Han *et al.* [7] varied four different parameters on a highly loaded centrifugal compressor stage, namely: diffuser inlet-to-impeller exit radius ratio, throat length, divergence angle and throat area. A change in any of these parameter can alleviate the diffuser inlet flow distortion and reduce the possibility of flow separation in passages, which can lead to an improved performance for a highly loaded stage. In a later numerical study by Han *et al.* in 2015 [49], the performance of an optimized pipe diffuser was compared with a wedge diffuser.

However, the only published study on fishtail pipe diffuser design was that of Han *et al.* [12] in 2016 in which they numerically investigated the effect of three design parameters namely cone length, streamwise area distribution and centerline shape for a centrifugal compressor stage with a 8.3:1 pressure ratio. The cross section is circular at the throat and remains circular across the straight centerline up to the end of the cone length. Then the cross section becomes oblong like an oval, which is characterized by semi-circular ends attached to straight lines. There is a progressive increase in the long axis of the oval while the semi-circular radius decreases along the centerline from the end of the cone to the diffuser outlet, therefore to make the area increase, the long axis should enlarge faster. Figure A.1 shows the *fishtail* diffuser design from in this reference. Note that CD is the cone length.

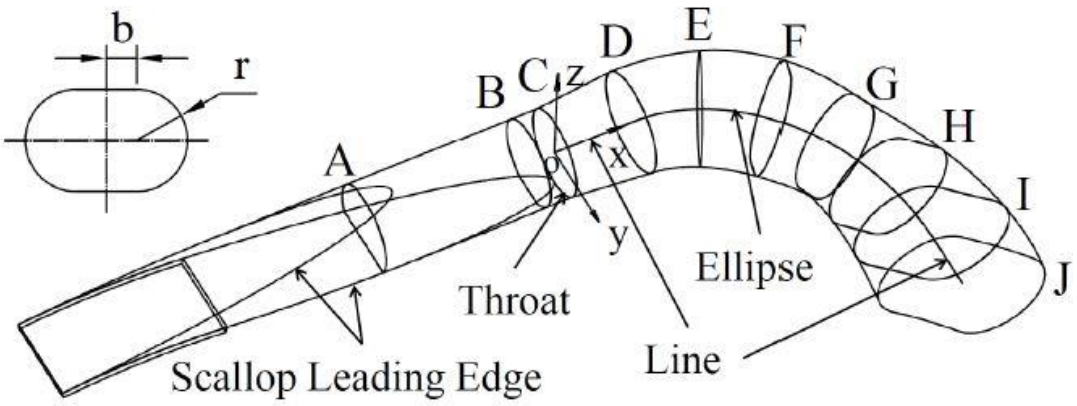

Figure A.1: Sketch of fishtail diffuser [12]

The first parameter changed was the cone length with a linear area increase along the centerline and a centerline with a quarter-ellipse shape with long to short axis ratio of 0.75. As can be seen in the Mach contours for three different cone lengths in Figure A.2, the increase in cone length reduced the flow separation on the pressure side and improved the stage performance. However, there is an optimum value for cone length beyond which flow reversal occurs on the suction side near the diffuser exit due to stronger secondary flows in turning process, which penalizes the performance. The optimum length is ‘Cone2’.

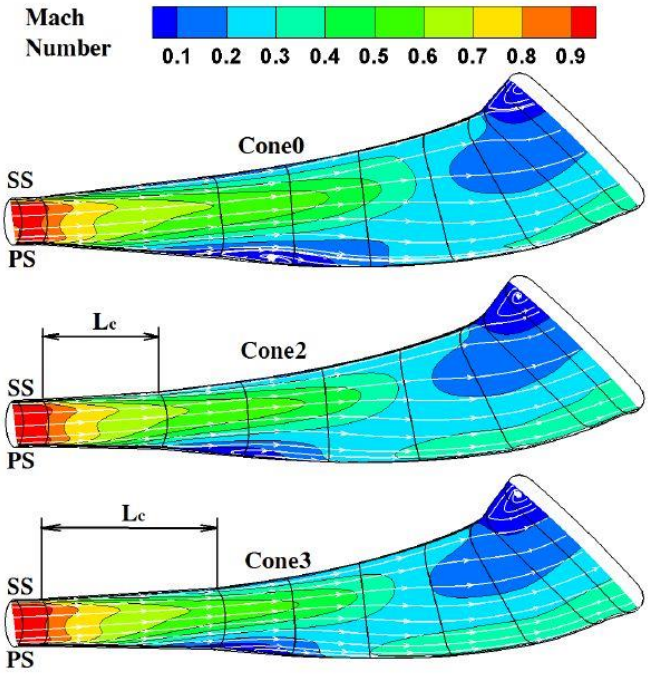

Figure A.2: Mach number contour and streamlines on diffuser mid-span of different cone length [12]

Staring from the 'Cone 2' configuration, the area distribution was changed, keeping the same ratio between the elliptical shape centerline axes of 0.75. It was found that the baseline design with linear area change (Figure A.2) has a better performance than the trumpet-shaped or bell-shaped area distribution, as can be seen by Mach number contours and streamlines (Figure A.3). Surge margin can be enhanced for the slight trumpet-shaped diffuser but at the cost of lower aerodynamic performance. However, bell-shaped is not recommended. This is similar to the results by Dolan *et al.* [50] that showed conical diffuser has a better performance at low inlet aerodynamic blockage and inlet Mach number below unity over bell-shaped and trumpet-shaped diffuser. Their results indicated that bell-shaped diffuser might have occasional advantages.

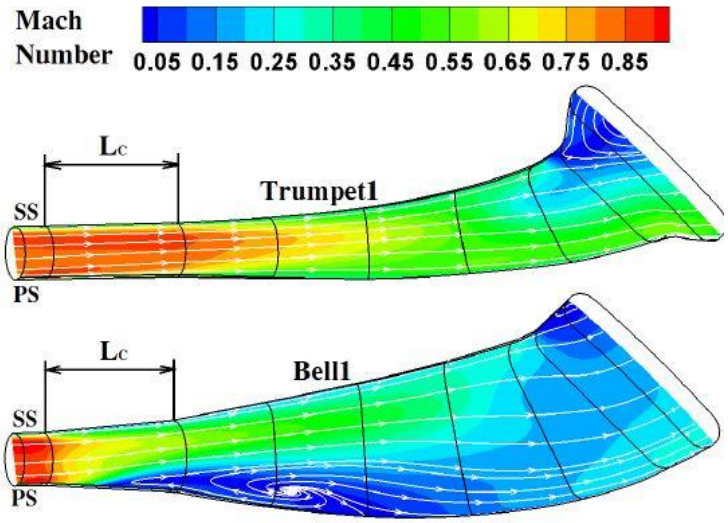

Figure A.3: Mach number contour and streamlines on diffuser mid-span of different area distribution [12]

The last parameter studied by Han *et al.* [12] was the shape of the centerline. As can be seen in Figure A.4, it is a quarter ellipse with a_0 being the axis in the radial direction and b_0 the axis in the axial direction.

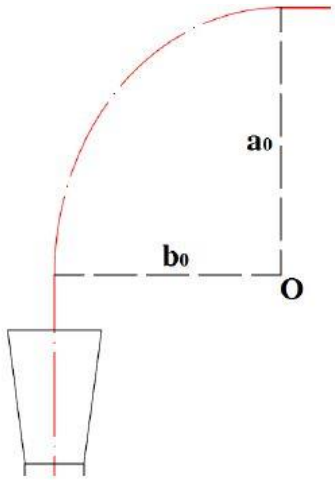

Figure A.4: Fishtail diffuser centerline [12]

The authors found that a larger turning radius makes the passage turn more smoothly, resulting in reduced losses and better performance. However, there is a maximum curvature radius beyond which the performance declines. Turning the flow from radial to axial direction when it has been diffused to lower velocities reduces turning losses and improves the performance. In other words, the ellipse long axis should be in the radial direction, i.e. a_0 should be higher than b_0. The optimum value of a_0/b_0 was found to be 9/5. The detailed work done in reference [12] served as a guideline for *fishtail* pipe diffuser design in the current research.

APPENDIX B MESH STUDY

B.1 High-Speed Mesh Study

Table B.1 lists the three different meshes used in the mesh study for the high-speed centrifugal compressor.

Table B.1: Mesh details for high-speed centrifugal compressor mesh study

High-Speed Baseline	**Mesh Type**	**Number of Mesh Elements**		
		Mesh1 (x)	**Mesh2 (2x)**	**Mesh3 (3x)**
Bellmouth	Structured	20746	39150	58240
Impeller	Structured	591798	1164964	1782996
Fishtail Diffuser	Unstructured	1062644	2298481	3303159
End Duct	Unstructured	161703	355214	485684
Total		1836891	3857809	5630079
y+		14.3	10.4	9

Figure B.1 plots the total-to-static pressure ratio versus the total number of mesh elements. Without a clear asymptotic trend and relatively small changes in pressure ratio between the meshes (implying that one may already be in the asymptotic range). Furthermore, all meshes have an average $y+$ value that are above the recommended minimum value of 2 [44]. The medium mesh (Mesh2) was selected.

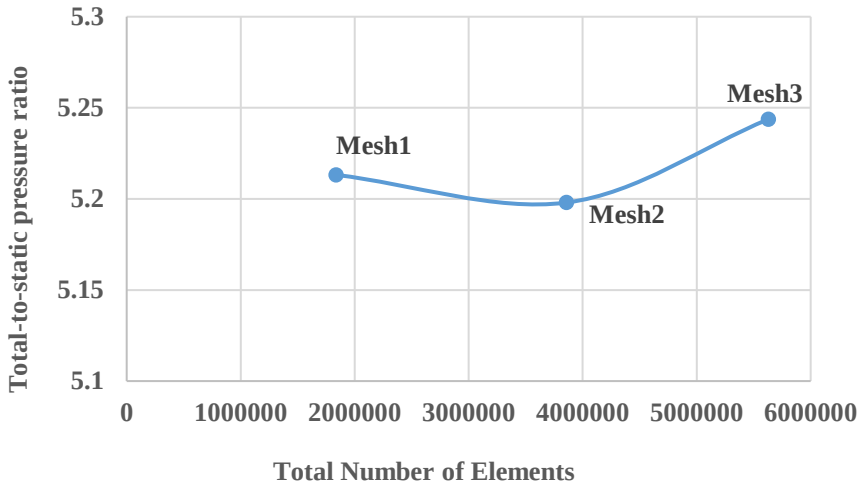

Figure B.1: Total-to-static pressure ratio versus total number of mesh elements for high-speed centrifugal compressor

B.2 Low-Speed Mesh Study

Five different meshes were used in the mesh study for the low-speed centrifugal compressor. The number of mesh elements for each independent domain of the baseline and the average *y*+ number for the entire baseline domains are summarized in Table B.2.

Table B.2: Mesh details for low-speed centrifugal compressor mesh study

Low-Speed Baseline	**Mesh Type**	**Number of Mesh Elements**				
		Mesh1 or baseline mesh (x)	**Mesh2 (1.5x)**	**Mesh3 (2x)**	**Mesh4 (3x)**	**Mesh5 (4x)**
Bellmouth	Structured	76,050	112,288	153,664	228,928	311,364
Impeller	Structured	225,917	310,420	426,318	648,432	864,576
Fishtail Diffuser	Unstructured	829,094	1,327,124	1,853,847	2,853,785	3,720,236
End Duct	Unstructured	98,488	165,200	211,586	344,277	461,295
Total		1,229,549	1,915,032	2,645,415	4,075,422	5,357,471
y+		12.9	11.9	8.4	8.6	7.7

Figure B.2 plots the total-to-static pressure ratio versus the total number of mesh elements for the different meshes. Again, without a clear asymptotic trend, the medium mesh (Mesh3) was chosen.

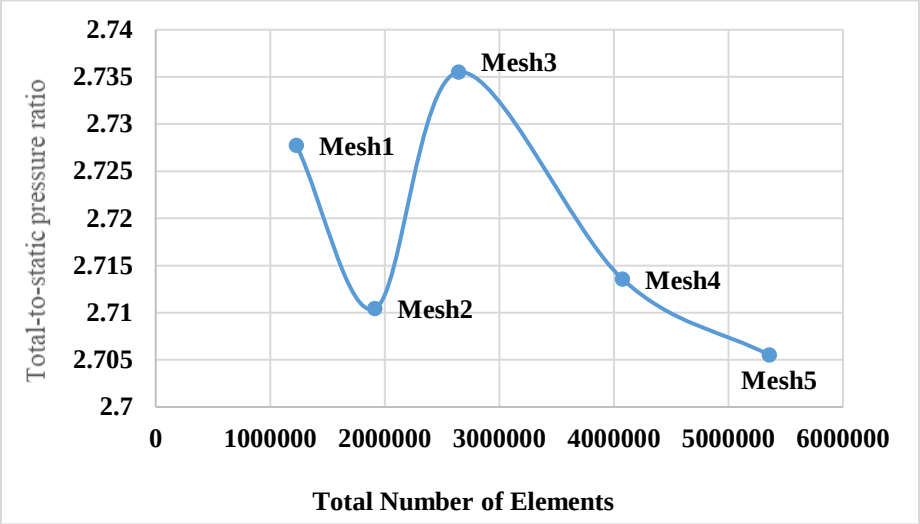

Figure B.2: Total-to-static pressure ratio versus total number of mesh elements for low-speed centrifugal compressor

APPENDIX C TIME-STEP SENSITIVITY STUDY

A sensitivity study has been carried out to determine the optimal time-step size in terms of number of iterations per impeller blade passing (pitch). The test case is the low-speed baseline centrifugal compressor at its design point. Six different number of iterations per blade passing is considered (2, 5, 10, 20, 40 and 80). Figures C.1 through C.3 plot the impeller efficiency, diffuser loss coefficient and stage efficiency, respectively, versus the number of iterations per blade passing. The results indicate that 10 iterations per blade passing is adequate.

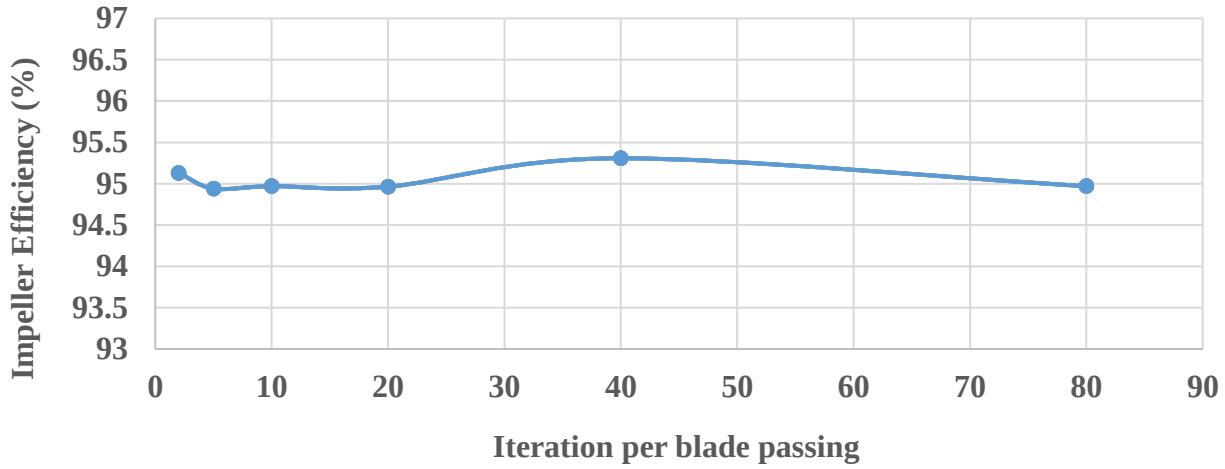

Figure C.1: Impeller efficiency versus number of iterations per impeller blade pitch at low-speed design point

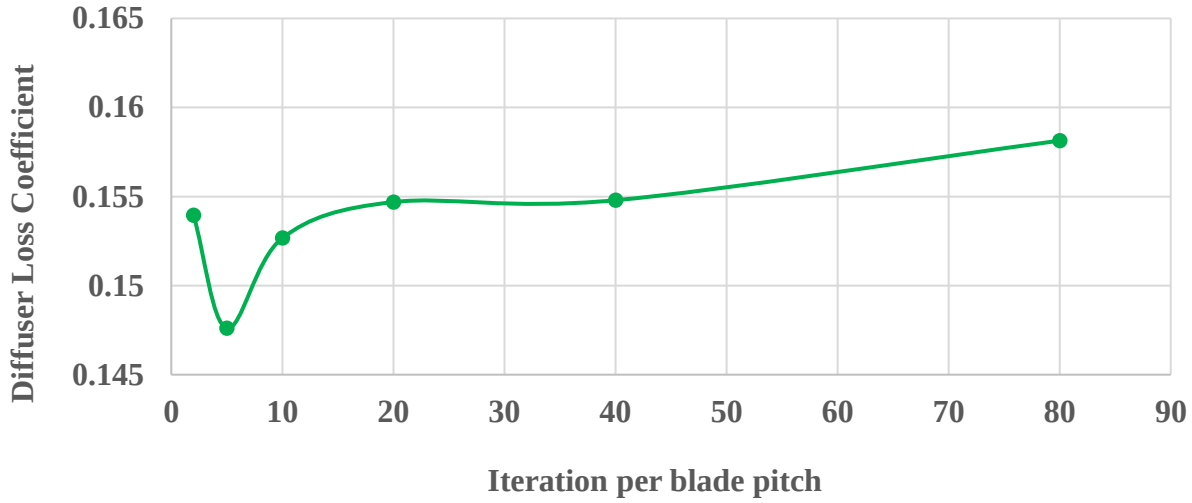

Figure C.2: Diffuser loss coefficient versus number of iterations per impeller blade pitch at low-speed design point

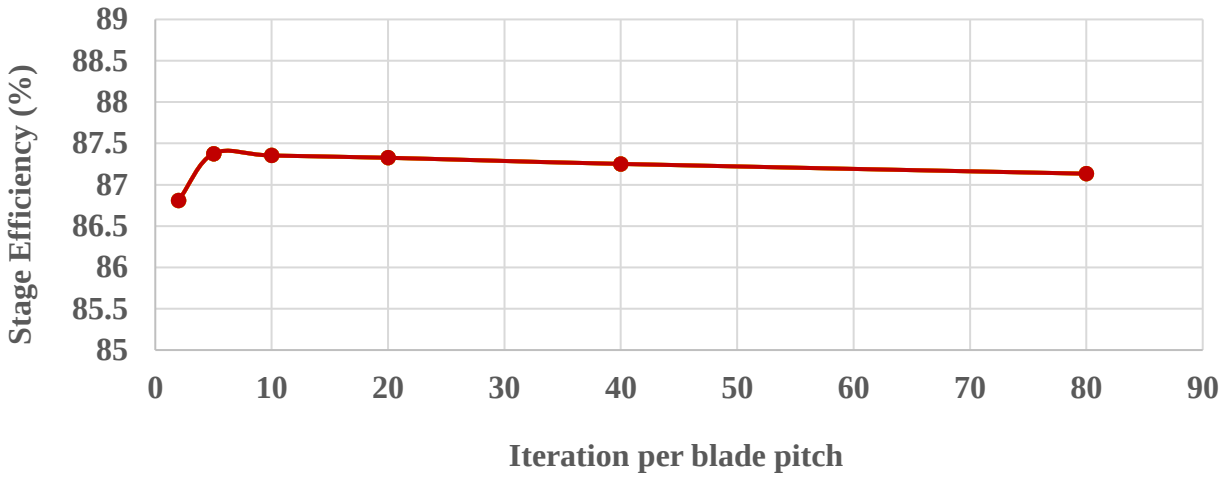

Figure C.3: Stage efficiency versus number of iterations per impeller blade pitch at low-speed design point

APPENDIX D FLOW CONTROL IMPACT AT RADIAL BEND VERSUS UPSTREAM OF LE

A preliminary study was carried out to see how the placement of passive flow control affects stall margin improvement and performance. The slots casing treatment in the high-speed centrifugal compressor was placed at the impeller leading edge (LE) region and compared with the same slots placed at the radial bend as shown in Figure D.1. Table D.1

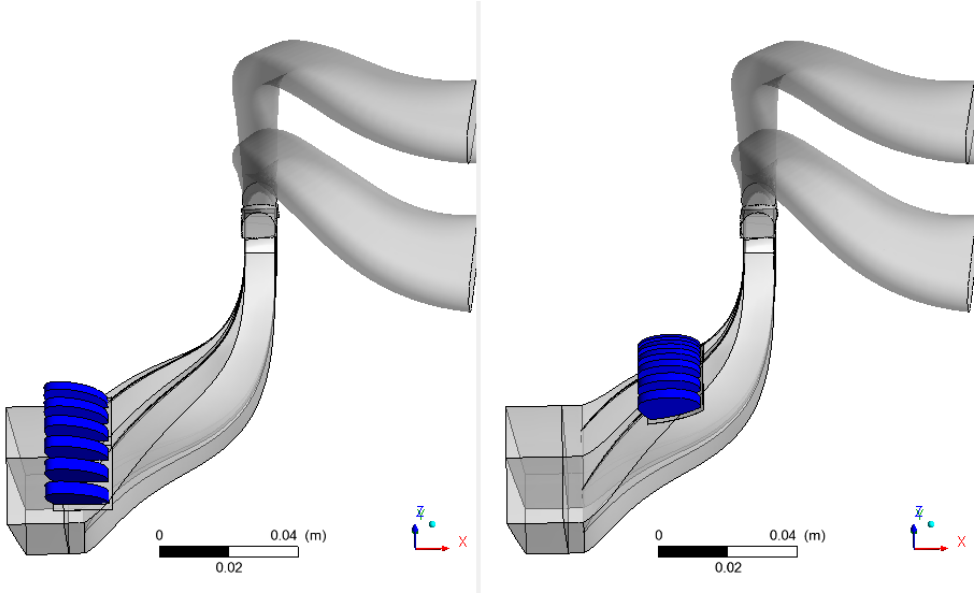

Figure D.1: Schematic of slots casing treatment applied over the leading edge (left) versus at the radial bend (right) at high-speed

Table D.1 list the integral parameters. The results indicate that the placement of the slots at the radial bend is significantly more effective in improving the stall margin, although it incurres a bit more penalty in performance (stage pressure ratio and efficiency).

Table D.1: Performance parameters of slots at impeller LE versus slots at radial bend for high-speed centrifugal compressor

	Stall Margin Improvement (%)	**Total-to-Total Pressure Ratio**	**Stage Efficiency (%)**
Baseline	-	5.22	84.01
Slots @ LE	2.60	5.20	83.70
Slots @ radial bend	3.57	5.17	82.73

APPENDIX E PSEUDO-FORCES IN IMPELLER ROTATING FRAME

The pseudo-forces acting on flow particles in the impeller rotating frame are defined with the following relations.

$$F - m\frac{d\Omega}{dt} \times r - 2m\Omega \times v - m\Omega \times (\Omega \times r) = ma \qquad \text{(E.1)}$$

Where:

F: $vector\ sum\ of\ the\ physical\ forces\ acting\ on\ flow\ particle\ in\ rotating\ frame$

r: $radial\ distance\ of\ the\ flow\ particle\ from\ roation\ axis$

Ω: $rotational\ speed$

v: $velocity\ of\ the\ flow\ particle\ in\ rotating\ frame\ of\ refernce$

$-m\frac{d\Omega}{dt} \times r$: $Euler\ (inertial)\ force$

$-2m\Omega \times v$: $Coriolis\ force$ (pseudo-force)

$-m\Omega \times (\Omega \times r)$: $Centrifugal\ force$ (pseudo-force)

In the current study in which the rotational speed is constant, the Euler force is zero and the two pseudo forces acting on the flow particles in the impeller passage are:

- The centrifugal force, which acts radially outward from the rotation axis and depends on the radius and the rotational speed, is the same for all flow particles at the same radius from the rotation axis.
- The Coriolis force, which acts normal to both the rotation axis and the particle relative velocity, and depends on both rotational speed and relative velocity, is different for flow particles with different relative velocity vectors.